Prototype Electron Beam Trackers Based On Quantum Coherent Optical Magnetometry

Nicolas DeStefano

Virginia Beach, Virginia

Master of Science, William and Mary, 2021
Bachelor of Science, Old Dominion University, 2019

A Dissertation presented to the Graduate Faculty of
The College of William and Mary in Virginia in Candidacy for the Degree of
Doctor of Philosophy

Department of Physics

The College of William and Mary in Virginia
August 2026

© Copyright by Nicolas DeStefano 2026

APPROVAL PAGE

This Dissertation is submitted in partial fulfillment of
the requirements for the degree of

Doctor of Philosophy

Nicolas DeStefano

Approved by the Committee, June 2026

Committee Chair
Irina Novikova, Professor of Physics, Physics
College of William & Mary

Eugeniy Mikhailov, Professor of Physics, Physics
College of William & Mary

Seth Aubin, Associate Professor of Physics, Physics
College of William & Mary

Todd Averett, Professor of Physics, Physics
College of William & Mary

Shukui Zhang, Staff Scientist, Accelerator Division
Thomas Jefferson National Accelerator Facility

ABSTRACT

Charged particle detection in nuclear and particle physics experiments have been driven by the search for new fundamental physics. To map the interactions and fundamental makeup of matter, particle accelerators are built to accelerate charged particle beams and capture particle dynamics within the atomic nucleus through beam collision experiments. While accurate control of charged particle beams are used to produce collision events, robust detectors are required in order to diagnose the intensity distribution and trajectory of the particle beams. While contemporary particle beam detectors can accurately map the current density of charged particle beams, there is a trade-off between sensitivity and invasiveness. In this dissertation we outline the development of atom-based magnetic field sensors to provide sensitive, non-invasive, localized, and self-calibrating measurements of electron beam magnetic fields to map the beam current density. This approach of magnetic field measurements has also been adapted for use in space, security, navigation, medicine, and physics research. As electrons pass through a dilute vapor of rubidium atoms, their magnetic field perturbs the atomic quantum states, causing polarization rotation of a laser resonant with the optical transition of the atoms. By measuring the polarization rotation angle across the laser beam, we recreate a 2D projection of the magnetic field and use it to determine the e-beam position, size and total current. We successfully tested this method for an e-beam with currents ranging from 30 to 110 μA to profile essential beam characteristics (i.e. beam position, shape, and total current). However, quantum fluctuations limit magnetic field sensitivity due to the shot noise of the interacting resonant optical fields. We reduce this quantum noise using intensity-correlated lasers generated through non-degenerate four-wave mixing to enhance magnetometer sensitivity by a factor of 3 compared to the classical optical shot noise limit. This improvement allows us to measure magnetic fields not possible using traditional optical magnetometers. This new approach increases magnetic sensitivity by significantly reducing optical noise, which should enable low-current charged particle beam profiling. This approach toward quantum-enhanced magnetometry is a competitive solution for non-invasive characterization of charged particle beams used in accelerators for particle and nuclear physics research.

TABLE OF CONTENTS

Acknowledgments iv

Dedications v

List of Figures vi

Chapter 1. Introduction 1

1.1 Electron Beam Tracking 1

1.2 Atomic Magnetometers 4

1.3 Photon Shot Noise and Atomic Spin Projection 6

1.4 Dissertation Outline 7

Chapter 2. Fundamental Theory 8

2.1 Wave Propagation In Atomic Mediums 8

2.2 Macroscopic Polarization of the Medium 11

2.3 Atomic Quantum Dipole Moment 12

2.4 Density Matrix Formalism 14

Chapter 3. Electron Beam Magnetic Field Detection 16

3.1 Classical Magneto-Optical Coupling 16

3.2 Nonlinear Magneto-Optical Rotation 18

3.3 Electron Beam Magnetic Profile & Current Density Reconstruction 23

3.4 Electron Beam Profiling via NMOR 28

3.4.1 Tabletop Electron Beamline 28

3.4.2 Electron Beam Characterization 33
3.4.3 Electron Beam Magnetic Field Profiling 37
3.5 Electron Beam Parameter Verification 45
3.5.1 Beam Current Measurement Sensitivity and Beam Width Discrepancy 46

Chapter 4. Quantum-Enhancement Via Four-Wave Mixing 50
4.1 Four-Wave Mixing Theory 52
4.1.1 Four-wave mixing in Rb vapor double-Λ systems 54
4.1.2 Noise Characteristics of FWM Fields 56
4.2 Four-Wave Mixing Squeezing Characterization 60
4.2.1 Shot Noise Calibration 63
4.2.2 Squeezing Optimization 65

Chapter 5. Far-Detuned Quantum-Enhanced Magnetometry 69
5.1 Enhancing Off-Resonant Magnetic Sensitivity 70
5.2 Squeezed Far-Detuned Magnetometry Characterization 72
5.2.1 Squeezed Magnetometer Optimizations 73
5.3 Quantum-Enhanced Magnetometry 77
5.4 Future Fundamental Research 79
5.4.1 Quantum-Enhanced Magnetic Gradiometer 79
5.4.2 Quantum-Enhanced Magnetic Field Imaging & Vector Magnetometry 80

Chapter 6. Conclusion 83

Appendix A. Quantum Fundamentals 85

Appendix B. Vacuum Procedures 87

B.1 QET Valve Routines 87
B.1.1 Part Descriptions 87
B.1.2 Expected Power Outage Procedure 88
B.1.3 Unexpected Power Outage Procedure 89
B.2 Minimizing Rb Oxidation When Opening Vacuum 89
B.2.1 Vacuum Work Gas Backflow Procedure 90
B.3 Electron Gun Procedures 91
B.3.1 Preliminary Checks 91
B.3.2 Slow Startup 92
B.3.3 Fast startup 93
B.3.4 Standby (less than 1 hr) 93
B.3.5 Standby (less than 3 hr) 93
B.3.6 Shutdown 94

Appendix C. Squeezing Balanced Photo-Detector Schematic 95

References 99

ACKNOWLEDGMENTS

The work presented in this dissertation would not have existed without the support of all those I've interfaced with over the years. First, I am exceptionally grateful for my advisor, Irina Novikova, who's incredible patience over the years taught me the value of constant curiosity, mentoring, and teaching. I thank my advising team, including Eugeniy Mikhailov, who inspired me to learn hardware at a fundamental level; Seth Aubin, whose inquisitive questions turned into unique discoveries; and Todd Averett, whose optimism and outlook helped keep me motivated throughout the project. I also thank our external collaborators Shukui Zhang and Alexandre Camsonne for stimulating conversations and perspectives from the nuclear community. For my close colleagues, Ziqi Niu and Rob Behary, whose conversations lead to solutions and fun music themes in the lab. Ziqi kept me motivated and entertained, whose ideas laid the foundation for later work in this dissertation. Whereas Rob helped make me a part of the Rydberg sensing group and made the quantum optics lab a close-knit group throughout the years. I was inspired to watch talented undergraduates including Sophia, Jiahui, Kevin, Will, Owen, Kalea, and Zach grow through the lab; I'm thankful to grad students and postdocs in the lab: Savannah, Charris, Sumrah, Nehal, Saeed, Mario, and Michael for their mentorship,curiosity, and comradery. I appreciate Justin, Kate, Axl, Will, Yiqi, Jack, and Quinn, who gathered in person every other week for D&D for much needed laughs, as well as Felipe, Will, Anja, Yangli, Chris, Hanzhou, and Jaejeong who shared living spaces with me through the years. I am grateful to the W&M grad student community through GSA and Journal Club inspired interdisciplinary conversations and involvement each week particularly with the help from Ben Spaude, Aidan Lucas, Michael Sizemore, and many others. I recognize, in memoriam, my undergraduate research advisor, Mark Havey, and my friend and colleague, Corey Sargent, within the Old Dominion Physics department. Mark gave me the first opportunity to do physics research, while Corey inspired me to become involved and was poised to become the first astrophysics PhD student in the department. I treasure the constant support from those from my hometown. To James, Ligia, Leicelle, Taylor, and everyone else in squash, I would not have completed this dissertation without and thank Kasey for teaching me to live and learn independently. I am deeply grateful to Yalda, Dr. Massengill and the counselors in the New Leaf center in William & Mary's School of Education for their support and contributions to my personal health and well-being through this journey. Finally, I thank Molly Robinson, for her constant support leading up to the finish line. You inspire me each day to continue learning and trying new things, and I cherish the adventures we had, and will have, in the coming years. This list shows how many people contribute to a PhD project throughout the years, of which I am grateful to all I have interfaced with during this time. For that, I am incredibly lucky and sincerely thankful to be a part of each of your lives.

This work is dedicated to my parents, Wanika and Robbie, and my siblings, Katarina and Marshall

LIST OF FIGURES

1.1 Electric (E) and magnetic (B) fields generated by an electron beam due to moving charged particles that make up the electron beam. The electromagnetic fields alter atomic properties in the detection medium, which is read out using a resonant probe laser and detector. 3

2.1 Λ transition scheme for the $F = 1 \rightarrow F' = 0$ transition, showing the 3 possible transitions using left circularly polarized σ_-, z-polarized π, and right circularly polarized σ_+ resonant light. 13

3.1 (a) Mechanism of the classical Faraday effect. (b) linear response of the polarization rotation angle β due to magnetic field magnitude B for $L = 1$ mm and $\nu = 1$. 17

3.2 (a) simplified energy level scheme for the closed NMOR system, without decoherences. States $|b_+\rangle$,$|b_-\rangle$, and $|a\rangle$ correspond to $|m_F = +1\rangle$, $|m_F = -1\rangle$ and $|m_{F'} = 0\rangle$ states, respectively. (b) NMOR scheme for the open system, including decoherences and pumping terms due to spontaneous emission Γ, transit decoherence γ_0, decays to external states $\tilde{\Gamma}$ and repumping $\gamma_0/2$ decoherences. 19

3.3 Sensitivity comparison between linear Faraday effect (orange dashed) with $L = 1$ mm, $\nu = 1$ and nonlinear magneto-optical rotation (solid blue) where $\frac{\hbar c N \gamma}{\lambda I} = 20$, $L = 1$ mm and the width of the resonance $\Gamma_{EIT} = 1$ from equations 3.12 and 3.11 22

3.4 The basic concept of the charged particle beam detection method. The linear polarization of a probe laser beam (red) φ is affected by the magnetic field (dashed light blue circles) of an electron beam (dark blue) mediated by the spin coherence of Rb atoms. 24

3.5 Effect of finite cell length L compared to electron beam width w on the polarization rotation profile $\varphi(y)$ generated from the electron beam magnetic field of equation 3.14 shown in figure 3.4. The rotation profile $\varphi(y)$ is evaluated from equation 3.17 for infinite cell length $L \gg w$ (blue) and finite cell length $L \approx w$ (orange), causing the tails of the profile to fall off far from the center of profile. These profiles were calculated for $\beta\mu_0\mathcal{I}_0 = 1$ rad, $y_0 = 0$ mm, $L = 10$ mm, and $w = 1$ mm, and is oriented to match the expected output polarization in the zy-plane from figure 3.4 26

3.6 Representative diagram of the electron beam vacuum system. Inline, angle, and gate valves are all marked with an inscribed "X". Various Pirani (P), cold-cathode ionization (I-CC), and hot-cathode ionization (I-HC) pressure gauges monitor vacuum pressure around the system. Helium (He) or other gases can be pumped into the Rb cell. The electrons terminate in the Faraday cup (FC) to measure total current at the end of the system. 30

3.7 Effect of Faraday cup biasing on the measured electron beam current. (a) Scheme used to bias the Faraday cup, where the cup and surrounding vacuum system is grounded. (b) Change of Faraday cup current versus biasing voltage. 32

3.8 Coupling efficiency of the electron emission current into the Faraday cup (without any bias voltage) located 1 meter downstream of the electron gun. The coupling efficiency is evaluated using a linear fit (orange) to the data (blue). 34

3.9 (a) e-beam current transient due to the refocusing of the electron beam when turning the beam on. (b) Faraday cup signal when sweeping the electron beam through the Faraday cup aperture. 35

3.10 Electron beam impact fluorescence in Rb vapor at three different vertical positions of the electron beam. Each image uses 10 averages with a camera exposure of 30 s per average. The left-most plot shows the vertical profiles (transparent) and Gaussian fits (opaque) used to verify electron beam widths and positions. The images on the right are the fluorescence images captured by the fluorescence camera. 35

3.11 Alternative secondary diagnostics that can be used to measure the electron beam profile. (a) Optical transition radiation (OTR) of the electron beam impacting the solid copper gasket between the upstream chamber and Rb cell in figure 3.6. The dashed red box enclosing the blue light shows where the electron beam impacts the gasket. (b) Harp scanner made to profile the electron beam current density. The electrons deposited on the wire can be read out as a current while the wire scans across the electron beam, by mapping the current on the wires to the position of the scanner, the cross section of the electron beam can be read out. (c) Electron impact-induced helium fluorescence inside the Rb cell captured using a high-exposure cellphone camera. Propagating the electron beam through high helium pressure (≤ 1 Torr) generates fluorescence, which can be used to measure the electron beam profile with greater signal-to-noise compared to Rb fluorescence in figure 3.10. 37

3.12 (a) Schematic of the experimental setup (see text for abbreviations), where a flipper mirror determines BPD- or CCD camera-based detection. (b) Laser intensity profile at the output of the PBS, recorded by the CCD with ~ 200 μs exposure time. (c) The e-beam-induced polarization rotation angle, $\varphi(y, z)$, calculated using equation 3.20. (d) The electron current density distribution reconstructed from the erf-function fit of the normalized polarization rotation $\Phi(y, z)$. For all the image analysis an intensity mask is applied to eliminate data points with laser intensity below 5% of the peak value to prevent infinities arising from $I_1 + I_2 = 0$ in equation 3.20 38

3.13 (a) Electron beam position change relative to the probe laser demonstrating the reversal of magnetic field direction across the laser cross-section. (b) Resulting NMOR based on two electron beam positions (orange and green, left axis) when the electron beam is turned on (blue, right axis). Due to the opposite directions of magnetic field between electron beam positions, opposite NMOR direction occurs, emphasized by the arrows for each plot. 40

3.14 Camera triggering relative to the pulsing of the electron beam. The trigger signal is set so that the camera exposure (orange) activates after the electron beam transients measured in the Faraday cup (blue) stabilize to consistently capture a constant beam profile. The width of the camera trigger pulse is the exposure time (50 ms, in this demonstration). 42

3.15 Dropped frame demonstration and correction procedure to ensure proper pairwise subtraction. (I) Frames are acquired every T seconds alternating between electrons ON I and OFF O, except for frame 4, which never arrives despite the camera and electron beam successfully triggering, resulting in an additional frame 9 at the end of the data acquisition. (II) Removing the frame with period $2T$ and the final frame (frames 5 and 9) resets the ordering of electron pulsing to follow correct ordering shown in (III). 43

3.16 (a) uniform magnetic field coil calibration to voltage driving the coils. Calibrations were taken on each side of the cell (blue, orange) with the average of the calibration corresponding to the field inside of the cell (green). (b) $\beta(y, z)$ calibration used to normalize out the light-matter variation from the NMOR images in figure 3.12(c). 44

3.17 Measured normalized rotation images $\Phi(y, z)$ for two different electron beam positions of electron beam emission current $\mathcal{I}_E = 200\mu$A and energy $E = 20$ keV. The location of the e-beam center in each case is clearly detectable by the reversal of the polarization rotation direction (red versus blue). The left panel shows the vertical profiles of the images with the corresponding fits from equation 3.17, and the horizontal dashed lines indicate the positions of the electron beam center, also extracted from the fits. 44

3.18 (a) Comparison between the electron beam center position extracted from the polarization rotation measurement $y_{0,\text{NMOR}}$ and from the electron-induced rubidium fluorescence images $y_{0,\text{fluorescence}}$ with a regression of $y_{0,\text{NMOR}} = (1.16 \pm 0.21)\ y_{0,\text{fluorescence}}$ (dotted blue line). (b) Comparison between the total electron beam current determined using the polarization rotation fits $\mathcal{I}_{\text{NMOR}}$ and measured directly using the Faraday cup $\mathcal{I}_{\text{FC}}$ with a regression of $\mathcal{I}_{\text{NMOR}} = (1.36 \pm 0.13)\ \mathcal{I}_{\text{FC}}$ (dotted blue line). The black dashed lines have a slope of 1 and 2, representing $\mathcal{I}_{\text{FC}}$ and the emission current $\mathcal{I}_{\text{E}} \approx 2\mathcal{I}_{\text{FC}}$. The shaded region indicates the range of valid beam currents measurable by NMOR. Uncertainties in NMOR-derived parameters stem from the variance of electron beam center position and total current under identical experimental conditions. The fluorescence uncertainty is based on the variance in center position for varied beam currents, while the Faraday cup signal uncertainty is due to the variance of the measured Faraday cup signal (read on an oscilloscope). 46

3.19 Fourier transformed signals from the BPD in the absence of polarization rotation. Plotted are the cases of typical experimental conditions (experiment noise, orange) compared to the dark noise of the BPD (BPD noise, blue). The red line in the bottom shows the shot-noise limited sensitivity. The right axis defines the minimum detectable current, based on the minimum detectable rotation angle of the left axis. 47

4.1 Input and output scheme for the four-wave mixing process. Two powerful pump fields E_{c_1} and E_{c_2} and a weak probe field E_a interact within a general third-order nonlinear medium to generate four output optical fields, including a new conjugate field E_b. 52

4.2 Light vector diagram showing momentum conservation in the case of nonzero angles $\theta_1 = \theta_{c_1} - \theta_a$ and $\theta_2 = \theta_{c_2} - \theta_b$, allowing separation of pump, probe, and conjugate fields dependent on the relative frequencies of the pump and probe fields. 53

4.3 (a) Mechanism of four-wave mixing. A powerful pump field c and weak probe field a intersect within the Rb cell, and generate a new conjugate field b through the third order nonlinear susceptibility of the medium and phase matching between the pump and probe fields. The input mode for the conjugate field is the vacuum state, while the input states for probe and pump fields are coherent states. (b) Double-Λ interaction scheme for FWM for the D_1 transition of Rb ($\lambda = 795$ nm). 54

4.4 Experimental scheme to measure squeezing in the four-wave mixing cell. The pump is focused down using an $f = 1000$ mm lens to increase the pump intensity for FWM, which is filtered out using the second polarizing beam splitter (PBS) and irises. To measure relative intensity squeezing, the differential probe and conjugate transmission is measured with a custom-made balanced photo-detector (BPD) 60

4.5 FWM frequency detunings relative to the rubidium spectra of the D_1 line operating around $\lambda = 795$ nm. The pump is initially tuned to the indicated detuning in order for the FWM gain peak to occur $\geq$ 1 GHz from the $F = 3 \rightarrow F'$ atomic transition, while the probe is ble-detuned $\Delta_{2p} = 3035$ MHz from the pump. Both lasers are tuned in this way to minimize optical losses due to atomic absorption. 61

4.6 (a) Setup to lock the relative frequency difference between the input pump and probe lasers to $\Delta_{2p} = 3035$ MHz. (b) Example of the beat note generated between the pump and probe lasers within the phase detector. The actual measured peak occurs at half of the set frequency due to the output of the Vescent phase lock, so the frequency axis is doubled for demonstration. 62

4.7 effect of varied (a) resolution bandwidth (with VBW = 10 Hz) and (b) video bandwidth (with RBW = 300 Hz) on a 300kHz sinusoidal signal on the spectrum analyzer. The resulting noise trace should behave like a delta function at 300 kHz, while peaks outside of 300 kHz are parasitic harmonics from lower frequency oscillations picked up by the spectrum analyzer. 63

4.8 (a) Balanced differential detection scheme to measure differential noise as a function of probe laser power. (b) the resulting logarithmic and linear noise as a function of laser power. Fitting the linear noise provides a calibration mapping the measured photovoltage to the expected shot noise, allowing immediate evaluation of the squeezing for each measurement. 64

4.9 Dependence of squeezing on probe power ($P_{pump,in} = 340$ mW, $\Delta_{2p} = 3.0382$ GHz, $T_{cell} = 105$ °C), two-photon detuning ($P_{probe,in} = 55$ μW, $P_{pump,in} = 340$ mW, $T_{cell} = 105$ °C), and cell temperature ($P_{probe,in} = 55$ μW, $P_{pump,in} = 343$ mW, $\Delta_{2p} = 3.0357$ GHz). By optimizing these 3 parameters, we are optimizing the coupling ξ (equation 4.9 between atoms and incident optical fields). Probe power uncertainty is due to temperature- and polarization-induced fiber instabilities during data acquisition. 66

4.10 Demonstration of two-mode intensity squeezing from the FWM process at 300kHz frequency. 68

5.1 Comparison between (a) resonant NMOR and (b) far-detuned magnetometry. The addition of the pump field in the Λ system breaks the symmetry of the traditional Λ scheme by establishing an additional coherence. 70

5.2 Left: Demonstration of far-detuned magnetometry driven by a sinusoidal magnetic field (dashed red) for $P_{pump} = 5$ mW, $P_{probe} = 150$ μW, $T_{cell} = 21$ °C (room temperature), $\Delta_{pump} = 0$ MHz and $\Delta_{probe} = -1816$ MHz from the ^{87}Rb D_1 $F = 2 \rightarrow F' = 2$ transition. The polarization angle only rotates in the presence of the pump field (blue), and in the absence of the pump (orange), the NMOR oscillations are significantly decrease due to the far detuning of the probe field. This differs from the frequency regime for the FWM, but the resulting far-detuned magnetometer principle is identical in either regime. Right: Probe transmission in the presence of the pump (blue) and absence of the pump (orange). The 3% increase in transmission indicates the lack of optical pumping or FWM processes. 71

5.3 Combined experimental scheme for the squeezed light magnetometer. The FWM cell generates -4 – -4.4 dB of squeezing, which is sent to the magnetometer cell ($L = 1$") for magnetic field sensitivity characterization. The polarimeter detector is configured to measure NMOR using the quantum-enhanced noise suppression from FWM. 72

5.4 Optimizations to maximize the SNR of the magnetometer by varying pump power (left; $T_{cell} = 110$ °C, $P_{probe} = 500$ μW) and cell temperature (right; $P_{pump} = 380$ mW, $P_{probe} = 450$ μW). The SNR saturates around $P_{pump} = 350$ mW, while the temperature continues in a linear trend. To protect the Rb from reacting with the glass cell, only temperatures $T_{cell} \leq 110$ °C are used. 74

5.5 Dependence of SNR on pump polarization, showing a sharp response around 20° polarization angle relative to the probe polarization. (b) Probe transmission variance as a function of pump polarization, showing 14% fluctuation over the range of polarization angles. Pump polarization angles are physical polarization angles relative to the probe polarization. 75

5.6 Experimental (blue) and calculated (orange) SNR dependence on (a) probe and (b) conjugate balancing angle, where 45° corresponds to the balanced polarimeter. The calculated traces are given by equation 5.2 and are plotted to show the functional trend of the balancing angle dependence. 76

5.7 Demonstration of optical loss compensation on the squeezing when transmission loss is applied to the probe using a VIS antireflection coated window. Ideal squeezing performance is given in the absence of any optical losses (blue), but the squeezing degrades when loss is induced in the probe field (orange). By inducing equal amounts of loss in the conjugate channel (green), identical squeezing performance is recovered, resulting in the noises without probe loss (blue) and compensated conjugate (green) being equivalent. 77

5.8 Quantum-enhanced magnetometer signal using the squeezed fields generated through FWM and inducing magnetic sensitivity using far-detuned magnetometry. The squeezed magnetometer signal (blue) lies below shot noise (thick red line), which vanishes in the absence of the pump field (green) and magnetic field (orange) within the magnetometer cell. Blocking the conjugate (thin red) removes the noise cancellation, and the magnetic field signal peak at 300 kHz vanishes due to the optical noise drowning out the magnetic field signal. Inset focuses on the range below shot noise for convenience. 78

5.9 Experimental configuration using the conjugate to measure magnetic field gradients within the magnetometer cell. Inputting the conjugate in the opposite polarimeter input port allows differential measurement of the magnetic field between the probe and conjugate regions 80

5.10 Potential experimental implementation to extract spatial information about magnetic field magnitude or direction using a spatial light modulator (SLM), digital micro-mirror device (DMD), or vortex waveplate (VWP). 81

B.1 3 valves on the Faraday QET system. (1a) primary safety gate valve: dependent on lab power and the state of the control switch where the state of the valve is indicated through the white marker on the left side of the unit. (1b) control switch for the primary safety gate valve (annotated by (1a)): green opens the gate valve, red closes the valve. This switch will maintain the valve closed position until the green button is manually pushed. (2) gradual angle valve: an angle valve which slowly opens and closes by manually rotating the valve handle. (3) manual gate valve: valve similar in structure to the primary safety valve, but requires manual turning to open and close. 88

C.1 Electronic schematic for the op-amp circuits and power supply. 97

C.2 Electronic schematic for the connectors for various outputs, POS_OUT (CH1), NEG_OUT (CH2), DIFF_OUT (DIFF), and SUM_OUT (SUM). 98

Chapter 1

Introduction

1.1 Electron Beam Tracking

With the advent of charged particle accelerators came the need for accurate beam characterization. Driven by improvements to quality and control of charged particle beams, the sensitivity and precision of *in-situ* diagnostics must meet the needs of new particle accelerators where increasingly strict demands are placed on beam energy, current, and emittance, among other beam properties. The need for increasingly precise beam profiling for a wide range of parameters inspires relentless efforts to continue towards the development of more robust, non-invasive spatial beam parameter measurements. Traditional harp (or wire) scanners provide accurate particle beam profile measurement by monitoring the current deposited on the wires by the charged particle beam as the scanner is swept across the cross-section of the particle beam [1]. This straightforward particle beam detector operates in low current regimes, whereas high-current electron beams sever the wires used for profile measurement. Extracting the beam profile using this method is invasive by design, since it interrupts charged particle beam transmission during profile measurement.

Profiling methods relying on optical signals can minimize the direct interaction with the particle beam. Synchrotron radiation has been used for monitoring beam position

and size [2–4], and laserwires [5, 6] rely on Compton scattering from a high-power laser to extract the charged particle beam parameters. However, these types of optics-derived signals are limited by technical requirements on the particle and laser beams. For example, synchrotron radiation is only available in particle trajectory-bending components such as magnets, while the laserwire method requires a high-intensity laser to slowly scan the beam profile, and often requires additional radiation, or electronic, detectors. Beam profile monitors based on gas ionization and excitation by particle beams have been demonstrated and used at different accelerators [7–9]. More recently, a 2D beam monitor measuring fluorescence from the interaction between a 5 keV particle beam and a supersonic gas curtain was reported [10], but the sensitivity is quite limited and it is not suitable for spatial longitudinal profile measurement.

However, another category of detectors avoids this collisional dependence by instead measuring the electromagnetic field generated by the particle beam. The charged particle beam is a collimated beam typically made up of accelerated electrons or ions to be used in nuclear detection experiments. These free charged particles that make up the beam produce electric fields from Gauss's law, and magnetic fields from Ampere's law shown in figure 1.1.

While this detection method is independent of direct interaction with the particle beam (i.e. non-invasive), devices based on this principle rarely measure more than one particle beam parameter simultaneously. The RF-based beam monitor is widely used in the accelerator community measures beam center position at high resolution, but is incapable of profile measurement [11]. Similarly, the beam current can be measured through RF-based beam current monitors which require calibration using a magnetic pickup coils to measure the charged particle beam current [12].

Thus there is great demand for a detector capable of charged particle beam spatial profiling without the requirement for direct beam interaction. Atom-based electromagnetic field sensors have been developed to detect electromagnetic fields too small to be measured by traditional magnetometers or electrometers. As an atomic vapor, these sensors

minimally interact with the sources of the fields being measured, removing the requirement for direct interaction with the electromagnetic field source. These types of sensors are immune to energy transfer from energetic particle beams due to the non-interactive nature and can be configured to acquire spatial beam characteristics via optical interrogation shown in figure 1.1. Given this, vapor-based sensors are a suitable platform for non-invasive particle beam profiling, enabling *in-situ* measurement for a wide range of beam currents and energies.

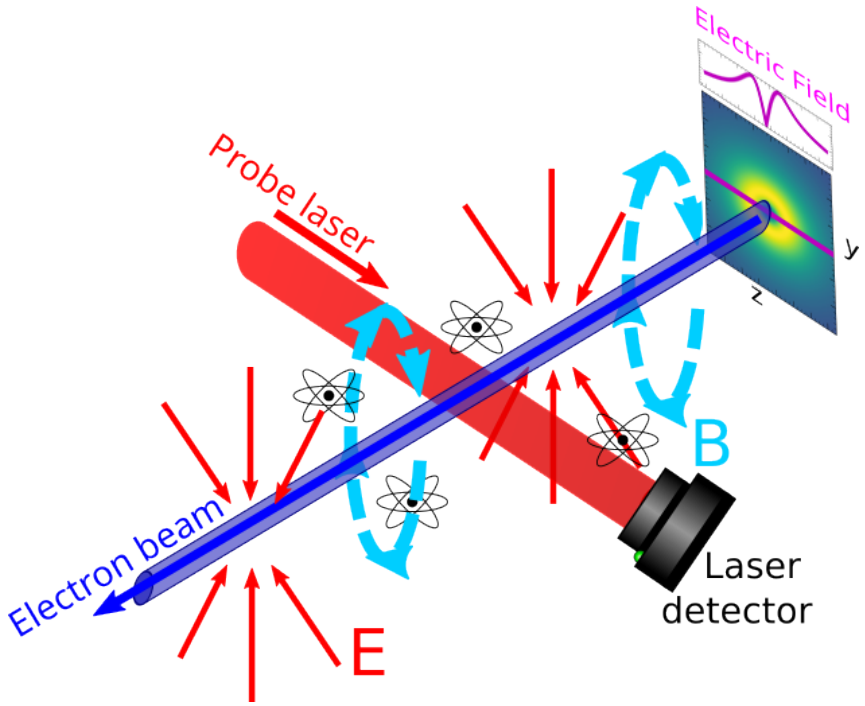


Figure 1.1: Electric (E) and magnetic (B) fields generated by an electron beam due to moving charged particles that make up the electron beam. The electromagnetic fields alter atomic properties in the detection medium, which is read out using a resonant probe laser and detector.

Highly-excited atomic Rydberg states are sensitive to small steady (DC) and time-varying (AC) electric fields by probing the associated interaction with resonant laser light [13–15]. Rydberg atoms in vapors have already been adapted to perform non-invasive measurements of spatially-varying electric fields due to an electron beam [16] and low-temperature plasmas [17]. However, Rydberg atom electric field sensitivity is indiscriminate of the electric field source. Parasitic free charges can globally skew electric field

measurements due to, e.g., lingering charges that build up on glass surfaces, requiring localized electric field sensing. Magnetic fields only form through the movement of charges in the detection medium, where any accumulated surface charge has negligible contributions to the detected magnetic field. In this case, magnetic field sensing is more robust in the presence of parasitic charges as a detector for charged particle beam magnetic fields. These examples demonstrate that atomic vapor-based sensors are invaluable for characterizing electric fields in nuclear or plasma experiments. In this work, we develop atomic vapor magnetometers to profile charged particle beams by minimizing direct particle beam interactions in contrast to traditional charged particle trackers.

1.2 Atomic Magnetometers

Most atomic magnetometers operate on the coupling of external magnetic fields to electron spin as well as strong and coherent interaction with resonant optical fields [18, 19]. Electromagnetic field detection based on this principle enables non-invasive, self-calibrating, and localized measurements that have a broad impact within the fields of intelligence, security, navigation, medicine, and physics. These magnetometers have been deployed to measure minute changes in local magnetic fields due to the presence of magnetized materials within submarines [20] and unexploded ordnances [21]. Magnetometers have also been adapted for geomagnetic-based navigation by comparing measured magnetic fields to Earth's magnetic field, resulting in a stable and reliable alternative to GPS in GPS-denied environments [22]. In the medical field, such magnetometers provide alternative methods of magnetoencephalography and magnetocardiography using arrays of atomic Rb vapor cells to measure small changes in brain and fetal magnetic activity [23, 24].

Nonlinear Magneto-Optical Rotation (NMOR) [19, 25, 26] of polarization has been thoroughly modelled [27] and experimentally demonstrated with sensitivities down to a few $\mathrm{pT/Hz^{1/2}}$ [28, 29]. This mechanism is due to the circular birefringence induced in the atomic medium by the optical field. This birefringence is altered in the presence of

a magnetic field, enabling precise measurements of said field through the optical polarization angle. Atoms as localized electromagnetic probes facilitate the imaging of the magnetic field generated by the charged particle beam, from which the particle beam current density can be extracted to acquire the beam profile. Some atomic magnetometers have been configured to image magnetic fields using various imaging schemes to capture field gradient and direction [30–33]. Vector magnetic field information can be extracted using NMOR spectral amplitudes and frequency shifts to sensitively determine field direction [34–38]. Cold atoms have also been explored as a platform for magnetic field sensing, where long atomic state lifetimes boost sensitivity otherwise limited by Doppler and collisional broadening [39, 40]. Complex schemes push NMOR sensitivity beyond classical limits by suppressing atomic spin fluctuations through so-called spin-exchange relaxation free (SERF) magnetometers [41–44]. Fluctuations in the interacting optical fields have also been suppressed using polarization self-rotation to reduce vacuum fluctuations of a probe field in an NMOR scheme by -1 – -2 dB below coherent vacuum noise [45–48]. Optical intensity fluctuations have also been suppressed using bright two-mode squeezed light in four-wave mixing, achieving an impressive -4 – -6 dB improvement in magnetometer sensitivity [49, 50].

The physical mechanism behind NMOR is rooted in the precession of the valence electron's magnetic moment about an externally applied magnetic field. As a result, the affected atom rotates the incident light's polarization. Therefore the measurements of magnetic field depend on (a) the precession of electron magnetic moment, proportional to the electron spin angular momentum and (b) the atomic interaction with optical fields. Both of these processes have lower bounds on how accurately they can be measured due to fundamental uncertainties that limit the sensitivity to magnetic fields.

1.3 Photon Shot Noise and Atomic Spin Projection

The lower bounds on optical field and electron spin measurements are set by the Heisenberg uncertainty principle. Due to the nature of the light-matter interaction, magnetic sensitivity is limited by two uncertainties: the optical shot noise and atomic spin projection.

Any optical magnetometer has noise contributions from the optical fields used to facilitate the atomic interaction and measure magnetic fields. Optical shot noise arises from fluctuations in the intensity and phase of the coherent optical field, which sets a lower bound on the minimum measurable intensity for any optical scheme. This shot-noise limit manifests in an NMOR measurement as the minimum detectable magnetic field when using coherent light [51].

Perhaps more fundamental is the limit on accurately measuring electron magnetic moment. The magnetic moment is proportional to electron spin angular momentum measured as a projection onto the desired quantization axis (e.g. the probe laser direction). Angular momentum F is subject to minimum uncertainty ΔF_i due to commutation rules between perpendicular components of angular momentum such that $\Delta F_x \Delta F_y \geq \langle F_z \rangle / 2$ [52], fundamentally limiting any atom-based measurements monitoring atomic angular momentum. However, spin projection noise can be reduced beyond this limit through spin squeezing [53] to achieve quantum-enhanced magnetometer sensitivities.

We address the dominant shot noise in atomic magnetometers by generating two entangled optical fields using four-wave mixing (FWM). By sending in powerful pump and weak probe laser fields and adhering to phase matching conditions a third, conjugate, field is generated [54–56]. This newly generated field contains intensity fluctuations identical to that of the probe laser, so a differential laser intensity noise measurement between the probe and conjugate falls below the shot-noise limit. Previous demonstrations of quantum noise suppression using FWM yield between -3 to -8 dB with respect to the shot noise limit of classical light [57, 58]. Four-wave mixing can benefit NMOR by suppressing the optical

intensity noise limiting the minimum resolvable magnetic field. Boosting the magnetic field sensitivity lowers the minimum detectable electron beam current, further widening the range of charged particle beams that can be profiled using this electromagnetic field sensor.

1.4 Dissertation Outline

In this dissertation, we present a qualitatively different approach to beam diagnostics that takes advantage of recent advances in quantum atom-based optical sensors to map the magnetic field produced by the moving charged particles to reconstruct the beam parameters. This demonstration is a stepping stone toward more sensitive and comprehensive detection of charged particle beams using advanced spectroscopy techniques. By combining these mechanisms of four-wave mixing and atomic magnetometry, we can profile electron beam currents not possible with traditional charged particle detectors.

This dissertation demonstrates a prototype magnetic-based electron beam tracker to profile the charge distribution of a particle beam and offers a path to achieving quantum-enhanced tracker performance. Chapter 2 outlines the fundamental theory of the semi-classical light-matter interaction to describe the effect of an atomic medium on the interacting optical field. Chapter 3 details the measurement principle of tracking electron beam magnetic fields, including more specific theory, design, and results using the simplest magnetometer configuration. In chapters 4 and 5, the classical sensitivity limit of the detector outlined in chapter 3 is surpassed through the use of four-wave mixing and far-detuned magnetometry. Finally, we summarize our work and discuss technological and fundamental improvements to the prototype particle detector in chapter 6.

Chapter 2

Fundamental Theory

This section outlines the fundamental theory describing the mechanisms behind the magnetic field detector. First, we build the light-matter interaction by representing the optical field classically and the atom via discrete quantum states. Next, we introduce the density matrix formalism to realistically model the interactions with an external quantum state reservoir that is otherwise not permitted in a pure state quantum formalism. Finally, the end of the chapter will model the effects on incident light due to the generalized density matrix structure of the given atomic energy state configuration. We postpone the detailed discussion of the quantum state configurations for magneto-optical rotation, four-wave mixing, and far-detuned magnetometry to chapters 3, 4 and 5 to preserve continuity.

2.1 Wave Propagation In Atomic Mediums

We start by considering the effect of an atomic medium on an incident electromagnetic field. Traditionally, we start with the general Maxwell's equation for electromagnetic fields:

$$\nabla \cdot \boldsymbol{D} = \rho \qquad \nabla \times \boldsymbol{E} + \frac{\partial \boldsymbol{B}}{\partial t} = 0$$
$$\nabla \cdot \boldsymbol{B} = 0 \qquad \nabla \times \boldsymbol{H} = \boldsymbol{J} + \frac{\partial \boldsymbol{D}}{\partial t}$$

Where $\boldsymbol{D} = \epsilon_0 \boldsymbol{E} + \boldsymbol{P}$ is the displacement field, $\boldsymbol{H} = \frac{\boldsymbol{B}}{\mu_0} - \boldsymbol{M}$ the magnetizing field including electric $\boldsymbol{E}$ and magnetic $\boldsymbol{B}$ components that make up the optical field, $\boldsymbol{P}$ the medium polarization, $\boldsymbol{M}$ the medium magnetization, ρ the charge density, $\boldsymbol{J}$ the current density, and ϵ_0, μ_0 the vacuum permittivity and permeability, respectively. The atomic vapor is made up of neutral atoms thus, $\rho = \boldsymbol{J} = 0$ interacting with an optical field that does not induce bulk magnetization in the medium $\boldsymbol{M} = 0$ and the interactions between the atoms and electromagnetic field make up a macroscopic polarization through an induced atomic dipole moment resulting in $\boldsymbol{P} \neq 0$. Introducing these simplifications result in modified Maxwell's equations:

$$\nabla \cdot (\epsilon_0 \boldsymbol{E} + \boldsymbol{P}) = 0 \qquad \nabla \times \boldsymbol{E} + \frac{\partial \boldsymbol{B}}{\partial t} = 0$$
$$\nabla \cdot \boldsymbol{B} = 0 \qquad \frac{1}{\mu_0} \nabla \times \boldsymbol{B} - \epsilon_0 \frac{\partial \boldsymbol{E}}{\partial t} - \frac{\partial \boldsymbol{P}}{\partial t} = 0$$

To further simplify, we evaluate $\nabla \times \nabla \times \boldsymbol{E}$, substitute $\nabla \times \boldsymbol{B}$, and reduce $\nabla \times \nabla \times \boldsymbol{E} = -\nabla^2 \boldsymbol{E} + \nabla(\nabla \cdot \boldsymbol{E})$ by considering an isotropic medium where $\nabla \cdot \boldsymbol{E} = 0$, leading to the wave equation in a polarized medium

$$-\nabla^2 \boldsymbol{E} + \frac{1}{c^2} \frac{\partial^2 \boldsymbol{E}}{\partial t^2} = -\mu_0 \frac{\partial^2 \boldsymbol{P}}{\partial t^2}, \tag{2.1}$$

for $\mu_0 \epsilon_0 = c^{-2}$. The medium is made up of N atoms resembling electric dipoles made between the atomic nucleus and valence electron so we can define the polarization of the medium as

$$\boldsymbol{P} = N\boldsymbol{d} = -Ne\boldsymbol{r}, \tag{2.2}$$

for electric dipole moment $\boldsymbol{d} = -e\boldsymbol{r}$. We can consider the general plane wave solution using complex vector amplitudes

$$\boldsymbol{E}(\boldsymbol{r},t) = \frac{1}{2}\mathcal{E}_0(\boldsymbol{r},t)\hat{\mathcal{E}}e^{i(\boldsymbol{k}\cdot\boldsymbol{r}-\omega t)} + c.c. \qquad \boldsymbol{P}(\boldsymbol{r},t) = \frac{1}{2}\mathcal{P}_0(\boldsymbol{r},t)\hat{\mathcal{P}}e^{i(\boldsymbol{k}\cdot\boldsymbol{r}-\omega t)} + c.c. \tag{2.3}$$

For $\boldsymbol{k}$ the wave vector, $|\boldsymbol{k}| = \frac{2\pi}{\lambda}$, ω the light frequency, $\mathcal{P}_0$ and $\mathcal{E}_0$ the medium polarization and light amplitudes, each with directions $\hat{\mathcal{P}}, \hat{\mathcal{E}}$. We have additionally included *c.c.* to denote the complex conjugate to simplify future expressions involving electric field and polarization. If we consider plane wave propagation in the z-direction and plug equations 2.3 into equation 2.1 we end up with

$$\begin{aligned}\frac{1}{2}(k^2\mathcal{E}_0 - 2ik\frac{\partial\mathcal{E}_0}{\partial z} - \frac{\partial^2\mathcal{E}_0}{\partial z^2} + \frac{\omega^2}{c^2}\mathcal{E}_0 - \frac{2i\omega}{c^2}\frac{\partial\mathcal{E}_0}{\partial t} + \frac{1}{c^2}\frac{\partial^2\mathcal{E}_0}{\partial t^2})e^{i(kz-\omega t)}\hat{\mathcal{E}} + c.c. \\ = \frac{1}{2}(\omega^2\mu_0\mathcal{P}_0 + 2i\omega\mu_0\frac{\partial\mathcal{P}_0}{\partial t} - \mu_0\frac{\partial^2\mathcal{P}_0}{\partial t^2})e^{i(kz-\omega t)}\hat{\mathcal{P}} + c.c.\end{aligned} \tag{2.4}$$

We restrict ourselves to slow-varying terms through the slowly-varying approximation for $\mathcal{E}_0$ and $\mathcal{P}_0$ such that

$$\frac{\partial\mathcal{E}_0}{\partial z} \ll k\mathcal{E}_0 \qquad \frac{\partial\mathcal{E}_0}{\partial t} \ll \omega\mathcal{E}_0, ck\mathcal{E}_0 \qquad \frac{\partial\mathcal{P}_0}{\partial t} \ll \omega\mathcal{P}_0, ck\mathcal{P}_0 \tag{2.5}$$

$$\frac{\partial^2\mathcal{E}_0}{\partial z^2} \ll k\frac{\partial\mathcal{E}_0}{\partial z} \qquad \frac{\partial^2\mathcal{E}_0}{\partial t^2} \ll \omega\frac{\partial\mathcal{E}_0}{\partial t} \qquad \frac{\partial^2\mathcal{P}_0}{\partial t^2} \ll \omega\frac{\partial\mathcal{P}_0}{\partial t}, \tag{2.6}$$

and keeping the first-order terms then we obtain the wave propagation in the atomic medium:

$$\left(\frac{\partial\mathcal{E}_0}{\partial z} + \frac{1}{c}\frac{\partial\mathcal{E}_0}{\partial t}\right) = -\frac{k}{2i\epsilon_0}\mathcal{P}_0 \tag{2.7}$$

2.2 Macroscopic Polarization of the Medium

The response to electric fields for linear and isotropic polarized mediums is related through the susceptibility, χ

$$\boldsymbol{P} = \epsilon_0 \chi \boldsymbol{E} = N\boldsymbol{d}, \tag{2.8}$$

where, in general, χ is complex, and can be written in terms of real $\chi' = \mathrm{Re}(\chi)$ and imaginary $\chi'' = \mathrm{Im}(\chi)$ parts. To gain intuition of the effects of susceptibility, we can consider *steady-state* wave propagation through the medium:

$$\frac{\partial \mathcal{E}_0}{\partial z} = \frac{ik}{2\epsilon_0}\mathcal{P}_0 = \frac{k}{2}(i\chi' - \chi'')\mathcal{E}_0 \tag{2.9}$$

$\mathcal{E}_0$ is generally complex so writing it in polar form, $\mathcal{E}_0 = \mathcal{E}_0(z)e^{i\phi(z)}$ and splitting the real and imaginary parts into 2 differential equations results in the propagation of amplitude and phase in the medium

$$\frac{\partial \mathcal{E}_0}{\partial z} = -\frac{k\chi''}{2}\mathcal{E}_0 \qquad \frac{\partial \phi}{\partial z} = \frac{k\chi'}{2} \tag{2.10}$$

In the case of a uniform medium (and equivalent susceptibility) the solutions are

$$\mathcal{E}_0(z) = \mathcal{E}_0(0)e^{-\alpha z} \qquad \phi(z) = \frac{k\chi'}{2}z + \phi(0) \tag{2.11}$$

From these solutions, we recognize that $\chi'' = \mathrm{Im}(\chi)$ governs the *optical absorption* through the absorption coefficient $\alpha = k\chi''/2$. The real part of the susceptibility $\chi' = \mathrm{Re}(\chi)$ is seen to control the *phase* or *dispersion* of the light in the medium, connected to the refractive index for the medium

$$n = \sqrt{\epsilon_r} \approx 1 + \frac{\chi'}{2}, \tag{2.12}$$

for $\epsilon_r = 1 + \chi'$ the relative permittivity of the optical medium using the assumption that $\chi' \ll 1$. The electric field solution to the wave equation becomes:

$$\boldsymbol{E} \propto \exp\left[i\left(\frac{2\pi}{\lambda}(1+\frac{\chi'}{2})z-\omega t\right)\right] \tag{2.13}$$

2.3 Atomic Quantum Dipole Moment

To calculate the average dipole moment, we evaluate the expectation value of the dipole operator with respect to atomic wave function, $|\psi\rangle = \sum_\alpha c_\alpha|\alpha\rangle$, which is made up of various atomic basis states, $|\alpha,\beta\rangle = |nlm\rangle$ for n the principle (or radial) quantum number, l the total angular momentum quantum number, and m the z-component of total angular momentum l. At this point, a proper basis can be chosen to represent angular momentum, l and m, in the atomic wavefunctions. One can work in the fine structure basis $\boldsymbol{J} = \boldsymbol{L}+\boldsymbol{S}$ for $\boldsymbol{L}$ the valence electron orbital angular momentum and $\boldsymbol{S}$ the atomic spin angular momentum, or hyperfine basis $\boldsymbol{F} = \boldsymbol{J}+\boldsymbol{I}$ to include the nuclear spin angular momentum $\boldsymbol{I}$. In these bases, the angular momentum values can take on values $|L-S| \leq J \leq |L+S|$ and $|J-I| \leq F \leq |J+I|$, while the z-component quantum numbers take on values $-|J| \leq m_J \leq |J|$ and $-|F| \leq m_F \leq |F|$.

To choose a basis, we assert that the magnitude of applied magnetic fields causes energy level shifts much smaller than the hyperfine splitting of the Rb ground states (~ 3 GHz). As a result, the hyperfine structure becomes a suitable angular momentum basis to work in such that $l \to F$ and $m \to m_F$ to make up the atomic wave function $|nFm_F\rangle$ [59].

For all combinations of atomic wavefunctions $|\alpha\rangle, |\beta\rangle$:

$$\boldsymbol{P} = N\langle\boldsymbol{d}\rangle = N\langle\psi|\boldsymbol{d}|\psi\rangle = N\sum_{\alpha,\beta}\rho_{\alpha\beta}\wp_{\alpha\beta}, \tag{2.14}$$

in terms of the probability $\rho_{\alpha\beta}$ and transition dipole moment $\wp_{\alpha\beta} = \langle\alpha|\boldsymbol{d}|\beta\rangle$.

In general, the sum has many terms but they can be reduced through symmetry arguments and selection rules. The majority of the transition schemes we employ uses a

Λ scheme shown in figure 2.1 for the simplest hyperfine $F = 1 \rightarrow F' = 0$ scheme. In this configuration, two components of circular polarization $\sigma_{\pm}$ and a linear z-polarized π light interact with a common excited state.

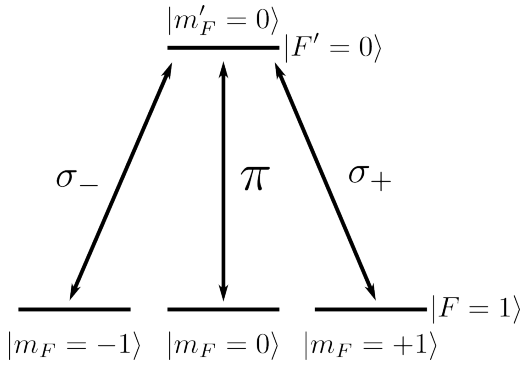


Figure 2.1: Λ transition scheme for the $F = 1 \rightarrow F' = 0$ transition, showing the 3 possible transitions using left circularly polarized σ_-, z-polarized π, and right circularly polarized σ_+ resonant light.

The nontrivial transitions can be evaluated first through the odd parity of the hydrogen atom wavefunctions, enforcing that $\Delta L = \pm 1$ for the angular momentum [60] . The selection rules for the z-component of that atomic angular momentum follows from the orthogonality of the spherical harmonics $Y_l^m(\theta, \phi)$ where the only non-vanishing contributions arise from $\Delta m = 0, \pm 1$ [61, 62]. If the electromagnetic field is written in a circularly polarized basis, then the transition dipole moment $\langle \alpha | \boldsymbol{d} \cdot \boldsymbol{E} | \beta \rangle$ will reduce to three nontrivial cases corresponding to left circularly polarized $\Delta m = -1$, z-polarized $\Delta m = 0$, and right circularly polarized $\Delta m = +1$ transitions.

When incorporating the external magnetic field, an additional term is included in the Hamiltonian, $H_{\text{Zeeman}} = -\boldsymbol{\mu} \cdot \boldsymbol{B}$, between the atomic magnetic moment $\boldsymbol{\mu}$ and applied magnetic field $\boldsymbol{B}$. This additional magnetic term in the Hamiltonian will have similar selection rules depending on the orientation of the magnetic field relative to the quantization axis, where a parallel B-field and laser propagation direction engages the $\Delta m_F = \pm 1$ transitions between ground state m_F levels (i.e. Faraday configuration), while perpendicular magnetic field and laser propagation direction engages the $\Delta m_F = 0$ transitions (i.e.

Voigt configuration) [63].

2.4 Density Matrix Formalism

In typical quantum mechanics we use atomic wavefunctions, which are superpositions of pure basis states $|\psi\rangle = \sum_\alpha c_\alpha |\alpha\rangle$. In this case the evolution of the system is given by

$$i\hbar \frac{\partial |\psi\rangle}{\partial t} = H|\psi\rangle, \tag{2.15}$$

for H the Hamiltonian for the quantum system. In the pure state formalism, probability is conserved and normalized to unity and only superpositions of *pure* states are allowed. However, in the case of atomic states being lost to decoherence, spontaneous emission, or transit away from the system, this system must be described as an ensemble of pure states in a statistical mixture.

Instead, we use a formalism that includes averages of statistical ensembles and mixture of atomic wave functions. Further, this formalism allows for sources of decoherence, interactions in an open system, and transitions between atomic wavefunctions (i.e. coherences). As a result, this approach conserves the density of atomic wavefunctions, rather than the basis states. To realize the benefits of this formalism, we define the density operator

$$\rho = \sum_{\alpha,\beta} |\psi_\alpha\rangle\langle\psi_\beta| \tag{2.16}$$

The expectation value of this operator yields the probability of the system being represented by the atomic wavefunction:

$$\langle\alpha|\rho|\beta\rangle = \langle\alpha|\psi_\alpha\rangle\langle\psi_\beta|\beta\rangle \tag{2.17}$$

$$\rho_{\alpha\beta} = c_\alpha c_\beta^* \tag{2.18}$$

$$\rho_{\alpha\alpha} = |c_\alpha|^2 \tag{2.19}$$

which is identical to the pure state case, but now allows for mixtures of basis states. To determine the time evolution of the density operator, we make use of equation 2.15

$$\frac{\partial \rho}{\partial t} = \frac{\partial}{\partial t}|\psi\rangle\langle\psi| = \frac{1}{i\hbar}[H, \rho] \tag{2.20}$$

which determines the time evolution of ρ with respect to the Hamiltonian of the given system. Therefore, the medium polarization $\boldsymbol{P}$ in equation 2.14 can now be written in terms of the density matrix elements $\rho_{_{\alpha\beta}}$ solved for in equation 2.20.

The power of the density matrix formalism is that decoherences can be added to the time-evolution equation in the simple addition:

$$i\hbar\frac{\partial \rho}{\partial t} = [H, \rho] + \mathcal{L}(\rho), \tag{2.21}$$

known as the Linblad master equation [64] where $\mathcal{L}$ contains all decays and decoherences of the system due to spontaneous decay, Doppler broadening, collisional broadening, transit decay, and other sources of spectral line broadening [65–67].

To summarize, the susceptibility of the medium affects the electric field of the incident optical field through equations 2.11. The susceptibility is calculated through equation 2.8, which depends on the expectation value of the dipole moment of the atoms evaluated through equations 2.14 and 2.20 for a given system Hamiltonian. Therefore, if we evaluate the Hamiltonian of the system and solve for the density matrix elements, we can determine the effect on the incident resonant light.

All future density matrix calculations assume a steady-state solution for density matrix elements, $\frac{d\rho}{dt} = 0$, since most effects occur on much longer time scales than atomic phenomenon and in following chapters, we consider the specific cases for each atomic energy scheme with the intention of linking back to the fundamental theory outlines in this chapter.

Chapter 3

Electron Beam Magnetic Field Detection

This chapter presents the methodology and results of imaging the electron beam magnetic field and extracting current density that generates the field. We start by outlining the classical magneto-optical effect coupling magnetic fields to optical polarization through the Faraday effect, then we discuss quantum properties of atoms to enhance magnetic field sensitivity. The theoretical discussion concludes with how electron beam current density is extracted from the measured magnetic field. The second half of the chapter discusses the experimental setup used to image the electron beam magnetic field, concluding with electron beam profile verification by comparing position, width and total current to secondary diagnostics discussed within the chapter.

3.1 Classical Magneto-Optical Coupling

The first demonstration of magneto-optical coupling was pioneered in the work of Faraday through the Faraday effect, as outlined in figure 3.1(a). A linearly polarized optical field propagates through an optical medium with magneto-optical properties characterized by Verdet constant ν under the influence of a uniform magnetic field B along length L. The

output polarization will be rotated by an angle β linearly proportional to the applied magnetic field as given by equation 3.1.

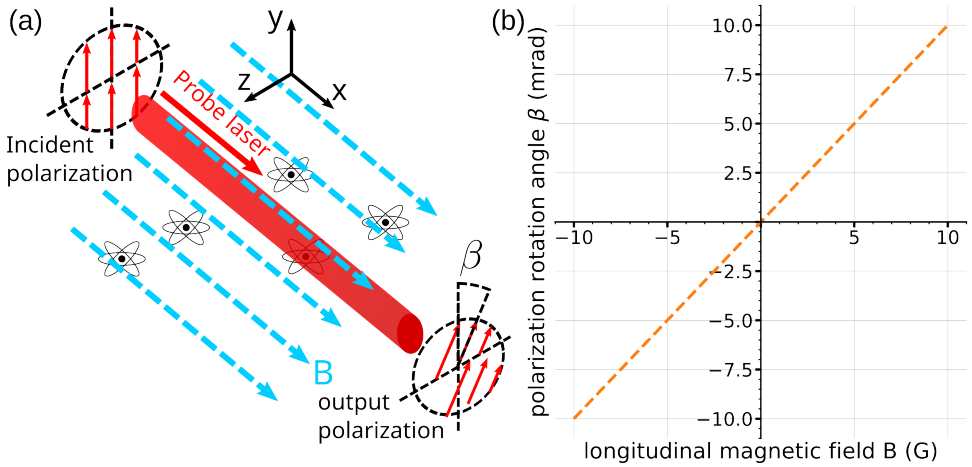


Figure 3.1: (a) Mechanism of the classical Faraday effect. (b) linear response of the polarization rotation angle β due to magnetic field magnitude B for $L = 1$ mm and $\nu = 1$.

$$\beta = \nu B L \tag{3.1}$$

This response is due to the differential birefringent coupling to the left- and right-circular polarization components that make up the linear polarization angle of the incident optical field [68]. Due to the differences of the indices of refraction for each circular polarization component in the presence of a magnetic field, the overall polarization angle rotates by an amount proportional to the propagation distance L. In this classical configuration, the sensitivity to magnetic field is governed by the slope of the linear response $d\beta/dB$ in figure 3.1(b), which is highly dependent on the Verdet constant ν governed by the properties of the optical medium. In general, this sensitivity is quite small and highly dependent on temperature of the material and wavelength of the interacting optical field [69]. However, we can show that by considering the quantum properties of the atomic medium, we can achieve high sensitivity to the magnetic field and strengthen the coherent coupling between resonant optical fields and the optical medium.

3.2 Nonlinear Magneto-Optical Rotation

We now consider the semi-classical interaction between the classically-defined electromagnetic field and the atomic-based medium, defined through quantum states. While the general theoretical approach was set up in chapter 2, here we narrow the scope to the simplest configuration of magneto-optical rotation derived by Budker and Matsko [70, 71], as well as highlight the advantages of the nonlinear response of the atomic vapor medium to applied magnetic fields.

In the presence of a magnetic field, the magnetically-sensitive quantum states of the atoms are shifted by a proportional amount due to the Zeeman effect shifting the resonances of these atomic states. These states interact with resonant optical fields through left- and right-handed circular polarizations, resulting in an overall rotation of the linear polarization angle of light proportional to the magnetic field sensed by the atoms. The non-linearity in nonlinear magneto-optical rotation (NMOR) indicates that the birefringence originates from nonlinear (laser intensity-dependent) optical susceptibility. Since the magnetic field induced shifts in atomic energy states are small compared to the hyperfine splitting of the transition (400 – 800 MHz for Rb D_1 transition), the F angular momentum states including nuclear spin angular momentum will be used for magnetic field sensing. The simplest NMOR interaction scheme is provided in figure 3.2(a), showing a simplified NMOR interaction scheme consisting of two Zeeman sublevels of the ground electronic states $|m_F = \pm 1\rangle$, coupled to the $|m_{F'} = 0\rangle$ excited state via two circular polarization components $\Omega^{\pm}$ of the linearly polarized near-resonant laser field, forming a so-called Λ scheme. Indeed, in the configuration where the magnetic field is parallel to the laser propagation axis, the selection rules determine that the circular components only allow transitions between $\Delta m_{F \to F'} = \pm 1$. In the absence of a magnetic field, the two ground state Zeeman sublevels are degenerate. In the case where a weak magnetic field B is present, the Zeeman energy shift for the $m_F = \pm 1$ levels is given by equation 3.2

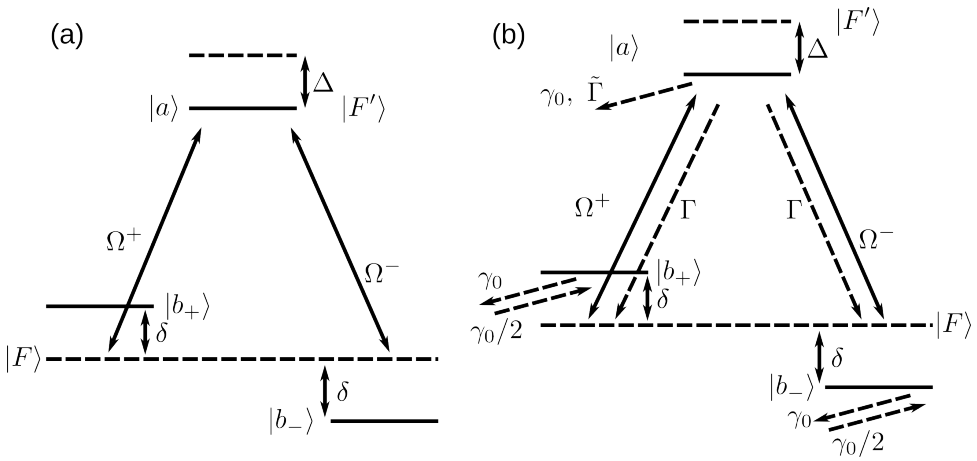


Figure 3.2: (a) simplified energy level scheme for the closed NMOR system, without decoherences. States $|b_+\rangle$,$|b_-\rangle$, and $|a\rangle$ correspond to $|m_F = +1\rangle$, $|m_F = -1\rangle$ and $|m_{F'} = 0\rangle$ states, respectively. (b) NMOR scheme for the open system, including decoherences and pumping terms due to spontaneous emission Γ, transit decoherence γ_0, decays to external states $\tilde{\Gamma}$ and repumping $\gamma_0/2$ decoherences.

$$\hbar\delta_{m_F} = g_F\mu_B m_F B = \gamma B, \tag{3.2}$$

for g_F is the hyperfine structure Lande g-factor, μ_B the Bohr magneton, m_F the Zeeman hyperfine sublevel, and B the magnitude of the magnetic field along the laser propagation path. The hyperfine g-factor has a correction to its value through equation 3.3, where g_J is the well tabulated fine structure Lande g-factor [59, 72], which is used to calculate the gyromagnetic ratio $\gamma = 5$ Hz/nT for ^{85}Rb.

$$g_F = g_J \frac{F(F+1) - I(I+1) + J(J+1)}{2F(F+1)} \tag{3.3}$$

To show the sharp response of the light-matter interaction in the presence of the external magnetic field, we can calculate the wave functions corresponding to $H|\psi\rangle = 0$ with the following Hamiltonian governed by the energy scheme in figure 3.2(a)

$$H = \hbar\delta|b_+\rangle\langle b_+| - \hbar\delta|b_-\rangle\langle b_-| + \hbar\Delta|a\rangle\langle a| + \hbar\Omega_+|b_+\rangle\langle a| + \hbar\Omega_-|b_-\rangle\langle a| + H.C. \tag{3.4}$$

where Δ is the detuning of the excited state from resonance, $H.C.$ the hermitian con-

jugate of the previous terms, and $\Omega_\pm = \wp_\pm E_\pm/\hbar$ are the Rabi frequencies of the left- and right-circular polarization components of the optical field, with $\wp_\pm$ the transition dipole moments and $E_\pm$ the electric field amplitudes of the birefringent optical field. The eigenenergies λ for the system are given by:

$$\begin{vmatrix} \delta-\lambda & \Omega_+ & 0 \\ \Omega_+^* & \Delta-\lambda & \Omega_- \\ 0 & \Omega_-^* & -\delta-\lambda \end{vmatrix} = (\delta-\lambda)[(\Delta-\lambda)(-\delta-\lambda) - |\Omega_-|^2] - |\Omega_+|^2(-\delta-\lambda)] = 0. \quad (3.5)$$

In the degenerate case where $\delta = 0$, the eigenvalues and eigenvectors can be found through the characteristic equation,

$$\lambda^2(\Delta-\lambda) + (|\Omega_+|^2 + |\Omega_-|^2)\lambda = 0 \quad (3.6)$$

$$\lambda_D = 0 \qquad \lambda_{B_{+,-}} = \frac{\Delta}{2} \pm \sqrt{\frac{\Delta^2}{4} + |\Omega_+|^2 + |\Omega_-|^2} \quad (3.7)$$

$$|D\rangle = \frac{\Omega_+|b_+\rangle - \Omega_-|b_-\rangle}{\sqrt{|\Omega_+|^2 + |\Omega_-|^2}} \qquad |B_{+,-}\rangle = \sqrt{\frac{|\lambda_{B_{+,-}}|}{\lambda_{B_+} - \lambda_{B_-}}}\left(|a\rangle + \frac{\Omega_+^*}{\lambda_{B_{+,-}}}|b_-\rangle + \frac{\Omega_-^*}{\lambda_{B_{+,-}}}|b_+\rangle\right) \quad (3.8)$$

resulting in the most remarkable property of such an interaction scheme due to the existence of a so-called "dark state" $|D\rangle$ that can be completely decoupled from the excited state $|a\rangle$ in the absence of the magnetic field (and thus does not produce fluorescence, giving the state its name). Atoms in such state (assuming no decoherence) do not absorb light, giving rise to the effect of electromagnetically induced transparency (EIT) [66, 73, 74]. The resulting optical interaction is extremely sensitive so that even small variations of the ground state energies due to the Zeeman shifts δ in equation 3.2 produce noticeable differences in the interactions with two circular laser polarization components.

While the sharp optical response is demonstrated through the derivation of equation 3.8 following the scheme of Figure 3.2(a), it is far from realistic due to the lack of decohering processes present in actual experimental implementations. The realistic energy scheme is

outlined in Figure 3.2(b), including various decoherences $\Gamma, \tilde{\Gamma}$, and γ_0 to simulate decays to m_F ground states, decays to external atomic states, and incoherent pumping and decay rates (*e.g.*, atoms entering and leaving the probe laser interaction region), respectively.

One can obtain the accurate solution for the optical susceptibility for the two circular components by solving equation 2.21 for the density matrix elements [70, 71]:

$$\chi_{\pm} = \frac{i\alpha_0\lambda}{\pi}\frac{(\gamma_0\Gamma_{EIT} + 4\delta^2) - i\delta\Gamma_{EIT}}{4\delta^2 + \Gamma_{EIT}^2}, \tag{3.9}$$

where $\alpha_0 = \frac{\wp_{\alpha\beta}^2 N}{2\epsilon_0\hbar\Gamma}$ is the unsaturated optical resonant absorption, $\wp_{\alpha\beta}$ is the electric dipole moment of the optical transition, N is the atomic density, and γ_0, Γ are the decoherence rates from each state and spontaneous decay of the excited state in figure 3.2(b), respectively. Here, $\Gamma_{EIT} = \gamma_0 + \frac{\wp_{\alpha\beta}^2}{c\epsilon_0\hbar^2\Gamma}I$ is the power-broadened width of the EIT resonance, where I is the laser intensity. Using this expression, we can determine the variation in the laser intensity and polarization rotation angle as light propagates through the atomic ensemble for a small magnetic shift $\delta_B \ll \Gamma_{EIT}$ using equations 2.10:

$$\frac{dI}{dx} = -\alpha_0\frac{\Gamma_0}{\Gamma_{EIT}}, \tag{3.10}$$

$$\frac{d\varphi}{dx} = \alpha_0\frac{\Gamma\delta}{\Gamma_{EIT}^2}. \tag{3.11}$$

Substituting Γ_{EIT} and in the limit of negligible ground state spin decoherence ($\gamma_0 \ll \Gamma_{EIT}, \Gamma$) and small laser intensity variation the polarization rotation rate reduces to

$$\left.\frac{d\varphi}{dx}\right|_{B\approx 0} = \frac{\hbar c N}{\lambda I}\gamma B, \tag{3.12}$$

in the case of long spin coherence lifetime and exact optical resonance. We assume the greatest contribution to φ is when the probe beam direction and magnetic field B are along the x-axis; λ, I, and c are the wavelength, local intensity, and speed of light, respectively; N is the density of the Rb vapor, and $\gamma = 5$ Hz/nT is the gyromagnetic ratio for ^{85}Rb atoms. Figure 3.3 shows the sensitivity comparison around zero longitudinal magnetic field

between the linear Faraday effect in equation 3.1 and nonlinear magneto-optical rotation in equation 3.12, where the nonlinear effect results in far greater sensitivity by comparing the relative slopes of the two curves. The sensitivity is determined by the slope of equation 3.11, $\alpha_0\Gamma/\Gamma_{EIT}^2$, with respect to Zeeman shift δ related to the magnetic field B by equation 3.2.

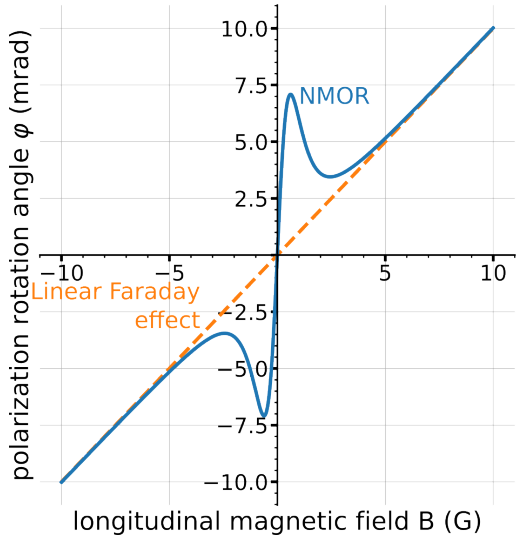


Figure 3.3: Sensitivity comparison between linear Faraday effect (orange dashed) with $L = 1$ mm, $\nu = 1$ and nonlinear magneto-optical rotation (solid blue) where $\frac{\hbar c N \gamma}{\lambda I} = 20$, $L = 1$ mm and the width of the resonance $\Gamma_{EIT} = 1$ from equations 3.12 and 3.11

In principle, since the intrinsic spin coherence lifetime $\gamma_0^{-1} \propto \Gamma_{EIT}^{-1}$ is very long, and in some experiments [75] was extended up to many seconds, NMOR-based magnetometers can achieve an impressive sub-pT sensitivity [28, 29]. When the spin decoherence and optical losses are accounted for, the exact proportionality coefficient between the polarization rotation rate and the applied magnetic field is more complex and depends, at some extent, on many experimental parameters (lifetimes of both optical spin states, laser frequency detuning from the optical resonance, influence of additional near-resonant atomic levels, etc.).

It is clearly seen that the slope, and therefore magnetic sensitivity, can be quite large due to the coefficient in equation 3.12, resulting in Verdet constants on the order of 10^4 rad

G^{-1} cm^{-1} compared to flint-based magneto-optical materials on the order of 10^{-5} rad G^{-1} cm^{-1} [76]. In the linear magneto-optical regime, the magnetic resonance width is limited by the optical line width on the order of MHz, whereas the nonlinear regime is limited by the coherence lifetime $T \sim 1/\Gamma$ on the order of Hz with the lambda energy level scheme in figure 3.2. This long-lived coherence is established around the dark state in equation 3.8, around zero magnetic field and on atomic resonance. Therefore, the combination of this energy scheme allows long coherence lifetimes to build sensitive atom magnetometers in a dilute rubidium vapor through equation 3.11.

3.3 Electron Beam Magnetic Profile & Current Density Reconstruction

Our experiment applies a spatially varying magnetic field due to the nature of the charged particle beam shown in figure 3.4 for an electron beam propagating in the z-direction and laser travelling in the x-direction. While this makes the magnetic field behavior more nontrivial, the geometry of the electron beam magnetic field allows us to derive essential charged particle beam parameters such as electron beam intensity, position and width through the following discussion.

To begin modelling the electron beam magnetic field, we reasonably assume that the electron beam has a Gaussian current density given by

$$\boldsymbol{j}(x,y) = \frac{\mathcal{I}_0}{\pi w^2} e^{-\frac{x^2+y^2}{w^2}} \hat{z}, \tag{3.13}$$

for electron beam propagation in the $\hat{z}$-direction, where $\mathcal{I}_0$ is the total current, and w is the beam $1/e^2$ half-width. Although this seems like a restrictive constraint to enforce, *a priori* knowledge of the electron beam distribution is not required if the vector information of the electron beam magnetic field is measured, discussed later in chapter.

The corresponding magnetic field maintains cylindrical symmetry along the polar direction $\hat{\theta}$, forming concentric field lines around the beam central axis which can be easily

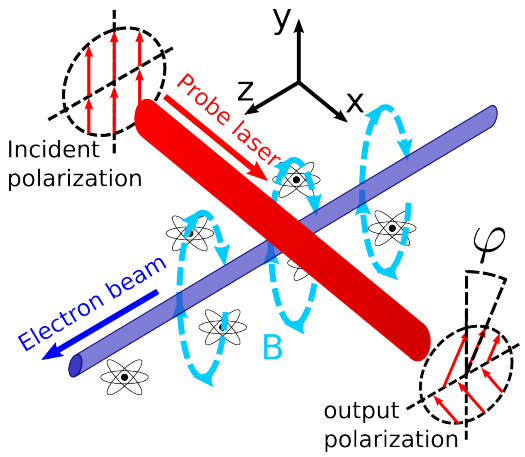


Figure 3.4: The basic concept of the charged particle beam detection method. The linear polarization of a probe laser beam (red) φ is affected by the magnetic field (dashed light blue circles) of an electron beam (dark blue) mediated by the spin coherence of Rb atoms.

found using Ampere's law:

$$\boldsymbol{B}(x,y) = \frac{\mu_0 \mathcal{I}_0}{2\pi\sqrt{x^2+y^2}} \left(1 - e^{-\frac{x^2+y^2}{w^2}}\right) \hat{\theta}, \tag{3.14}$$

where μ_0 is the magnetic permeability of free space.

We can obtain quantitative information about the e-beam current distribution from its magnetic field by deriving a function encoding beam parameters into a fit function derived from the measured magnetic field. We begin with what we measure, which is the total polarization rotation $\varphi(y,z)$ integrated along the detection region of length L characterized by coefficient $\beta(y,z)$ under the influence of a magnetic field B

$$\varphi(y,z) = \beta(y,z) \int_{-L/2}^{L/2} B_x(x,y)dx, \tag{3.15}$$

for small rotation angles $\varphi(y,z)$. We assume that the atomic interaction is constant along the laser propagation direction, the electron beam is collimated along z with no magnetic field dependence along z, and that the primary contribution to the polarization rotation angle is the magnetic field along the laser propagation direction $\hat{x}$ such that $\boldsymbol{B}(x,y) \to B_x(x,y)$. In this case any changes in the polarization rotation in the z-direction

can only be caused by the variation in the atomic response $\beta(y,z)$ due to, e.g., laser intensity variation.

Characterizing the atomic response generally requires evaluating atomic related properties such as atomic number density, transition dipole moments of all possible transitions, wavelength of the resonant optical field, etc. However, all of these constants are measurable through a straightforward evaluation if the applied magnetic field is known. If a uniform magnetic field is applied such that all positions within the laser interaction region experience the same magnetic field, then the only variation in atomic response is due to the light-matter interaction. Therefore, by measuring the spatial polarization rotation angle for a uniform magnetic field, equation 3.15 trivially reduces to

$$\varphi_0(y,z) = \beta(y,z) B_0 L, \tag{3.16}$$

and $\beta(y,z)$ is determined by normalizing the resulting rotation $\varphi_0(y,z)$ to the magnetic field magnitude B_0 and length of the interaction region L. By evaluating the spatial atomic interaction in this way, we encompass all optical interactions in this single coefficient for arbitrary optical transitions, atomic densities, and laser intensities.

Using equation 3.14, we can find an analytical expression for the polarization rotation for an electron beam centered at vertical location $y = y_0$:

$$\begin{aligned}\varphi(y,z) &= \beta(y,z)\frac{\mu_0 \mathcal{I}_0 (y-y_0)}{2\pi}\int_{-L/2}^{L/2}\frac{1-e^{-\frac{x^2+(y-y_0)^2}{w^2}}}{x^2+(y-y_0)^2}dx \\ &\approx \frac{\beta\mu_0\mathcal{I}_0}{2}\left[\operatorname{erf}\left(\frac{y-y_0}{w}\right) - \frac{2}{\pi}\arctan\left(\frac{2(y-y_0)}{L}\right)\right],\end{aligned} \tag{3.17}$$

where $\operatorname{erf}(x)$ is the error function, and we assume $e^{-L^2/4w^2} \ll 1$. For a larger cell the first term dominates the rotation, while the edge effects become more noticeable farther from the e-beam center and for interaction lengths on the order of electron beam width, as shown in the vertical polarization rotation profiles in figure 3.5

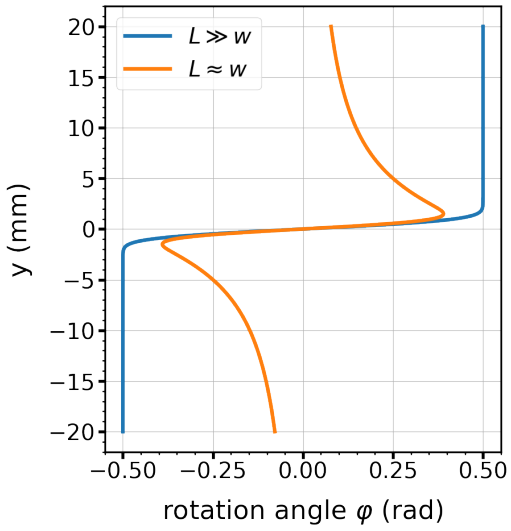


Figure 3.5: Effect of finite cell length L compared to electron beam width w on the polarization rotation profile $\varphi(y)$ generated from the electron beam magnetic field of equation 3.14 shown in figure 3.4. The rotation profile $\varphi(y)$ is evaluated from equation 3.17 for infinite cell length $L \gg w$ (blue) and finite cell length $L \approx w$ (orange), causing the tails of the profile to fall off far from the center of profile. These profiles were calculated for $\beta\mu_0\mathcal{I}_0 = 1$ rad, $y_0 = 0$ mm, $L = 10$ mm, and $w = 1$ mm, and is oriented to match the expected output polarization in the zy-plane from figure 3.4

It is convenient to introduce a normalized signal $\Phi(y,z) = \varphi(y,z)/(\mu_0\beta(y,z))$ since it depends only on the e-beam current distribution. For a Gaussian current distribution, according to equation 3.17, the normalized signal is an error function for $L \gg w$, centered at the vertical position of the e-beam y_0, and the maximum variation of $j(y,z)$ depends only on the total e-beam current, that allows for robust measurements of these parameters even for a noisy signals. Therefore by fitting the resulting magnetic field profile, one can obtain the current $\mathcal{I}_0$, center position y_0, and width w of the electron beam. Additionally, if a profile of the current distribution is required, it becomes as trivial as evaluating the derivative

$$j(y) = \frac{d\Phi}{dy}, \tag{3.18}$$

resulting in a Gaussian current distribution as expected in the case of $L \gg w$.

Therefore, to measure the Gaussian beam profile, the electron-induced NMOR $\varphi(y,z)$ needs to be normalized to the atomic response $\beta(y,z)$ obtained through equation 3.16.

Once normalized, the resulting vertical profile can be fit to equation 3.17 to extract the total current $\mathcal{I}_0$, position y_0, and width w. Optionally, by differentiating in the vertical direction, the current distribution can be mapped through equation 3.18. As a result, the current density can be reconstructed from the measured magnetic field distribution imaged in the experiment.

Two assumptions regarding this analysis is on the beam shape, and constraining the current density variation to the vertical axis. The assumption regarding the beam shape, however, is straightforward to neglect if magnetic field direction is measured. With magnitude and direction of the magnetic field, the vector can be constructed and the current density calculated through Ampere-Maxwell law:

$$\boldsymbol{\nabla} \times \boldsymbol{B} = \mu_0 \boldsymbol{j}, \tag{3.19}$$

in the steady state ($\partial \boldsymbol{E}/\partial t = 0$). Previous work has demonstrated a method for determining magnetic field direction based on NMOR transmission spectra [37] and structured light [36] for uniform fields of arbitrary direction, and by adapting the methods for electron beam magnetic fields, arbitrary current density reconstruction is attainable, thus loosening the constraint set on the electron beam current distribution.

More spatial dimensions can be included in the current density reconstruction by introducing an additional probe laser propagating in the y-direction in figure 3.4 to extract the magnetic field and current density along the x axis, resulting in a cross-sectional profile of the electron beam by using the analysis discussed in this section. With the two transverse reconstructions, the full cross-sectional area of the electron beam can be mapped, providing beam profiles obtainable through collisional based detectors mentioned in section 1.1. This transmission-based measurement integrates along the optical propagation path and discards any spatial magnetic field behavior along the laser axis. Rydberg atom spatial electric field sensing has been shown to spatially characterize electric field-induced energy level shifts along the laser propagation path using laser-induced fluorescence [16].

By applying the same principles of Rydberg EIT fluorescence to NMOR, this problem can likely be addressed to probe the magnetic fields within the electron beam and along the laser propagation path.

3.4 Electron Beam Profiling via NMOR

This section discusses the experimental apparatus made up of the electron gun, vacuum system and secondary electron beam diagnostics to generate, maintain, and characterize the electron beam. We start with the various features of the vacuum system and Rb vapor cell used in magnetic field detection. Then we discuss secondary diagnostics that can be used to characterize the electron beam profile to validate the beam properties measured using the magnetometer. Finally, we go over the optical setup and results of the electron beam profiles obtained by measuring the particle beam magnetic field using NMOR.

3.4.1 Tabletop Electron Beamline

The electron beam source is a device by STAIB instruments (model RH30) which is typically used for reflection-based high-energy electron diffraction (RHEED) imaging [77, 78] as a method of electron microscopy typically used for surface characterization of materials [79]. This source, however, is sufficient to generate a collimated and configurable electron beam to use for the tabletop charged particle beam profiler. The electrons are generated through a thermionic filament style source, where running high current through the filament heats it sufficiently so that it emits free electrons. Higher filament current yields greater total beam currents at the cost of filament lifetime due to the greater heating of the filament. An electric potential that focuses or diverges the electron cloud is applied through a conical "grid" element to collimate the emitted electrons. The electrons are finally accelerated up to 20 keV in a collimated beam to freely propagate through the system while being magnetically steered using two pairs of Helmholtz coils within the electron

gun. The result is a collimated electron beam with up to 200 μA of current accelerated between 10-30 keV, which can be focused to a 100 μm width with proper focusing.

This electron source can manipulate beam focus through a combination of "grid" and "focus" control voltages, and beam deflection in the horizontal X and vertical Y directions. Electron emission during the experiment is controlled through beam blanking, which completely diverges the electron beam through defocusing. Electron total current is therefore controlled by a combination of filament current, beam "grid", and beam "focus" controls.

X-ray protective measures are taken to minimize radiation exposure through the use of leaded materials to block the x-rays generated by electrons scattering into glass interfaces. In particular, the glass hot-cathode ionization gauge (I-HC) and downstream chamber optical access window in figure 3.6 are covered with lead to prevent x-ray exposure during the experiment. Exposure rates in the absence of shielding range from 2.07 rem/hr adjacent to glass interfaces down to 28 mrem/hr 12 inches away from the glass interface due to the rapid decrease in exposure rates at far distances. Since all glass interfaces are covered by leaded material, plastic or metal enclosures, or sufficient distance from working areas, the exposure to x-rays is negligible ($\leq$ 500 μrem/hr) compared to the unshielded case.

To generate an electron beam and profile the magnetic field, the vacuum system in figure 3.6 is kept at 1 – 10 nTorr to preserve the electron filament and rubidium alkali. The electron beam propagates through the upstream chamber, the rubidium cell, and the downstream chamber for a total propagation distance of 1 m.

The upstream chamber houses vacuum diagnostics to monitor vacuum pressure using cold- and hot-cathode pressure gauges to monitor low vacuum ($\leq$ 760 Torr) to ultra-high vacuum ($\leq$ 1 nTorr). Two optical access points are included to view downstream and perpendicular to the electron beam path for additional diagnostics and beam characterization.

The rubidium cell is a rectangular cuboid glass cell (inner dimensions: 10 mm $\times$ 10 mm $\times$ 45 mm) containing a natural abundance of Rb vapor designed to allow the electrons

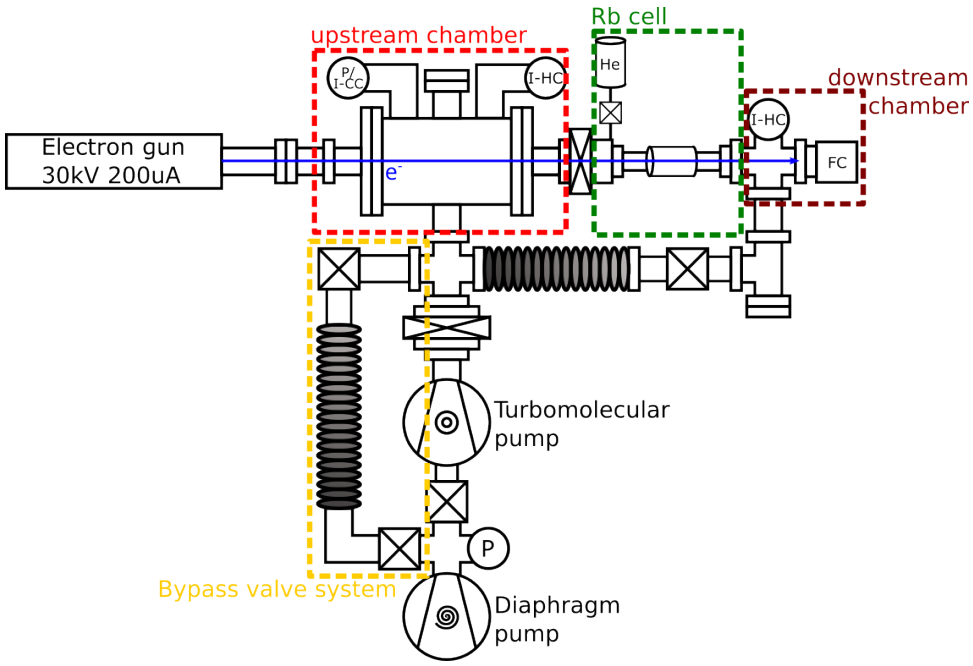


Figure 3.6: Representative diagram of the electron beam vacuum system. Inline, angle, and gate valves are all marked with an inscribed "X". Various Pirani (P), cold-cathode ionization (I-CC), and hot-cathode ionization (I-HC) pressure gauges monitor vacuum pressure around the system. Helium (He) or other gases can be pumped into the Rb cell. The electrons terminate in the Faraday cup (FC) to measure total current at the end of the system.

to pass through while keeping sufficient rubidium vapor pressure within the cell region. Differential pumping through 8 mm apertures, up- and down-stream of the cell, are used to confine the vapor to the cell and to keep it at constant pressure. The vapor was maintained at $\sim 60°$C, corresponding to a ^{85}Rb vapor density of 2.7×10^{11} cm^{-3}. Although there is no pressure gauge in the Rb cell, we estimate the pressure in the cell and downstream chamber to be ~ 1 μTorr, which is the maximum pressure read in the surrounding vacuum chambers after exposing the cell to vacuum and before pumping back down to ultra-high vacuum. The cell has two reservoirs for gases: one included as part of the cell to load and seal the rubidium ampoule, and another to fill the cell with an arbitrary gas for electron beam diagnostics. The rubidium reservoir can be heated to gradually include vapor in the detection area of the cell, while the gas inlet can be used to backfill the cell with inert gas to protect the alkali when the vacuum is opened or to measure electron beam impact

fluorescence using an inert gas like helium.

A heated-air oven encloses the cell to control Rb vapor density without parasitic magnetic fields from electronic heaters. The oven is designed with pneumatic, optical, and temperature sensing ports for efficient heating and monitoring, while still allowing optical access for magnetic field sensing. Heated air is delivered to the cell from a compressed air supply regulated by a flow controller (0 – 5 SCFM). The air subsequently passes through a pipe heated electronically using heater strips connected to a variac.

The downstream chamber houses more electron beam and vacuum diagnostics with a hot-cathode pressure gauge, another optical access port, and the Faraday cup. The Kimball Physics FC73-A Faraday cup is used to measure electron beam total current and energy spread using a series of conductive grids to read out the electron deposition into the Faraday cup. The cup can be fitted with a phosphor screen and energy retarding grid to measure beam profile and energy spread, but these have been removed to limit parasitic light and back-scattered electrons affecting electron beam measurements. A bias voltage ($\sim$ 50 – 300 V) can be applied to the Faraday cup output to minimize back-scattered electrons and increase detector efficiency shown in figure 3.7(a). Figure 3.7(b) shows the 20% change in measured beam current when applying bias voltages V_{FC} from -30 – +30 V, where only bias voltages $-10\ V \leq V_{FC} \leq 30\ V$ show appreciable change in beam current. Therefore, further biasing voltage is not expected to significantly improve the measurement efficiency of the Faraday cup.

To pump out the vacuum system, a turbomolecular (turbo) pump (70 L/S, Pfeiffer model TMU-071P) is backed by a diaphragm rough pump to bring the pressure to 10 nTorr, which is more than sufficient to preserve the alkali and electron source filament, operable for pressures $\leq 5\ \mu$Torr. For safe turbo pump operation, the rough pump should initially pump out the system down to 1 – 10 mTorr before activating the turbo to limit heat generation in the turbo. This initial rough pumping can be facilitated through the bypass valve system, which bypasses the turbo pump to bring the system to mTorr pressures without the need to power cycle the turbo pump through the initial pumping

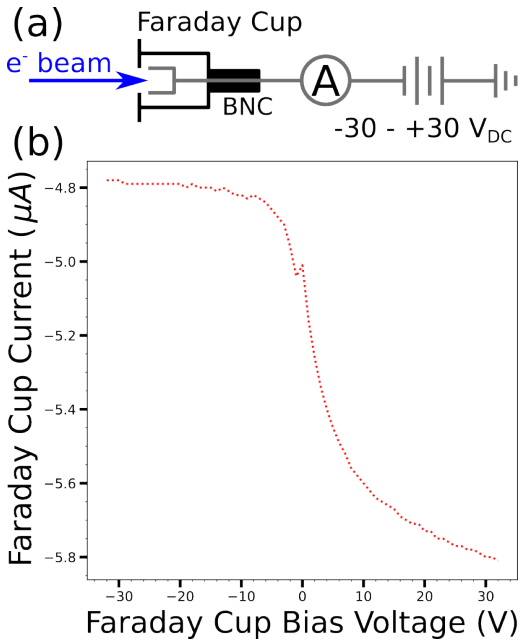


Figure 3.7: Effect of Faraday cup biasing on the measured electron beam current. (a) Scheme used to bias the Faraday cup, where the cup and surrounding vacuum system is grounded. (b) Change of Faraday cup current versus biasing voltage.

phase. To properly used the bypass, the valves surrounding the turbo can be closed to isolate the turbo, while the bypass valves can be opened until mTorr pressures are reached. After closing the bypass valves, the valves surrounding the turbo can be opened safely, starting with the valve facing the diaphragm pump, to pump down to ultra-high vacuum pressures.

To protect the vacuum from intermittent power outages, an automatic gate valve shuts in front of the pumps to limit the leakage of air into the system should the pumps lose power. This valve is pneumatically-controlled, and must be manually reset or opened to conserve the nitrogen gas supplied to the pneumatic gate valve. Two separate manual valves are placed to isolate the rubidium cell and downstream chamber from the rest of the system, allowing the vacuum to be exposed to air, while preserving the vacuum and enclosed alkali in this isolated region. Should work by done in the rubidium cell and downstream chamber, the gas inlet within the rubidium cell can be used to provide a constant flow of inert gas (e.g. nitrogen or argon) to limit the interaction of the alkali

with air. While this process can work for quick vacuum adjustments, more extensive vacuum work will require the rubidium alkali to be replaced. Details on these vacuum and electron gun procedures are listed in appendix B with step-by-step instructions on various processes to restore or maintain the vacuum system.

3.4.2 Electron Beam Characterization

We rely on several mechanisms to determine electron beam charge distribution and intensity using traditional profiling methods. To determine the total current of the electron beam, we use the emission current indicated by the electron source controller and the current measured on the Faraday cup. The Faraday cup current is measured through the voltage across a 50 Ω resistance BNC terminator. However, the current measured in the Faraday cup is subject to beam losses throughout the system, shown in figure 3.8, resulting in notably lower Faraday cup current compared to the emission current. This discrepancy arises from several factors, including potential beam clipping through the vacuum system, poor focusing and alignment of the electron source filament to the grid electrode, or back-scattered electrons reflected away from the Faraday cup. Despite these, however, we obtain coupling efficiency from 40% – 70% into the Faraday cup, as demonstrated in figure 3.8.

The Faraday cup can also be used to determine optimal beam pulse speeds and beam focus parameters. Since the beam blanking defocuses and refocuses the beam, there is a transient period before the electron beam is stable as demonstrated in figure 3.9(a) when the electron beam is turned on. The long transient times to collimate the beam constrains the pulse speeds to be limited to 1 Hz for stable beam profiles. Pulse rates up to 1 MHz using an electron pulser unit, which deflects the electrons through an aperture using electric fields [80], can speed up data acquisition, but this unit was not available for this apparatus. To optimize the beam focus at the Faraday cup, we sweep the electron beam position around the aperture of the Faraday cup (vertically, if considering the scheme shown in figure 3.7(a)) and tune the grid and focus parameters to maximize the width

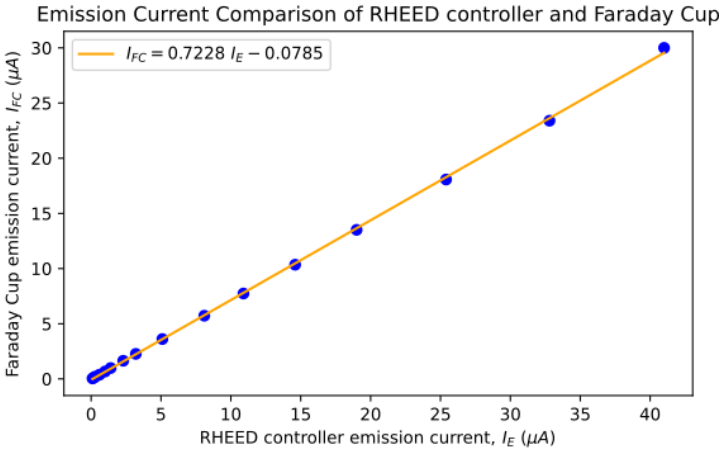


Figure 3.8: Coupling efficiency of the electron emission current into the Faraday cup (without any bias voltage) located 1 meter downstream of the electron gun. The coupling efficiency is evaluated using a linear fit (orange) to the data (blue).

and rise time of the measured current in figure 3.9(b).

In reality, the beam focus is a convolution of beam energy, filament current, grid, and focus parameters and is unlikely to be perfectly collimated throughout the length of the vacuum apparatus. Therefore, the electron beam profile is best compared within the rubidium cell using ionization (or impact) induced rubidium fluorescence. The fluorescence is generated after the ionized atoms recombine to neutral atoms, emitting light within the vicinity of where the ionization originally occurred. By imaging the resulting fluorescence, the beam profile can be mapped out to determine beam position and width with respect to the magnetometer probe region. The original fluorescence scheme used high pressures of helium to obtain beam profiles resulting in degradation of the electron source filament and rubidium supply due to the required high vapor pressure and gas impurities of the helium used, respectively. However, rubidium still undergoes the impact processes, albeit at a comparatively infrequent rate, to be able to extract fluorescence signals. Setting up an auxiliary imaging system with a magnification 1 (further discussion and configuration will be given in section 3.4.3), we obtained independent verification of the e-beam characteristics. Figure 3.10 shows examples of acquired fluorescence images due to the e-beam

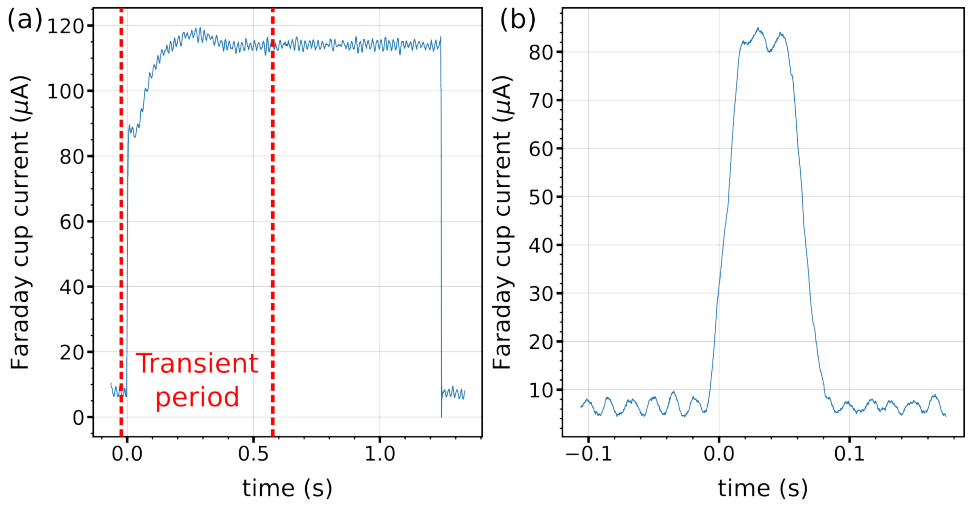


Figure 3.9: (a) e-beam current transient due to the refocusing of the electron beam when turning the beam on. (b) Faraday cup signal when sweeping the electron beam through the Faraday cup aperture.

for different vertical positions. We employed a camera with a 30-second exposure time to capture the fluorescence images, considering the low number of excited atoms that emit photons through fluorescence.

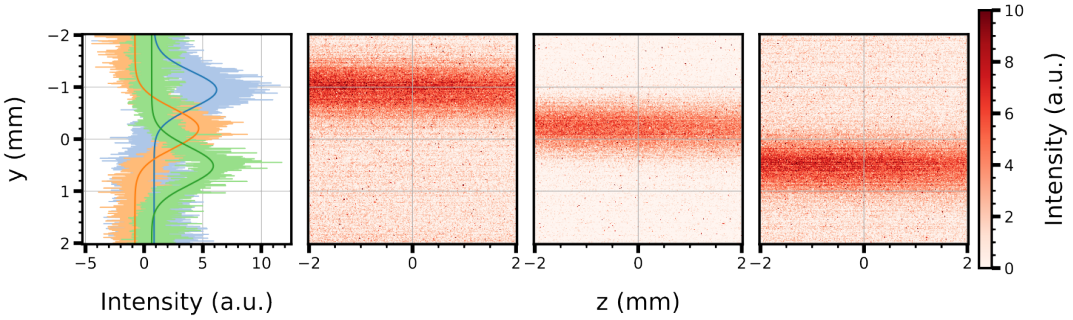


Figure 3.10: Electron beam impact fluorescence in Rb vapor at three different vertical positions of the electron beam. Each image uses 10 averages with a camera exposure of 30 s per average. The left-most plot shows the vertical profiles (transparent) and Gaussian fits (opaque) used to verify electron beam widths and positions. The images on the right are the fluorescence images captured by the fluorescence camera.

Using this fluorescence, we can measure the beam profile coincident to the magnetometer probe region to verify beam position and width measurements. Figure 3.10 also reveals the low interaction probability and frequency of the electrons and the atomic vapor, where

less than 10 fluorescence counts are captured over the span of 30 s exposure time. This argument, albeit not exhaustive, can be a measure of the non-invasive nature of this approach. Accurate measure of the interaction between the rubidium atoms and incident electron beam requires use of simulations such as GEANT4 [81–83] to fully characterize the processes, or lack thereof, between the electron beam and rubidium vapor.

Other beam diagnostics have been explored to accurately verify the electron beam characteristics, of which are outlined in figure 3.11. Optical transition radiation (OTR) is a phenomenon in which rapidly decelerated electrons emit optical radiation proportional to the electron beam intensity [84–86]. By imaging the resulting light, a profile can be mapped to verify the current density of the e-beam. Figure 3.11(a) shows an example of the radiation when the electron beam impacts the upstream differential pumping gasket between the upstream chamber and Rb cell in figure 3.6. However, the only optical access for OTR is on the upstream differential pumping aperture, located 6 inches upstream of the magnetometer probe region, making it unsuitable to validate the electron beam profile within the magnetometer probe region.

A harp (or wire) scanner in the detection region can also be used to extract the current density of the e-beam by reading out the current generated by electron deposition the wire as a function of scanner position [1]. Figure 3.11(b) shows a configuration for the wire scanner built to be used in the experimental apparatus, where 3 wires at 0° and $\pm 45^\circ$ are used to read out any ellipticity in the electron beam profile. However, the current Rb cell lacks a ConFlat vacuum flange near the magnetometer probe region, preventing implementation of the scanner that would greatly benefit the experiment as a diagnostic tool for total current within the detection cell. As a result, the system lacks a measure of beam current to validate within the probe region, discussed in section 3.5.

Finally, should electron impact-induced Rb fluorescence yield poor signal-to-noise ratio, higher pressures of inert gas can be used through the gas inlet valve attached to the Rb cell. Greater vapor pressures of inert gas generate more fluorescence that can be captured using cameras, as shown in figure 3.11(c) for $\sim$ 1 Torr He gas over short periods

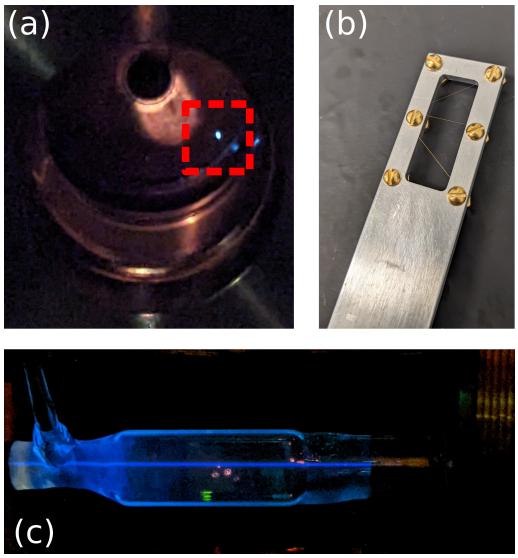


Figure 3.11: Alternative secondary diagnostics that can be used to measure the electron beam profile. (a) Optical transition radiation (OTR) of the electron beam impacting the solid copper gasket between the upstream chamber and Rb cell in figure 3.6. The dashed red box enclosing the blue light shows where the electron beam impacts the gasket. (b) Harp scanner made to profile the electron beam current density. The electrons deposited on the wire can be read out as a current while the wire scans across the electron beam, by mapping the current on the wires to the position of the scanner, the cross section of the electron beam can be read out. (c) Electron impact-induced helium fluorescence inside the Rb cell captured using a high-exposure cellphone camera. Propagating the electron beam through high helium pressure ($\leq$ 1 Torr) generates fluorescence, which can be used to measure the electron beam profile with greater signal-to-noise compared to Rb fluorescence in figure 3.10.

($\sim$ 1 s) to prevent electron source filament deterioration. Care *must* be taken to use high purity inert gas and evacuated supply lines to prevent alkali oxidation and cell window contamination to safely boost fluorescence signal using this diagnostic.

This summarizes the design of the vacuum system, and various methods to characterize the electron beam and compare to the magnetometer approach. The next section details the optical scheme and results in profiling electron beam magnetic fields using rubidium vapor.

3.4.3 Electron Beam Magnetic Field Profiling

The essence of the profiling approach is shown in Fig. 3.4. The e-beam travels through a cell containing a dilute gas of rubidium atoms. Within the cell each Rb spin precesses at a

rate determined by the local magnetic field. A linearly polarized laser beam traverses the volume surrounding the charge particle beam and probes the atomic spins: the nonlinear magneto-optical polarization rotation (NMOR) effect [18, 87, 88] rotates the optical linear polarization due to the magnetic field of the e-beam. By measuring the polarization rotation variation across the laser beam cross-section, we are able to determine the local magnetic field of the e-beam and reconstruct its transverse spatial profile. Our detection scheme is largely non-invasive as the e-beam is minimally affected by the low-density alkali vapor ($10^{10} - 10^{12}$ cm^{-3}) localized within a 30 cm region enclosed in high-vacuum. The strong resonant coupling between laser light and atomic spin coherence enhances the sensitivity compared to the approaches based on incoherent electron impact-induced fluorescence [10].

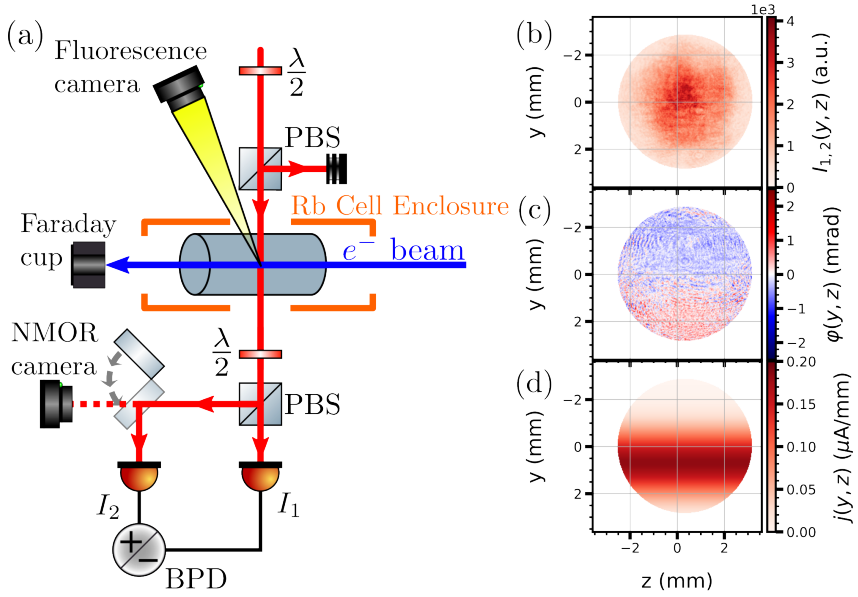


Figure 3.12: (a) Schematic of the experimental setup (see text for abbreviations), where a flipper mirror determines BPD- or CCD camera-based detection. (b) Laser intensity profile at the output of the PBS, recorded by the CCD with ~ 200 μs exposure time. (c) The e-beam-induced polarization rotation angle, $\varphi(y, z)$, calculated using equation 3.20. (d) The electron current density distribution reconstructed from the erf-function fit of the normalized polarization rotation $\Phi(y, z)$. For all the image analysis an intensity mask is applied to eliminate data points with laser intensity below 5% of the peak value to prevent infinities arising from $I_1 + I_2 = 0$ in equation 3.20

In the experiment, the laser beam propagates along the x-axis shown in Fig. 3.4, nearly

perpendicular to the electron beam direction, designated as the z-direction. The laser is linearly polarized in the y-direction, perpendicular to both the electron and the laser beam propagation directions. In this configuration, the laser polarization rotation should only be sensitive to the longitudinal magnetic field component B_x (Faraday configuration) [70].

Figure 3.12(a) shows the optical scheme for the simplest configuration to measure electron beam-induced NMOR. For optical detection, we use an external cavity diode laser (ECDL) operating on the D_2 line of ^{85}Rb (wavelength $\lambda = 780$ nm), operating within $\pm$50MHz of the $5^2S_{1/2}, F = 3 \rightarrow 5^2P_{3/2}, F' = 4$ transition. The laser frequency is stable enough to maintain consistent NMOR sensitivity fluctuations during data acquisition, so laser frequency locking was not used for the e-beam magnetic field measurements. The laser beam is linearly polarized using a polarizing beam splitter (PBS) cube and enlarged to 6 mm before the entering the Rb-filled glass cell to capture the full e-beam diameter. Since such system is most sensitive to small magnetic fields we suppress environmental fields by placing the atomic vapor cell inside a layer of μ-metal magnetic shielding, and use 3D Helmholtz coils to further reduce the background magnetic fields. After passing through the cell, the laser polarization rotation is analyzed using a balanced polarimeter, consisting of a half-wave plate that rotates the polarization by 45°, an analyzer PBS and a differential amplified photodetector (BPD). In the absence of the e-beam, the intensities of the two PBS outputs $I_{1,2}$ are balanced. A small rotation of the polarization φ produces a proportional variation between the two channel intensities, allowing accurate calculations of φ:

$$\varphi = \arcsin\left(\frac{I_2 - I_1}{2(I_2 + I_1)}\right) \approx \frac{I_2 - I_1}{2(I_2 + I_1)}. \tag{3.20}$$

Although the schematic shows normal incidence of the probe laser into the Rb cell, we introduce a slight ($\leq 5°$) angle to minimize back-reflected interference fringes arising from the lack of a cell anti-reflection coating. Two methods of detection are possible using either photodetector- or camera-based detection to measure the electron beam magnetic field.

Photodetectors are inherently less noisy and more efficient at converting light into electrical signals. However, spatial information is lost as they integrate transmission over the entire cross-section of incident light. While this can be resolved by translating a narrow laser and reading out the NMOR as a function of laser position, it is more straightforward to use a camera to image the spatially-dependent NMOR, at the cost of increased electronic noise.

For a narrow laser beam the magnitude and sign of the rotation angle depend on the cumulative magnetic field along the optical propagation path. Therefore, the direction of polarization rotation should be dependent on the position of the electron beam relative to the probe laser shown in figure 3.13(a), with the resulting NMOR signal in figure 3.13(b). This NMOR reversal based on electron beam position can be used to verify the electron magnetic field behavior and coarsely align the electron beam to the laser.

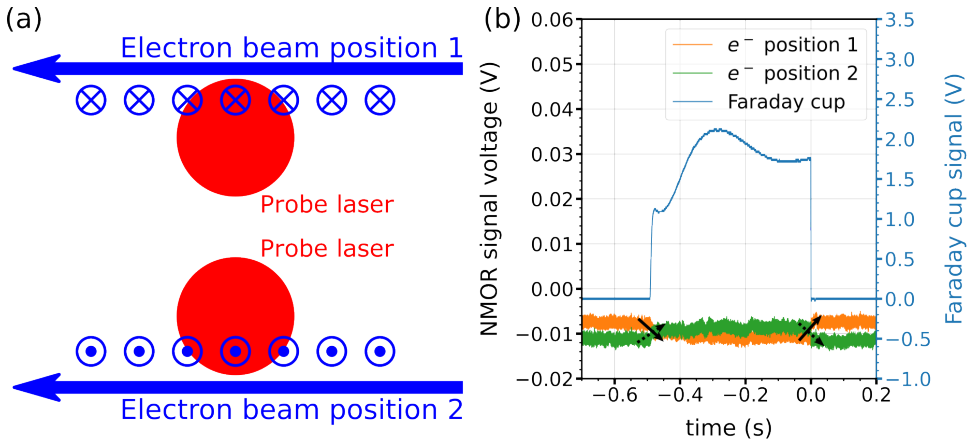


Figure 3.13: (a) Electron beam position change relative to the probe laser demonstrating the reversal of magnetic field direction across the laser cross-section. (b) Resulting NMOR based on two electron beam positions (orange and green, left axis) when the electron beam is turned on (blue, right axis). Due to the opposite directions of magnetic field between electron beam positions, opposite NMOR direction occurs, emphasized by the arrows for each plot.

To verify that the observed NMOR signal is due to the electron beam magnetic field, the reversal of polarization rotation demonstrated in figure 3.13(b) must be present. Further, this signal must invert when swapping I_1 and I_2 in equation 3.20, accomplished by rotating the polarimeter balancing waveplate by 45° (equivalent to rotation of the polar-

ization by 90°). This verification factors out irrelevant changes in laser absorption due to stray electrons sputtering rubidium metal into the surrounding rubidium vapor, increasing laser absorption, which is independent of electron beam position or polarimeter balancing.

A 2D map of the polarization angle can be imaged on a camera using a laser beam with large cross-section to obtain a transverse profile of the e-beam. For camera-based NMOR, we measure total power changes in each channel that let us measure the integrated rotation signal, which is convenient for system alignment. For most presented data we use a CCD-based imaging system (magnification 0.50) to record the spatial distribution $\varphi(y, z)$ across the laser beam. To ensure the consistency between the recorded intensity masks $I_{1,2}$ they are recorded consecutively at the same camera position, but with a different polarimeter balancing angle before the polarizer. An example of such intensity profile for one of the channels is shown in figure 3.12(b), in which the intensity difference between two channels, induced by the e-beam, is not distinguishable by the naked eye. As the laser beam has a Gaussian intensity profile, we only use its central part with sufficient intensity for determining the polarization rotation angle.

In addition, the electron beam was pulsed on and off at 1 Hz to record two consecutive images, with and without the e-beam. To synchronize the camera and electron beam pulsing, both are controlled using square waveforms with a relative 50° phase to ensure the camera triggers after the initial electron focusing transient in figure 3.9(a). Figure 3.14 shows the camera exposure time relative to the Faraday cup current read when the electron beam turns on. The phase between the electron and camera trigger signals should be sufficient enough to trigger the camera after the electron beam transient, but small enough to ensure the camera does not expose during the electron pulse transition.

Subtracting the pairs of images from each other allows us to remove any residual polarization rotation due to stray magnetic fields or optical elements to ensure that we only detect the polarization rotation caused by the e-beam. A number of averages can also be designated to reduce optical or electron related noises over the course of data acquisition. Since we measure small changes in polarization angle, on the order of 1 mrad,

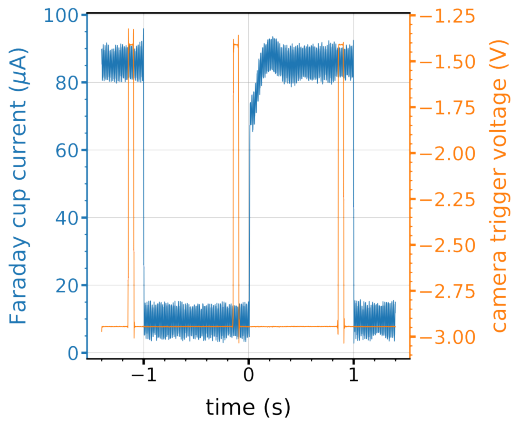


Figure 3.14: Camera triggering relative to the pulsing of the electron beam. The trigger signal is set so that the camera exposure (orange) activates after the electron beam transients measured in the Faraday cup (blue) stabilize to consistently capture a constant beam profile. The width of the camera trigger pulse is the exposure time (50 ms, in this demonstration).

we require sufficient camera bit depth to differentiate small pixel count resolution. Each image holds up to 2592x1944 pixels each measuring 12 *bits* per pixel (1.5 *bytes* per pixel), which corresponds to a total of $\sim$ 7.5 MB per image per second (assuming 1 Hz camera triggering). The consequence of large data transfer from the camera will result in dropped frames, despite using Ethernet interfaces with bandwidths up to 1 GB/s. This manifests as a skip in the image pairs acquired during data collection, misidentifying the electron state for subsequent images. The concept and solution of dropped frames in shown in figure 3.15, where frame 4 is dropped. As a result, the subsequent frames are reversed in pairwise order, such that when the subtraction and averaging is done, the resulting rotation would be significantly smaller than the true polarization rotation. We can monitor which frames are dropped by monitoring the timestamps of each frame and tracking the period between frames. Since the acquisition continues until the designated averaging number is reached, the imaging collection will acquire an additional frame (9, in figure 3.15). By removing the frame with period longer than the camera trigger period T and the final frame in the dataset, correct frame ordering is reestablished, and the pairwise subtraction and averaging will measure the proper NMOR angle due to the electron beam magnetic field. Should multiple frames be dropped, the procedure can be repeated, removing the

frame with long period and the final frame to maintain frame ordering for an arbitrary number of dropped frames. Traditionally, this correction is manually executed, given that the rate of dropped frames is small enough to feasibly make the corrections. However, for large numbers of dropped frames, future data acquisition improvements should be done to automate the frame correction procedure.

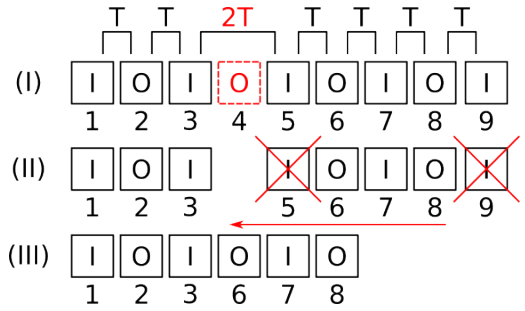


Figure 3.15: Dropped frame demonstration and correction procedure to ensure proper pairwise subtraction. (I) Frames are acquired every T seconds alternating between electrons ON I and OFF O, except for frame 4, which never arrives despite the camera and electron beam successfully triggering, resulting in an additional frame 9 at the end of the data acquisition. (II) Removing the frame with period $2T$ and the final frame (frames 5 and 9) resets the ordering of electron pulsing to follow correct ordering shown in (III).

By capturing the intensity profiles of the two outputs on a CCD camera with two waveplate positions, we were able to calculate local variations of $\varphi(y, z)$ within the laser beam cross-section as shown in Fig. 3.12(c). The angle distribution within the laser beam is extracted by applying equation 3.20 to each camera pixel. Since the e-beam generates a circulating magnetic field in the $x - y$ plane, and the nonlinear polarization rotation is primarily sensitive to the x-component of the magnetic field, we expect to see a sign change in the measured polarization rotation angle below and above the center of the e-beam, as shown in Fig. 3.4.

To reconstruct the electron beam profile according to section 3.3, we need to normalize the electron-induced polarization rotation to isolate the electron beam current. In equation 3.16, we measure $\beta(y, z)$ by normalizing the uniform NMOR to the induced magnetic field. Figure 3.16(a) shows the dependence of the uniform magnetic field on the voltage applied in the coil using a calibrated F.W. Bell Model 9500 gaussmeter. Since it is not possible

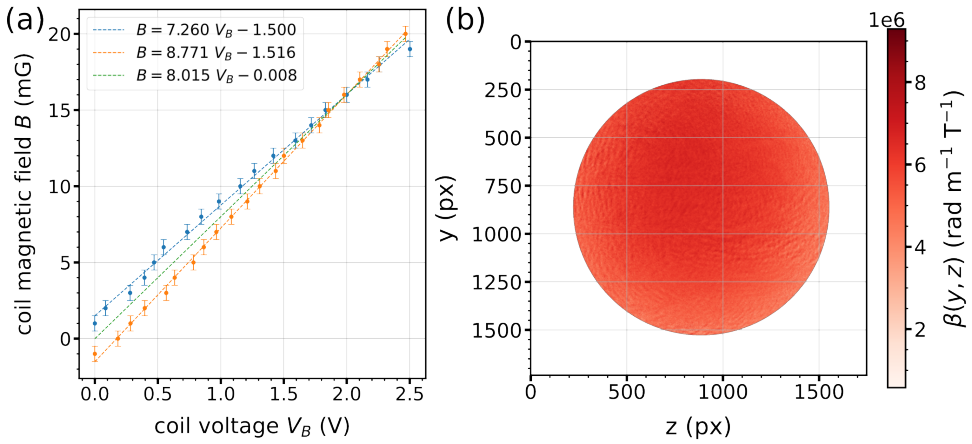


Figure 3.16: (a) uniform magnetic field coil calibration to voltage driving the coils. Calibrations were taken on each side of the cell (blue, orange) with the average of the calibration corresponding to the field inside of the cell (green). (b) $\beta(y, z)$ calibration used to normalize out the light-matter variation from the NMOR images in figure 3.12(c).

to monitor the magnetic field inside the Rb cell using the gaussmeter probe, we take the average calibration between the fields measured on either side of the cell (± 5 mm). This way, we can record $\beta(y, z)$ in the exact same manner as electron-induced NMOR, instead pulsing the uniform magnetic field, and by using the voltage across the coils, we can calculate the spatial profile of $\beta(y, z)$ through equation 3.16 shown in figure 3.16(b).

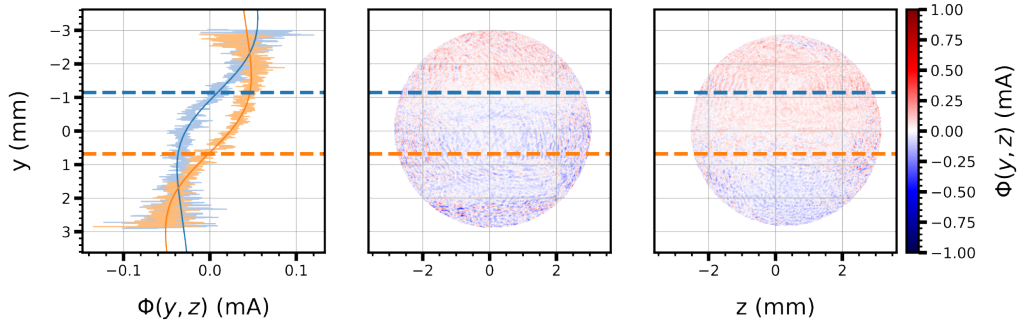


Figure 3.17: Measured normalized rotation images $\Phi(y, z)$ for two different electron beam positions of electron beam emission current $\mathcal{I}_E = 200\mu$A and energy $E = 20$ keV. The location of the e-beam center in each case is clearly detectable by the reversal of the polarization rotation direction (red versus blue). The left panel shows the vertical profiles of the images with the corresponding fits from equation 3.17, and the horizontal dashed lines indicate the positions of the electron beam center, also extracted from the fits.

Fig. 3.17 shows the examples of the recorded normalized signal $\Phi(y, z)$ for two vertical

positions of the e-beam. As expected, the polarization rotation changes direction from positive to negative at the e-beam center position, and the signal is uniform in the z-direction.

3.5 Electron Beam Parameter Verification

To verify the measured quantities obtained via the previous discussion, we correlate beam position, current, and width with secondary beam diagnostics discussed in section 3.4.2. Figure 3.18 shows the correlations between beam position and current, when compared to electron-induced impact fluorescence and the Faraday cup (and electron source current), respectively. We verify the accuracy of the beam position measurements by capturing images of fluorescence from Rb atoms ionized by the e-beam (discussed in section 3.4.2). The measured centroid position variation matches within 16% between the two methods, indicating that the spatial coordinate systems agree between the two separate imaging systems and that we accurately measure beam position betweeo the two methods. Similarly, we compare the total e-beam current value extracted from the polarization rotation measurements with that measured at the Faraday cup $\mathcal{I}_{\mathrm{FC}}$ and electron emission current $\mathcal{I}_{\mathrm{E}}$. Since the system lacks a secondary current diagnostic in the region of the magnetometer, we can only validate the current within the range set by the Faraday cup, located approximately 25 cm downstream of the Rb cell, and the electron source, approximately 75 cm upstream of the detection region. The current measured by the magnetometer matches within 36% of $\mathcal{I}_{\mathrm{FC}}$ and 14% of $\mathcal{I}_{\mathrm{E}}$ between the two methods.

From the fit, we obtain a FWHM e-beam diameter of 1.96 ± 0.13 mm. Although we are unable to independently verify the precise profiles of the electron beam, this value is noticeably broader than that obtained from the fluorescence fits, 0.89 ± 0.04 mm FWHM, where the uncertainty for these quantities are derived by considering the variance of the profile parameters of the datasets. In the next section, we discuss the lower bound of magnetic field and beam current measurements of the initial electron beam profiler and

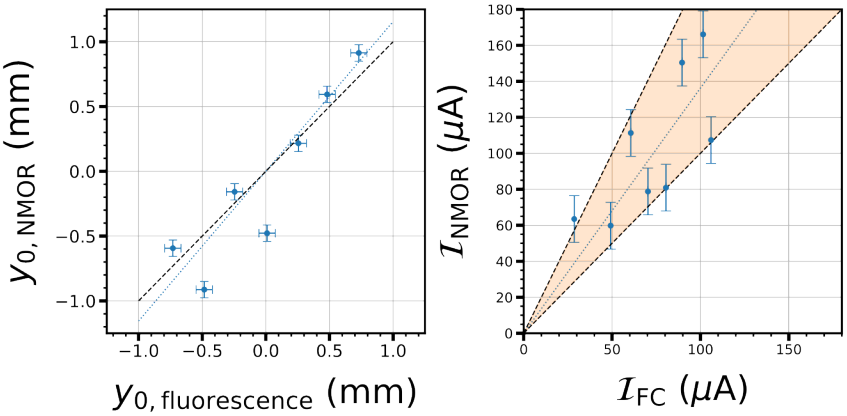


Figure 3.18: (a) Comparison between the electron beam center position extracted from the polarization rotation measurement $y_{0,\mathrm{NMOR}}$ and from the electron-induced rubidium fluorescence images $y_{0,\mathrm{fluorescence}}$ with a regression of $y_{0,\mathrm{NMOR}} = (1.16{\pm}0.21)\, y_{0,\mathrm{fluorescence}}$ (dotted blue line). (b) Comparison between the total electron beam current determined using the polarization rotation fits $\mathcal{I}_{\mathrm{NMOR}}$ and measured directly using the Faraday cup $\mathcal{I}_{\mathrm{FC}}$ with a regression of $\mathcal{I}_{\mathrm{NMOR}} = (1.36 \pm 0.13)\, \mathcal{I}_{\mathrm{FC}}$ (dotted blue line). The black dashed lines have a slope of 1 and 2, representing $\mathcal{I}_{\mathrm{FC}}$ and the emission current $\mathcal{I}_{\mathrm{E}} \approx 2\mathcal{I}_{\mathrm{FC}}$. The shaded region indicates the range of valid beam currents measurable by NMOR. Uncertainties in NMOR-derived parameters stem from the variance of electron beam center position and total current under identical experimental conditions. The fluorescence uncertainty is based on the variance in center position for varied beam currents, while the Faraday cup signal uncertainty is due to the variance of the measured Faraday cup signal (read on an oscilloscope).

primary sources of this width discrepancy, with potential solutions for each source.

3.5.1 Beam Current Measurement Sensitivity and Beam Width Discrepancy

Here we estimate the optimal performance of the proposed sensor, where the performance is severely affected by the technical noises in the optical detection. As the dark noise of the CCD camera, used here, is higher than for a balanced photo-diode detector (BPD), we consider the latter to estimate the best achievable sensitivity. The smallest measurable e-beam current (δI_e) is estimated to correspond to the signal-to-noise ratio (SNR) equal to one. In our case, it is determined by the smallest measurable polarization rotation angle ($\delta\varphi$) and by the response of our system S, i.e. the polarization rotation angle per current carried by the e-beam:

$$\delta I_e = \left(\frac{d\varphi}{dI_e}\right)^{-1} \delta\varphi = \frac{1}{S}\delta\varphi \tag{3.21}$$

To estimate the response S of the system, we varied the emission current of our electron gun in the range of 0 - 90 μA. We observe the linear relationship between the measured rotation angle and the emission current with a slope $S = 0.21$ mrad/μA. (We note that the emission current is consistently 50% larger than the current indicated by the Faraday cup due to the losses along the electron beam propagation path, such as beam line obstacles, back-scattered electrons, etc.).

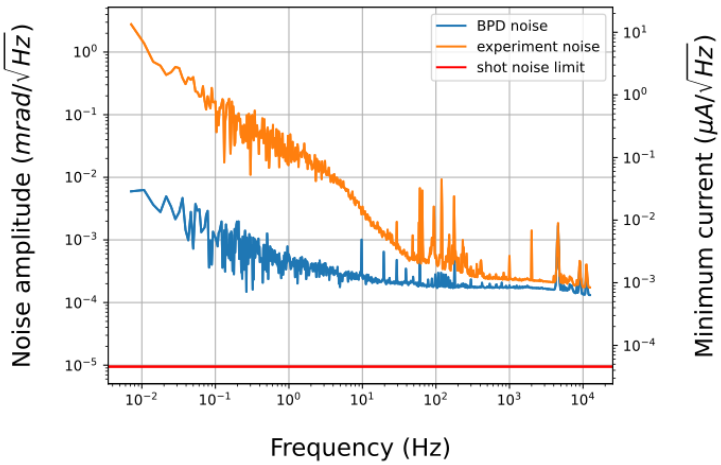


Figure 3.19: Fourier transformed signals from the BPD in the absence of polarization rotation. Plotted are the cases of typical experimental conditions (experiment noise, orange) compared to the dark noise of the BPD (BPD noise, blue). The red line in the bottom shows the shot-noise limited sensitivity. The right axis defines the minimum detectable current, based on the minimum detectable rotation angle of the left axis.

The smallest measured rotation angle (per unit of bandwidth) is fundamentally set by the shot noise of the laser beam, discussed in detail in chapter 4, which depends on the laser power P [89] as

$$\delta\varphi = \sqrt{\frac{2hc/\lambda}{\eta P}} = \sqrt{\frac{2e}{I_{ph}}}, \tag{3.22}$$

where h is the Planck constant; c is the speed of light; λ is the laser probe wavelength, η is the quantum efficiency of the detector, e is charge of the electron and I_{ph} is total

photo-current generated in the BPD. It is easy to see that the expression under the square root is just the number of photo-electrons generated by light in the photodiode, per unit of time.

Combining equations 3.21 and 3.22, we calculated shot noise-limited sensitivity for our setup to be 400 pA/$\sqrt{\text{Hz}}$ (see Fig. 3.19). In practice, the sensitivity limit is actually set by the classical noise sources: residual light intensity noise, mechanical vibrations, flicker noise in electronics, that make it hard to reach the shot noise limited performance. In our case, the performance of the BPD was limited by the photodiode dark noise at high frequencies to about 1 nA/$\sqrt{\text{Hz}}$ (see Fig. 3.19). At lower frequencies, we see performance degradation with a characteristic $1/f$ noise.

While there may be a variety of reasons behind the beam width discrepancy, we primarily attribute poor signal-to-noise ratio (SNR) of the rotation signal, especially at the edges of the laser beam, where the laser intensity is low. The overall rotation signal was typically below 1 mrad, and thus strongly affected by the camera electronic noise.

Additionally, the presence of a transverse magnetic field B_y in figure 3.4 has been shown to broaden the NMOR resonance [90], and thus the unaccounted transverse components of the magnetic field can increase the estimated width of the electron beam. However, due to the antisymmetric electron beam magnetic field, these transverse magnetic field contributions could cancel out through the integration along the laser propagation length. To settle this, realistic modelling of the NMOR response to the full electron beam magnetic field needs to be simulated to confirm whether or not these transverse fields broaden the electron beam profile.

There are a few straightforward steps for improving the experimental sensitivity. From Fig. 3.19 it is clear that increasing the detection frequency can reduce the noise dramatically. In the current experiment, the data was recorded at 1 Hz rate due to the limited speed of the electron beam modulator, but in practice many charged particle beams are pulsed at a much faster rate. Although this detection scheme is limited by the speed of the atomic response through the EIT lifetime Γ_{EIT}^{-1} [38] in equation 3.11, using a different, off-

resonant two-photon Raman scheme could achieve sub-ns response [91]. Moreover, some laser-related noises can be suppressed by monitoring a reference probe beam unaffected by the charged particles. Subtracting such a reference from the signal laser beam can help to eliminate the background signals not pertaining to the electron beam.

These enhancements can improve the performance of the proposed tracker, resulting in a wider range of charged particle beams that can be profiled for various nuclear experiments. In the next chapter, we discuss a fundamental improvement to the system to address the fundamental optical noise and handle the poor SNR of the initial electron beam profiler.

Chapter 4

Quantum-Enhancement Via Four-Wave Mixing

Direct measurement of polarization rotation is prone to both environmental and optical noise, reducing achievable magnetic field sensitivity and placing a lower bound on the electron beam currents that can be measured. One way to reduce the noise contributions is the use of another optical field to act as a reference for the magnetic field environment, such that the electron beam signal is obtained from a differential measurement of the signal and reference fields. While the environmental fluctuations are limited through differential measurements, there is still a noise contribution rooted in the quantum nature of the photons interacting with the atomic medium. Any differential optical scheme, whether through a gradiometer or differential polarimeter configuration, is subject to the probabilistic nature of light, resulting in fluctuations in the laser light intensity and phase. This photon noise limit is ultimately determined by the Heisenberg uncertainty principle [92] given by

$$\langle \Delta \hat{N}^2 \rangle \langle \Delta \hat{\phi}^2 \rangle \geq \frac{1}{4}, \tag{4.1}$$

where $\Delta \hat{N}^2$ is the photon number (i.e. intensity) fluctuations and $\Delta \hat{\phi}$ the photon phase fluctuations. However, the *product* of the fluctuations, or quadratures, need only be greater

(or equal) to 1/4, allowing the reduction (or squeezing) of one quadrature at the expense of the other.

This concept of squeezed light has been used for various precision measurements and sensing applications due to the reduced fluctuations in light amplitude or phase [93–95]. Non-classical light has been used in sensing applications to detect magnetic fields [45, 49, 96] and gravitational waves [97, 98] that are not possible with coherent light. Spatial characterization of squeezed light has also been captured through quantum imaging [99], utilizing entangled sources of light to identify the intensity or phase correlations in each optical field [100–102], or imaging squeezed vacuum for low-light or photosensitive applications [103–105].

To squeeze the uncertainty of the differential intensity measurement and reduce optical noise present in the electron beam detector, we use four-wave mixing to generate two-mode squeezed light utilizing two optical fields for quantum-enhanced noise suppression. Four-wave mixing (FWM) has been thoroughly explored theoretically [55, 106] and experimentally [107–110] as a method of generating two-mode squeezing. Depending on the configuration, the output from FWM can be used for effective polarization entanglement using polarization-selective FWM [111] or as a source of entangled photon pairs for quantum communications [112–114]. The reduced optical noise provided by FWM has been used for quantum-enhanced sensing for two-photon spectroscopy [115, 116], magnetic field sensing [50], and it is expected that Rydberg atom-based sensing could benefit from multi-wave mixing to sense electric fields [117, 118].

For the remainder of the dissertation, we characterize and suppress this quantum noise using entangled, far-detuned optical probe fields through a combination of four-wave mixing and far-detuned NMOR to achieve quantum-enhanced magnetometer sensitivity.

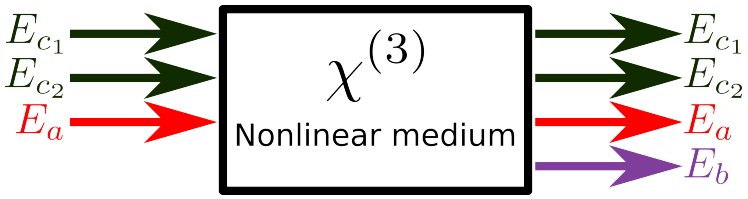


Figure 4.1: Input and output scheme for the four-wave mixing process. Two powerful pump fields E_{c_1} and E_{c_2} and a weak probe field E_a interact within a general third-order nonlinear medium to generate four output optical fields, including a new conjugate field E_b.

4.1 Four-Wave Mixing Theory

The fundamental scheme of four-wave mixing is demonstrated in Figure 4.1 where a high-intensity pump laser $E_{c_{1,2}}$ intersects with a weakly intense probe laser E_a within the rubidium vapor medium. Due to the high intensity of the pump field, the polarization of the atomic medium is no longer linear as defined in equation 2.8, and higher order terms begin contributing to the polarization response of the medium:

$$\boldsymbol{P} = \epsilon_0 \sum_n \chi^{(n)} \boldsymbol{E}^n. \tag{4.2}$$

The second-order nonlinearity $\chi^{(2)}$ is often observed in anisotropic nonlinear crystals $(n = 2)$ [119], whereas the third-order susceptibility $\chi^{(3)}$ is seen in atomic vapors [120]. In FWM, we consider the effect of two strong pump fields propagating with a weak probe field, leading to the generation of a fourth conjugate field. To show this, the third-order polarization of the atomic medium is evaluated:

$$P^{(3)} = \epsilon_0 \chi^{(3)} (\boldsymbol{E}_a + \boldsymbol{E}_{c_1} + \boldsymbol{E}_{c_2})^3 \tag{4.3}$$

We define the pump $\boldsymbol{E}_{c_{1,2}}$, probe $\boldsymbol{E}_a$, and conjugate $\boldsymbol{E}_b$ fields through equation 2.3. When we write out the cube of the electric fields, the result has many terms, reducible by limiting to the phase matched terms of order $\exp(i\boldsymbol{k}_j \cdot \boldsymbol{r})$ $(j = a, b, c)$ [121]. In this case

the dominant contributions to polarization then become

$$P_b^{(3)} = \epsilon_0 \chi_b^{(3)} E_a^* E_{c_1} E_{c_2} \exp\left[i(\boldsymbol{k}_a - \boldsymbol{k}_{c_1} - \boldsymbol{k}_{c_2})z - (\omega_a - \omega_{c_1} - \omega_{c_2})t\right] \tag{4.4}$$

$$P_a^{(3)} = \epsilon_0 \chi_a^{(3)} E_b^* E_{c_1} E_{c_2} \exp\left[i(\boldsymbol{k}_b - \boldsymbol{k}_{c_1} - \boldsymbol{k}_{c_2})z - (\omega_b - \omega_{c_1} - \omega_{c_2})t\right], \tag{4.5}$$

where the conjugate polarization results from the phase conjugation of the probe. For the conjugate component of the polarization $P_b^{(3)}$, the dependence on the pump and probe frequencies and wave vectors vanishes if $\omega_b = \omega_a - \omega_{c_1} - \omega_{c_2}$ and $\boldsymbol{k}_b = \boldsymbol{k}_a - \boldsymbol{k}_{c_1} - \boldsymbol{k}_{c_2}$. For the probe component of the polarization $P_a^{(3)}$, the dependence on the pump and probe frequencies and wave vectors vanishes if $\omega_a = \omega_b - \omega_{c_1} - \omega_{c_2}$ and $\boldsymbol{k}_a = \boldsymbol{k}_b - \boldsymbol{k}_{c_1} - \boldsymbol{k}_{c_2}$. In order for energy to be conserved through the energy level diagram in figure 4.3(b), we require that $\omega_a + \omega_a = \omega_{c_1} + \omega_{c_2}$.

The wave numbers, however, are dependent on these frequencies in a polarized medium, where $|\boldsymbol{k}_j| = n_j(\omega)\omega_j/c$. Therefore, the dispersion of the medium means that for $\boldsymbol{k}_j \cdot \hat{z} = |\boldsymbol{k}_j| \cos\theta$, then $\theta \neq 0$ depending on the various frequencies of the optical fields constrained by

$$\frac{n_{c_1}\omega_{c_1}}{c}\cos\theta_{c_1} + \frac{n_{c_2}\omega_{c_2}}{c}\cos\theta_{c_2} + \frac{n_a\omega_a}{c}\cos\theta_a = \frac{n_b\omega_b}{c}\cos\theta_b. \tag{4.6}$$

This use of dispersion allows separation between pump, probe, and conjugate fields shown in figure 4.2 in order to isolate and individually steer the selected fields within the experiment at the cost of sensitive intersection angle dependency.

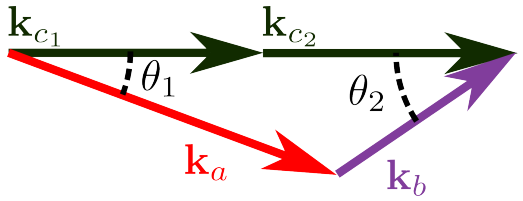


Figure 4.2: Light vector diagram showing momentum conservation in the case of nonzero angles $\theta_1 = \theta_{c_1} - \theta_a$ and $\theta_2 = \theta_{c_2} - \theta_b$, allowing separation of pump, probe, and conjugate fields dependent on the relative frequencies of the pump and probe fields.

Thus we show that sending strong pump fields accesses the $\chi^{(3)}$ nonlinear susceptibility, and by adhering to energy and momentum conservation, we generate a new conjugate field.

4.1.1 Four-wave mixing in Rb vapor double-Λ systems

Next, we consider the noise characteristics of the input and output fields using a quantum formalism to describe the light-matter interaction through creation and annihilation operators of the two fields. To start describing the effects of four-wave mixing on transmission and fluctuations of the involved fields, we adopt the quantum operator approach for the modes of the pump, probe, and conjugate fields. Review of fundamental quantum treatment of photon creation and annihilation operators is given in appendix A, whereas here we assume knowledge of commutation relations, coherent states, and eigenvalues of creation and annihilation operators.

The process of four-wave mixing is described by Figure 4.3.

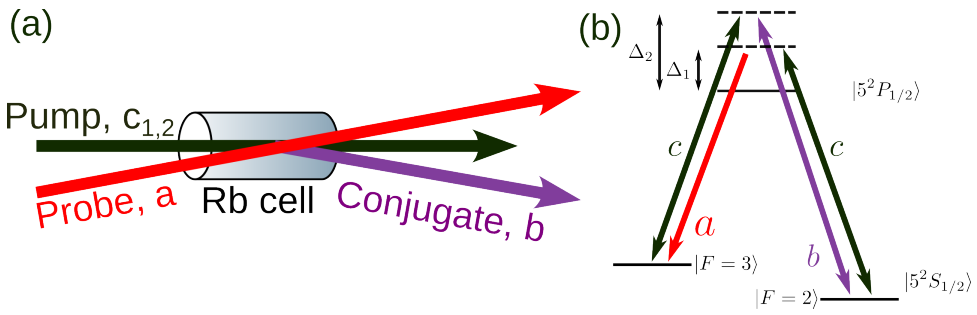


Figure 4.3: (a) Mechanism of four-wave mixing. A powerful pump field c and weak probe field a intersect within the Rb cell, and generate a new conjugate field b through the third order nonlinear susceptibility of the medium and phase matching between the pump and probe fields. The input mode for the conjugate field is the vacuum state, while the input states for probe and pump fields are coherent states. (b) Double-Λ interaction scheme for FWM for the D_1 transition of Rb ($\lambda = 795$ nm).

During this process, a pump photon is absorbed to stimulate emission of a probe photon, then another pump photon is absorbed followed by the stimulated emission of a conjugate photon. In this case, the same pump field is absorbed $c_1 = c_2 = c$ and the Hamiltonian for this process is given by

$$H = i\hbar\beta b^\dagger c a^\dagger c - i\hbar\beta^* b c^\dagger a c^\dagger, \tag{4.7}$$

where $\hbar$ is the reduced Planck constant, β is a constant associated with the light-atom coupling, and a,b,c are the annihilation operators for the probe, conjugate, and pump fields, respectively, with corresponding creation operators $a^\dagger$,$b^\dagger$,$c^\dagger$. It is immediately seen that the imaginary factor i keeps the Hamiltonian hermitian. If the pump field is in a coherent state $|\gamma\rangle$ where $\gamma \gg 1$, with $c|\gamma\rangle \approx \gamma|\gamma\rangle$ (where absorbing one photon from an intense pump field will leave the pump field intensity unchanged), then we can rewrite the Hamiltonian solely in terms of probe and conjugate operators

$$H = i\hbar\xi b^\dagger a^\dagger + H.C., \tag{4.8}$$

where $H.C.$ is the hermitian conjugate of the first term, and the rescaled light-atom coupling ξ is

$$\xi = \beta\gamma^2, \tag{4.9}$$

where γ^2 is the pump intensity, and β can be tuned dependent on probe power, pump and probe detuning, and atomic density (i.e. cell temperature).

To derive the input output relations for the four-wave mixing process, we use the propagation equations for the probe and conjugate operators in the Heisenberg picture:

$$\frac{da}{dz} = \frac{i}{\hbar}[H, a] \qquad \frac{db}{dz} = \frac{i}{\hbar}[H, b] \tag{4.10}$$

Plugging in the Hamiltonian in equation 4.8 and solving the coupled differential equations yields the input-output operators over an interaction length L [122]:

$$\begin{pmatrix} a_{out} \\ b^\dagger_{out} \end{pmatrix} = \begin{pmatrix} \cosh(\xi L) & \sinh(\xi L) \\ \sinh(\xi L) & \cosh(\xi L) \end{pmatrix} \begin{pmatrix} a \\ b^\dagger \end{pmatrix} \tag{4.11}$$

To calculate the fluctuations in each field intensity and the differential intensity we calculate the expectation value of each fields' number operator, $\langle N_{a_{out}}\rangle$, $\langle N_{b_{out}}\rangle$, $\langle N_{a_{out}} +$

$N_{b_{out}}\rangle$, and $\langle N_{a_{out}} - N_{b_{out}}\rangle$ and the expectation values of their squares $\langle N_{a_{out}}^2\rangle$, $\langle N_{b_{out}}^2\rangle$, $\langle (N_{a_{out}} + N_{b_{out}})^2\rangle$, and $(\langle N_{a_{out}} - N_{b_{out}})^2\rangle$ to evaluate all the variances.

Throughout these calculations we note that (1) the initial state for the conjugate mode is vacuum, so $\langle N_b\rangle = \langle b^\dagger b\rangle = \langle b^\dagger\rangle = \langle b\rangle = 0$, and (2) there are many photons in the incident probe field $\langle N_a\rangle = \langle a^\dagger a\rangle \gg 1$. Taking these into account, we can calculate the four expectation values:

$$\langle N_{a_{out}}\rangle \approx G^2\langle a^\dagger a\rangle, \tag{4.12}$$

$$\langle N_{b_{out}}\rangle \approx (G^2 - 1)\langle a^\dagger a\rangle, \tag{4.13}$$

$$\langle N_{a_{out}} - N_{b_{out}}\rangle \approx \langle a^\dagger a\rangle, \tag{4.14}$$

$$\langle N_{a_{out}} + N_{b_{out}}\rangle \approx (2G^2 - 1)\langle a^\dagger a\rangle, \tag{4.15}$$

where we have defined the gain, $G^2 = \cosh^2(\xi L)$. Equation 4.14 shows that the difference in output photon number (between probe and conjugate states) is the input probe photon number, which can be used to identify optical losses in the experiment.

4.1.2 Noise Characteristics of FWM Fields

To calculate and compare the field fluctuations of the output of the four-wave mixing process, we need to calculate

$$\langle (\Delta n)_{a_{out}}^2\rangle = \langle n_{a_{out}}^2\rangle - \langle n_{a_{out}}\rangle^2, \tag{4.16}$$

with respect to the coherent input states.

We next compare the uncertainties of the individual optical fields coming from the FWM process, using equation 4.11. Writing $G = \cosh(\xi L)$ and $g = \sinh(\xi L)$ to simplify the expressions, then the output relations are given by

$$a_{out} = Ga + gb^\dagger \tag{4.17}$$

$$b^\dagger_{out} = ga + Gb^\dagger \tag{4.18}$$

Next, we evaluate the probe output uncertainty including the cumbersome $\langle n^2_{a_{out}} \rangle$ term:

$$\begin{aligned}\langle n^2_{a_{out}} \rangle = \langle & G^4 a^\dagger a a^\dagger a + G^3 g a^\dagger a a^\dagger b^\dagger + G^3 g a^\dagger a b a \\ & + G^2 g^2 a^\dagger a b b^\dagger + G^3 g a^\dagger b^\dagger a^\dagger a + G^2 g^2 a^\dagger b^\dagger a^\dagger b^\dagger \\ & + G^2 g^2 a^\dagger b^\dagger b a + G g^3 a^\dagger b^\dagger b b^\dagger + G^3 g b a a^\dagger a \\ & + G^2 g^2 b a a^\dagger b^\dagger + G^2 g^2 b a b a + G g^3 b a b b^\dagger \\ & + G^2 g^2 b b^\dagger a^\dagger a + G g^3 b b^\dagger a^\dagger b^\dagger + G g^3 b b^\dagger b a \\ & + g^4 b b^\dagger b b^\dagger \rangle \end{aligned} \tag{4.19}$$

However, many terms including conjugate operators disappear for the vacuum conjugate input state and number state orthogonality. Therefore, the terms including $bb^\dagger$, $bb^\dagger b^\dagger$ and any combination of a, $a^\dagger$ remain:

$$\langle n^2_{a_{out}} \rangle = \langle G^4 a^\dagger a a^\dagger a + 2G^2 g^2 a^\dagger a + G^2 g^2 a a^\dagger + g^4 \rangle \tag{4.20}$$

$$= G^4 |\alpha|^4 + G^4 |\alpha|^2 + 3G^2 g^2 |\alpha|^2 + g^2 G^2 + g^4, \tag{4.21}$$

for α the eigenvalue of the coherent state $a|\alpha\rangle = \alpha|\alpha\rangle$, where $|\alpha|^2$ corresponds to the intensity of the probe coherent state. Through a similar, albeit simpler evaluation, we can then evaluate the output probe intensity fluctuations

$$\langle n_{a_{out}}\rangle^2 = (\langle G^2 a^\dagger a\rangle + g^2)^2 = G^4|\alpha|^4 + 2G^2g^2|\alpha|^2 + g^4 \tag{4.22}$$

$$\langle (\Delta n)^2_{a_{out}}\rangle = G^4|\alpha|^2 + G^2g^2|\alpha|^2 + G^2g^2 \tag{4.23}$$

If we only consider terms proportional to the probe input intensity then

$$\langle (\Delta n)^2_{a_{out}}\rangle \approx G^2(G^2+g^2)\langle n_a\rangle, \tag{4.24}$$

and we find that the output intensity fluctuations from the FWM process scale as the *square* of the associated gains $(G^2)^2$. We can similarly calculate the intensity variance for the conjugate output from the FWM process using similar derivations and approximations

$$\langle (\Delta n)^2_{b_{out}}\rangle \approx g^2(g^2+G^2)\langle n_a\rangle \tag{4.25}$$

Comparing this to a linear gain medium demonstrates that the individual probe and conjugate fields greatly amplify the fluctuations, therefore the individual fields are useless in the context of reducing optical noise. However, by considering the joint difference in the photon measurements, we can derive an interesting consequence from FWM, and calculate $\langle (\Delta(n_{a_{out}} - n_{b_{out}}))^2\rangle$ through

$$\langle (\Delta(n_{a_{out}} - n_{b_{out}}))^2\rangle = \langle (n_{a_{out}} - n_{b_{out}})^2\rangle - \langle n_{a_{out}} - n_{b_{out}}\rangle^2. \tag{4.26}$$

The two terms are reducible through identical arguments as before, where

$$\langle n_{a_{out}} - n_{b_{out}}\rangle^2 = (G^4 - 2G^2g^2 + g^4)|\alpha|^4 \tag{4.27}$$

$$\begin{aligned}\langle (n_{a_{out}} - n_{b_{out}})^2\rangle = {} & G^4|\alpha|^2 + G^4|\alpha|^4 - 2G^2g^2|\alpha|^4 - 2G^2g^2|\alpha|^2 \\ & + g^4|\alpha|^2 + g^4|\alpha|^4 - G^2g^2\end{aligned} \tag{4.28}$$

$$\langle (\Delta(n_{a_{out}} - n_{b_{out}}))^2\rangle = (G^2-g^2)^2|\alpha|^2 - G^2g^2 \approx |\alpha|^2 = \langle n_a\rangle, \tag{4.29}$$

where we make use of the identity $G^2 - g^2 = \cosh^2(\xi L) - \sinh^2(\xi L) = 1$. If we take the difference between two coherent states with different mean photon numbers $a|\alpha\rangle = \alpha|\alpha\rangle$, $b|\beta\rangle = \beta|\beta\rangle$, then the uncertainty in the differential measurement can be calculated for coherent states:

$$\langle (n_a - n_b)^2 \rangle = |\alpha|^2 + |\alpha|^4 - 2|\alpha|^2|\beta|^2 + |\beta|^2 + |\beta|^4 \tag{4.30}$$

$$\langle n_a - n_b \rangle^2 = |\alpha|^4 - 2|\alpha|^2|\beta|^2 + |\beta|^4 \tag{4.31}$$

$$\langle (\Delta(n_a - n_b))^2 \rangle = |\alpha|^2 + |\beta|^2 = \langle n_a \rangle + \langle n_b \rangle \tag{4.32}$$

To compare to the outputs of the FWM process, we add an amplifying gain to each term proportional to the gain from the FWM process such that

$$\langle n_a \rangle \rightarrow G^2 \langle n_a \rangle \qquad \langle n_b \rangle \rightarrow g^2 \langle n_a \rangle, \tag{4.33}$$

and consider the ratio between the variances of the FWM outputs and the coherent (i.e. shot noise limited) outputs, then the squeezing is obtained

$$S = 10 \log_{10} \left[\frac{\langle (\Delta(n_{a_{out}} - n_{b_{out}}))^2 \rangle}{\langle (\Delta(n_a - n_b))^2 \rangle} \right] = 10 \log_{10} \left[\frac{1}{G^2 + g^2} \right], \tag{4.34}$$

where $\langle (\Delta(n_{a_{out}} - n_{b_{out}}))^2 \rangle$ is the differential noise for the outputs of the FWM process. Negative values of squeezing S indicates sub-shot noise limited measurements of relative intensity.

The first consequence of this result indicates the importance of the joint differential measurement of the probe and conjugate fields. Due to the amplification, the individual field noise increases dramatically compared to the coherent case shown by equations 4.24 and 4.25. However, due to the high correlations of probe and conjugate intensities, the conjugate intensity fluctuation will scale with with probe intensity fluctuations. Thanks to this noise correlation, the differential intensity noise is reduced below the classical shot

noise limit. The noise suppression, or squeezing provided by equation 4.34, is deeply dependent on ideal intensity cancellation, where any optical losses (including those induced by atomic absorption) will greatly amplify the noise of the differential intensity measurement. Lastly, the general trend is that the gain of the probe and conjugate fields will determine the amount of squeezing measured. Indeed, this will depend on actual experimental implementation with ideal phase and spatial mode matching between the pump and probe fields, however, the configurations that maximises the gain will generally maximize the intensity squeezing.

4.2 Four-Wave Mixing Squeezing Characterization

The scheme for the four-wave mixing setup to measure quantum-enhanced noise suppression is shown in figure 4.4.

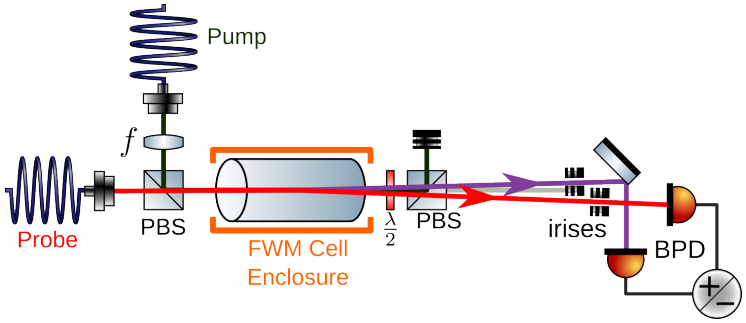


Figure 4.4: Experimental scheme to measure squeezing in the four-wave mixing cell. The pump is focused down using an $f = 1000$ mm lens to increase the pump intensity for FWM, which is filtered out using the second polarizing beam splitter (PBS) and irises. To measure relative intensity squeezing, the differential probe and conjugate transmission is measured with a custom-made balanced photo-detector (BPD)

The pump laser operates up to 500 mW power through the use of a Toptica BoosTA tapered laser amplifier, which is focused down to 1 mm within the FWM cell region through the use of a 1000 mm focal length lens to maximise the Rayleigh length and pump intensity within the squeezing cell. The probe laser has 55 μW of power, focused down to a similar size as the pump laser within the rubidium cell. The two lasers have a

relative frequency difference of $\Delta_{2p} = 3035$ MHz, and intersect with an angle of roughly 0.4° in the squeezing cell in order to satisfy the phase matching condition in equation 4.6. Stable FWM squeezing performance necessitates the use of frequency locking, which is accomplished using a Vescent offset phase lock servo to stabilize the frequency difference of the pump and probe lasers.

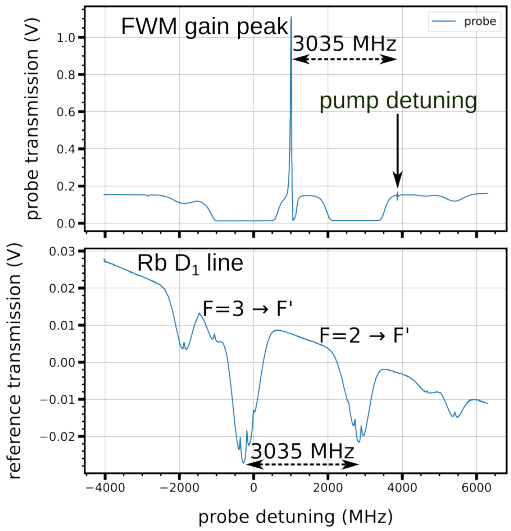


Figure 4.5: FWM frequency detunings relative to the rubidium spectra of the D_1 line operating around $\lambda = 795$ nm. The pump is initially tuned to the indicated detuning in order for the FWM gain peak to occur ≥ 1 GHz from the $F = 3 \rightarrow F'$ atomic transition, while the probe is ble-detuned $\Delta_{2p} = 3035$ MHz from the pump. Both lasers are tuned in this way to minimize optical losses due to atomic absorption.

The pump detuning is set such that both the generated probe and conjugate fields are more than 1 GHz away from the ^{85}Rb D_1 $F = 3$ transition to minimize the optical losses induced by atomic absorption processes as shown in figure 4.5. The frequency lock stabilizes the optical beat note in figure 4.6(b) generated by mixing the pump and probe fields through a fiber setup shown in figure 4.6(a).

The squeezing cell is made up of an isotopically pure ^{85}Rb vapor cell with antireflection coating to minimize optical losses in the resulting probe and conjugate beams. The squeezing cell enclosure is magnetically shielded, and its temperature is set to 105 °C using a Variac and temperature controller.

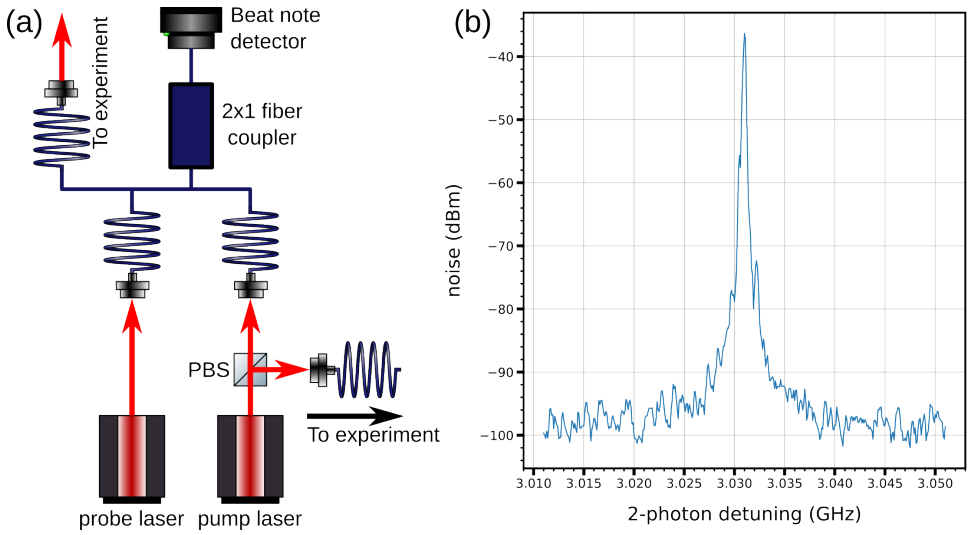


Figure 4.6: (a) Setup to lock the relative frequency difference between the input pump and probe lasers to $\Delta_{2p} = 3035$ MHz. (b) Example of the beat note generated between the pump and probe lasers within the phase detector. The actual measured peak occurs at half of the set frequency due to the output of the Vescent phase lock, so the frequency axis is doubled for demonstration.

Following the squeezing cell, the pump is filtered out through a PBS, a pair of irises, and pickoff mirrors in order to prevent any pump degradations to the noise suppression. Finally, the probe and conjugate are routed to a photodetector, capable of measuring the sum, difference, and individual channels reading the probe and conjugate transmissions.

The photodetector itself is customized for stable operation around 300 kHz, where the schematic and detailed discussion can be found in appendix C. The differential noise is measured using a HP-8596E spectrum analyzer connected through radio-frequency (RF) cabling.

The spectrum analyzer monitors the differential intensity noise spectral power $\langle(\Delta(n_a - n_b))^2\rangle^2$ by sweeping through the frequency spectrum, with the resolution of the frequency sweep set by the resolution bandwidth (RBW). To ensure proper spectrum analyzer bandwidth settings, we measure the frequency response of a sinusoidal signal, which results in a delta-function like signal in the frequency domain. RBW has the effect of integrating across frequency ranges set by the RBW, and higher bandwidths will result in more noise being integrated, as demonstrated in 4.7(a). The video bandwidth (VBW) on the

spectrum analyzer controls the refresh rate at which the data is read out, which has the effect of trace averaging depending on the frequency sweep time of the spectrum analyzer. Generally lower VBW corresponds to greater averaging at the cost of increased data acquisition time. Figure 4.7(b) shows the effect of VBW on the sinusoidal signal in the frequency domain, where lower VBW reduces variance in the traces outside the peak response. In our configuration, 300 Hz resolution bandwidth (RBW) and 30 Hz video bandwidth (VBW) were chosen such that the resulting signal peaks closely resemble a delta function.

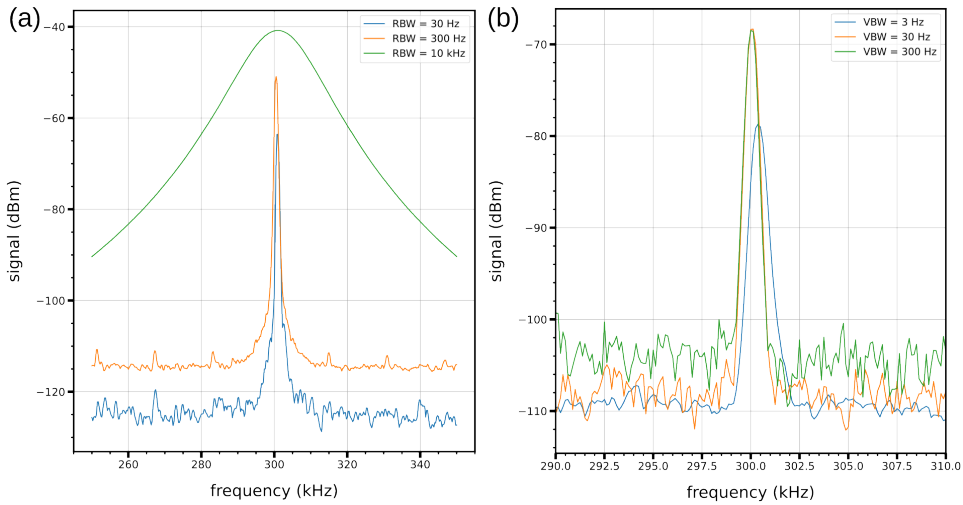


Figure 4.7: effect of varied (a) resolution bandwidth (with VBW = 10 Hz) and (b) video bandwidth (with RBW = 300 Hz) on a 300kHz sinusoidal signal on the spectrum analyzer. The resulting noise trace should behave like a delta function at 300 kHz, while peaks outside of 300 kHz are parasitic harmonics from lower frequency oscillations picked up by the spectrum analyzer.

4.2.1 Shot Noise Calibration

The squeezing derived in equation 4.34 is measured relative to shot noise, which is dependent on the transmission of the probe evident by equation 4.32. To experimentally determine this dependence, we measure the differential noise due to a balanced detection scheme shown in figure 4.8(a), where the probe laser is split equally in the polarizing beam splitter to cancel out all classical noise. The remaining noise is the optical shot noise

$\langle(\Delta n_a)^2\rangle$, which scales linearly with the probe power from equation 4.32 (for $|\alpha|^2 \to |\alpha|^2/2$ and $|\beta|^2 \to |\alpha|^2/2$). The dependence of the differential noise on the photovoltage measured on a *single* photodetector in the detection setup is shown in figure 4.8(b) with both logarithmic and linear scales.

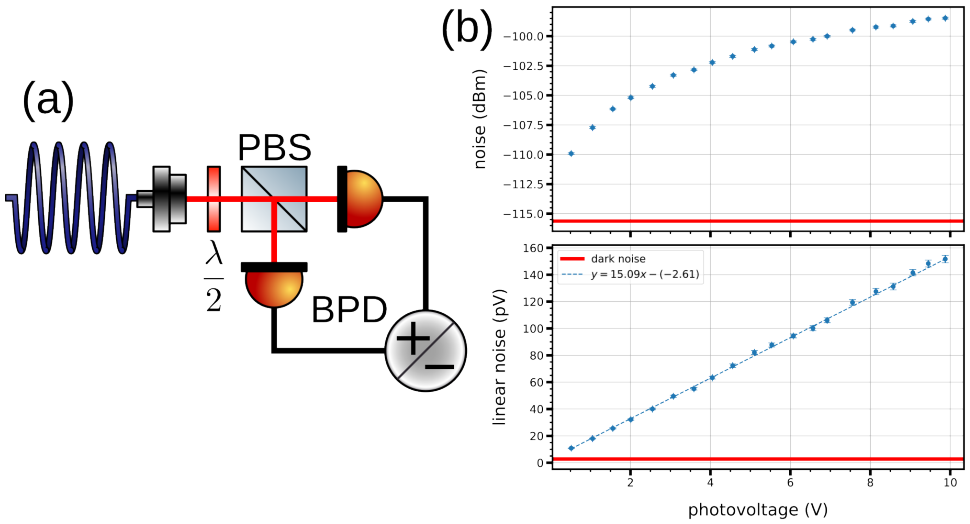


Figure 4.8: (a) Balanced differential detection scheme to measure differential noise as a function of probe laser power. (b) the resulting logarithmic and linear noise as a function of laser power. Fitting the linear noise provides a calibration mapping the measured photovoltage to the expected shot noise, allowing immediate evaluation of the squeezing for each measurement.

A simple linear fit results in the shot noise calibration for a given photovoltage V_{PD}

$$\Delta V_{SNL} = 15.09 V_{PD} + 2.61[pV], \tag{4.35}$$

for ΔV_{SNL} the shot noise, and 2.61 the offset due to the dark noise of the BPD. With this calibration, any noise can be measured relative to shot noise. The dark noise of the photodetector $\Delta V_{DN} = -115.62$dBm is obtained by measuring the resulting noise at 300kHz when both photodetectors are blocked. The squeezing is then calculated by taking into account the dark noise ΔV_{DN} and shot noise ΔV_{SNL} through

$$S = 10\log_{10}\left(10^{\frac{\Delta V}{10}} - 10^{\frac{\Delta V_{DN}}{10}}\right) - 10\log_{10}\left(10^{\frac{\Delta V_{SNL}}{10}} - 10^{\frac{\Delta V_{DN}}{10}}\right), \tag{4.36}$$

for arbitrarily measured differential noise ΔV from the spectrum analyzer.

4.2.2 Squeezing Optimization

Equation 4.34 shows that the squeezing is proportional to the gain $G(\xi L) = G(\beta\gamma^2 L)$ such that the atomic coupling β, pump intensity γ^2, and interaction length L determine the squeezing. Although L is spatially constrained by the strict momentum conservation requirements used to generate the conjugate field, the coupling β can be tuned by the probe power, 2-photon detuning, and atomic density. The dependence of the squeezing and probe transmission on these parameters is shown in figure 4.9. The probe transmission matches the linear dependence on probe input power that is expected with a linear optical gain interactions. However, the association between squeezing and probe gain starts breaking down with the detuning and cell temperature optimization in figure 4.9, where the peak probe transmission does not correspond to the peak squeezing. This discrepancy is present in other work, being attributed to unbalanced losses between the probe and conjugate and close probe proximity to atomic resonances compared to the pump [123, 124]. The form of the atomic coupling β is beyond the scope of our analysis, which has been explored more thoroughly as the source of this gain and squeezing inconsistency [125].

From figure 4.9, the optimal probe power is $P_{probe,in} = 55\ \mu$W, the two photon detuning around $\Delta_{2p} = 3035$ MHz, and cell temperature at $T_{cell} = 105°$C, all matching previous results using the same four-wave mixing process [107, 108]. Locking these parameters coarsely tunes the intensity correlations, but the alignment between the pump and probe fields can have a dramatic effect on the measured squeezing due to the strict phase mode matching conditions of the system. Therefore, it is important to carefully align and start the system using a rigorous and consistent approach to troubleshoot poor intensity correlations through the following process:

1. Warm up the squeezing cell to 105 °C. Without this the FWM gain will not be visible, even with proper alignment.

2. Sweep the probe laser frequency, revealing the FWM peak (figure 4.5).

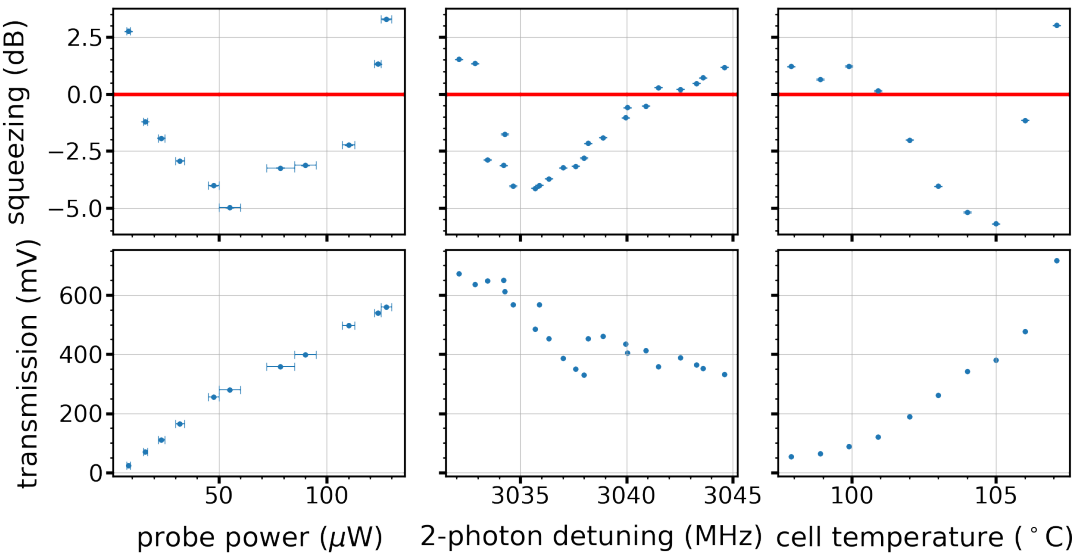


Figure 4.9: Dependence of squeezing on probe power ($P_{pump,in} = 340$ mW, $\Delta_{2p} = 3.0382$ GHz, $T_{cell} = 105$ °C), two-photon detuning ($P_{probe,in} = 55$ μW, $P_{pump,in} = 340$ mW, $T_{cell} = 105$ °C), and cell temperature ($P_{probe,in} = 55$ μW, $P_{pump,in} = 343$ mW, $\Delta_{2p} = 3.0357$ GHz). By optimizing these 3 parameters, we are optimizing the coupling ξ (equation 4.9 between atoms and incident optical fields). Probe power uncertainty is due to temperature- and polarization-induced fiber instabilities during data acquisition.

3. Tune the parked pump until the FWM gain peak is 1 GHz from the $F = 2 \rightarrow F' = 3$ hyperfine transition. Use the $F' = 2, 3$ hyperfine splitting of 361.6 MHz to calibrate to the frequency axis.

4. Park the probe laser at the FWM gain peak maximum.

5. Lock the 2 photon detuning to $\Delta_{2p} = 3035$ MHz using the phase lock, which is verified by monitoring the beat note shown in figure 4.6(b)

6. Set the probe power to $P_{probe,in} = 55$ μW and ensure pump power $P_{pump,in} \geq 350$ mW. At this point the conjugate field should be visible and, assuming proper alignment in the photodetector, noise cancellations should be seen (i.e. noise increases after blocking one of the probe or conjugate fields due to the lack of noise cancellation).

7. Sensitively tune the pump alignment mirrors until squeezing is captured.

Should the squeezing signal vanish, one only need check the previous steps to verify all other parameters are properly tuned. If working in the optimum parameter space, only then should the pump alignment be tuned to obtain the intensity squeezing, which has its own process required for *each* translation of the pump field:

1. Tune the alignment of the pump to minimize the noise and maximize the probe transmission to optimize the squeezing.

2. Verify probe and conjugate alignment into the photodetector, ensuring no clipping of either probe or conjugate fields are occurring. Move the probe and conjugate pickoff mirrors if needed.

3. Align the irises to the probe and conjugate maximum transmission to further filter out the pump field. Verify the lack of pump leakage into the photodetector by blocking the probe input, and gradually expanding the irises until just before the pump leakage starts contributing to the measured noise.

Due to momentum conservation, only the conjugate field position will be dependent on the pump alignment, requiring the most attention to downstream alignments to the photodetector. It is clearly evident how sensitive and involved the alignment process is to achieve quantum-enhanced noise suppression. However upon successful alignment, the differential intensity noise results in -4 – -4.4 dB relative to the classical shot noise limit, as demonstrated in figure 4.10

Similar experiments have been able to achieve -8 – -9 dB of squeezing [57] by carefully matching the spatial modes between the pump and probe lasers and minimizing the optical losses in either probe or conjugate output fields. Careful phase matching between pump and probe fields would greatly enhance the performance of the quantum-enhanced magnetometer to yield a -9 dB improvement (compared to shot noise) to magnetometer sensitivity.

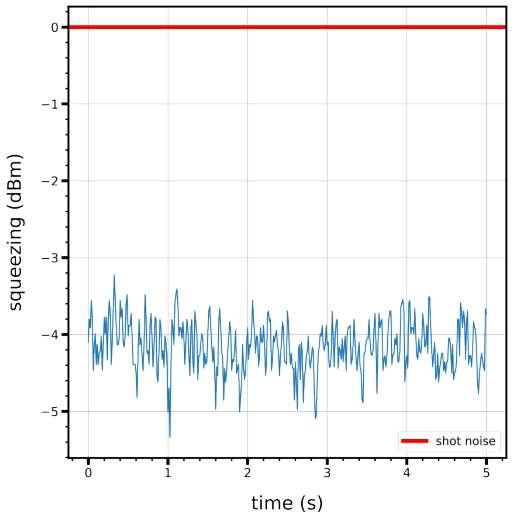


Figure 4.10: Demonstration of two-mode intensity squeezing from the FWM process at 300kHz frequency.

This quantum-enhanced noise suppression is demonstrated at the cost of working in a far-detuned frequency regime. However, the NMOR interaction is maximally coupled in the resonant case, corresponding to the dark state from equation 3.8, becoming much less sensitive in the far-detuned case. In the next chapter, we implement an approach to compromise between these two conflicting regimes, where we induce magnetic field sensitivity in the far-detuned optical fields. Combining these methods, we gain all the advantages of quantum noise suppression from FWM and sensitive magnetic field measurement from NMOR to eliminate the optical noise limit set by quantum uncertainty principles.

Chapter 5

Far-Detuned Quantum-Enhanced Magnetometry

FWM provides quantum-enhanced noise suppression using off-resonant optical fields to minimize optical losses induced by atomic absorption. However, operating an NMOR-based magnetometer in the off-resonant regime significantly reduces the magnetic field sensitivity due to the reduced atomic coupling with the far detuned fields. In this chapter, we develop a combined approach to maintain the noise suppression from FWM and induce magnetic sensitivity using nonlinear interaction within a separate rubidium vapor cell. The combined scheme makes it possible to detect magnetic fields not measurable with coherent or classical magnetometer schemes by addressing the photon shot noise that limits traditional NMOR-based magnetometers.

Recent research has explored the use of FWM to reduce optical noise in atomic magnetometers, where one of the primary challenges is using far-detuned fields from FWM within NMOR, which is most sensitive near atomic resonances [25, 126]. Groups have found ways around this through optical pumping processes in a gradiometer configuration [49] or *in-situ* within the FWM interaction region [50]. However, these two methods use complex and sensitive optical schemes, requiring additional dimensions or strict phase matching discussed in chapter 4. The work presented here achieves similar quantum-enhanced mag-

netometer performance without sensitive optical alignment in the aforementioned schemes.

Our approach involves reusing the pump field from FWM to access nonlinear susceptibilities for the NMOR interaction from chapter 3. The addition of this pump field in a simple counterpropagating alignment does not require sensitive phase matching or extra dimensions. The nonlinearity of the interaction enables NMOR in far-detuned regimes for probe and pump fields that are already used in FWM.

5.1 Enhancing Off-Resonant Magnetic Sensitivity

While the theory and mechanisms behind far-detuned magnetometry has been previously reported [127–129], here we summarize the the effect in a straightforward approach that permits the use of the intensity-squeezed light generated from FWM. In the traditional NMOR scheme shown in figure 5.1(a), the coherence depends on the detuning Δ_{probe}. In far-detuned regimes, the coupling between ground states m_F is weakened, resulting in the rapid falloff of magnetic sensitivity reliant on this ground state coupling and coherence.

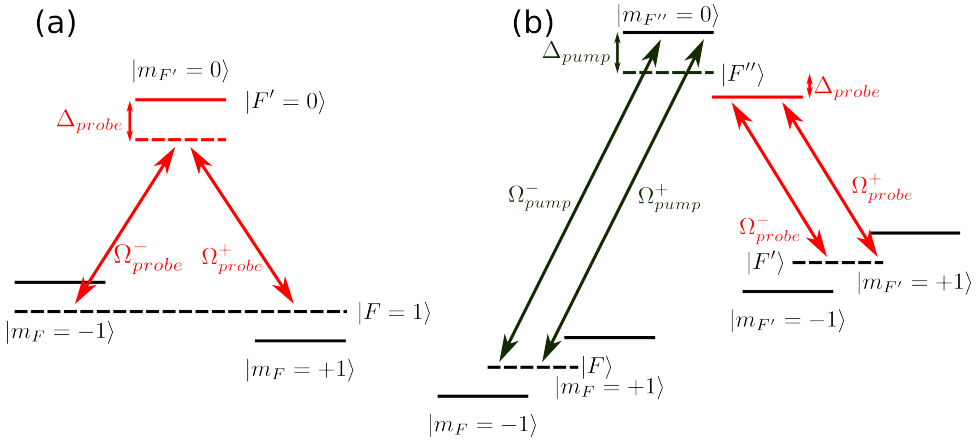


Figure 5.1: Comparison between (a) resonant NMOR and (b) far-detuned magnetometry. The addition of the pump field in the Λ system breaks the symmetry of the traditional Λ scheme by establishing an additional coherence.

If a pump field $\Omega^{\pm}_{pump}$ is included to interact with a common excited state $|F''\rangle$ as the traditional NMOR scheme in figure 5.1(b), an additional coherence path can occur between the two interactions to facilitate polarization rotation. This system exhibits state

population transfer from the pump Λ system into the probe Λ system in a far-detuned regime where $\Delta_{pump,probe} \geq 1$ GHz. The result of this effect is far-detuned magnetic sensitivity enabled by the presence of the pump field. Figure 5.2 demonstrates this effect due to a sinusoidal magnetic field for a $\Delta_{probe} \geq 1$ GHz red-detuned probe from the ^{87}Rb D_1 $F = 2 \rightarrow 1$ transition, and a resonant pump on the ^{87}Rb D_1 $F = 2 \rightarrow 2$ transition. While this frequency regime differs from the detunings used in FWM (as shown in figure 4.5), it is found that other frequency regimes still demonstrate this principle, such as the frequencies used in FWM.

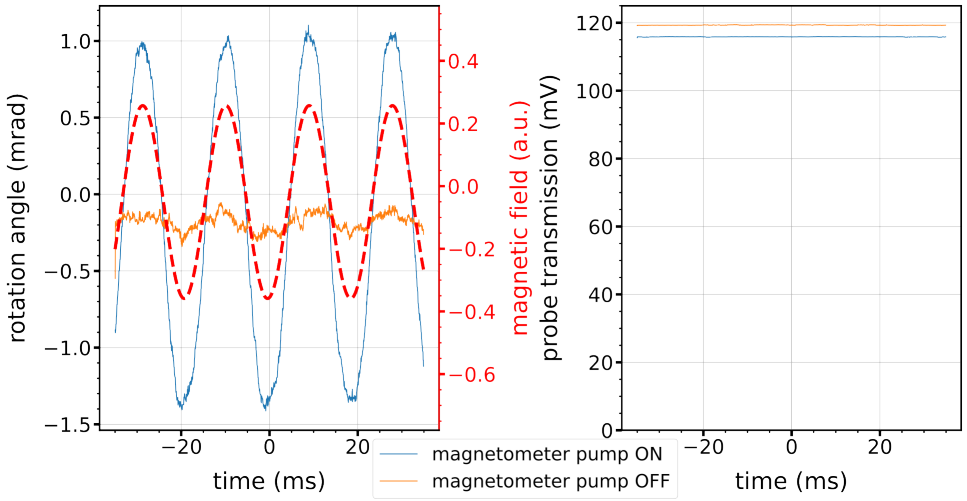


Figure 5.2: Left: Demonstration of far-detuned magnetometry driven by a sinusoidal magnetic field (dashed red) for $P_{pump} = 5$ mW, $P_{probe} = 150$ μW, $T_{cell} = 21$ °C (room temperature), $\Delta_{pump} = 0$ MHz and $\Delta_{probe} = -1816$ MHz from the ^{87}Rb D_1 $F = 2 \rightarrow F' = 2$ transition. The polarization angle only rotates in the presence of the pump field (blue), and in the absence of the pump (orange), the NMOR oscillations are significantly decrease due to the far detuning of the probe field. This differs from the frequency regime for the FWM, but the resulting far-detuned magnetometer principle is identical in either regime. Right: Probe transmission in the presence of the pump (blue) and absence of the pump (orange). The 3% increase in transmission indicates the lack of optical pumping or FWM processes.

While the term "pump" is used for the second field that induces magnetic sensitivity, it is not to be confused with a pump field used in optical pumping or electromagnetically-induced transparency. This process has negligible effect on the probe transmission, given that the probe transmission differed by less than 3% in the presence of the pump field shown in figure 5.2.

This effect has been studied as a way to improve magnetometer sensitivity [127–129] but here we optimize the magnetic sensitivity for far-detuned optical fields generated from the FWM process.

5.2 Squeezed Far-Detuned Magnetometry Characterization

To combine the two effects to demonstrate squeezed far-detuned magnetometry, we sequentially set up the squeezing and magnetometer setups as shown in figure 5.3. We send the probe field to the magnetometer, allowing the pump and probe to counterpropagate within the cell for magnetometer measurements, while the conjugate bypasses the cell to solely provide a reference for the optical noise suppression. The magnetometer cell is an isotopically pure ^{85}Rb cell of length $L = 1$" with antireflection coating to minimize optical losses in the probe field (at 795 nm). The cell is enclosed with a temperature-controlled and magnetic shielded enclosure identical to the FWM cell enclosure, but with the added capability of applying uniform magnetic fields using an internal solenoid coil, and a pair of gradient magnetic field coils to apply magnetic gradients perpendicular to the laser propagation direction.

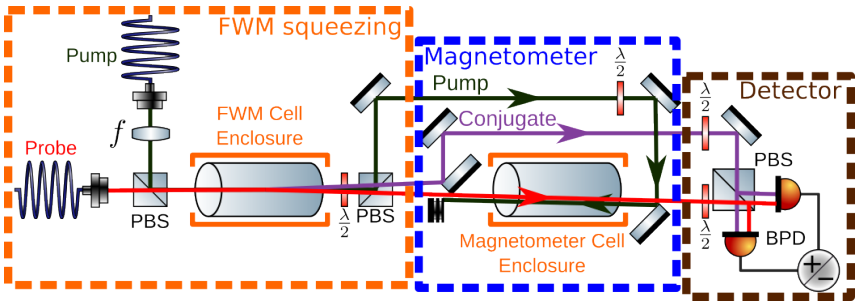


Figure 5.3: Combined experimental scheme for the squeezed light magnetometer. The FWM cell generates -4 – -4.4 dB of squeezing, which is sent to the magnetometer cell ($L = 1$") for magnetic field sensitivity characterization. The polarimeter detector is configured to measure NMOR using the quantum-enhanced noise suppression from FWM.

The magnetic field from the solenoid is calibrated to the voltage using previous measurements of atomic Zeeman shifts as a function of solenoid current [130]. The solenoid is

calibrated so that 10 mA solenoid current equates to 700 kHz of atomic Zeeman shift, and by using the hyperfine splitting within the ^{87}Rb transitions of 700 kHz per 1 G of magnetic field [72], then 10 mA of current equates to 1 G of magnetic field. The current through the solenoid (i.e. an inductor) is driven by a function generator to generate sinusoidal magnetic fields across the magnetometer cell, and the relation between the driving voltage and current in the coil is given by Ohm's law across the inductor and resistor that make up the magnetic field solenoid.

$$B_{solenoid} = \frac{1\text{ G}}{10\text{ mA}} \frac{V_{FG}}{\sqrt{(R_{FG} + R_{solenoid})^2 + (fL)^2}}\text{ mA}, \tag{5.1}$$

where $R_{FG} = 50\ \Omega$ is the function generator output resistance, $R_{solenoid} = 25.4\ \Omega$ is the solenoid resistance, $L = 9.24$ mH the measured solenoid inductance, and $f = 300$ kHz the linear driving frequency.

To detect NMOR in the probe laser, the pump field from the FWM process is reused in a counter-propagating configuration to generate the far-detuned magnetometry scheme in figure 5.1(b). In addition, this injection of probe and conjugate on opposing polarimeter input ports allows for gradiometric measurements of magnetic fields between the probe and conjugate regions.

5.2.1 Squeezed Magnetometer Optimizations

Our figure of merit to characterize far-detuned magnetometer performance is the signal-to-noise ratio (SNR). To measure SNR, we take two traces from the spectrum analyzer: One measuring the signal on the spectrum analyzer due to a 300kHz sinusoidal magnetic field, and another measuring the noise resulting whenever the oscillating magnetic field is turned off. The difference between the two yields the signal-to-noise *ratio* since the traces measured on the spectrum analyzer are in dBm. Measuring constant traces over the measurement time collects enough points to extract uncertainty statistics for each squeezing measurement.

The SNR of the magnetometer is optimized through the pump power, pump polarization (relative to the probe polarization), cell temperature, and probe/conjugate balancing angles into the detector. The pump power and polarization determine the efficiency of the population transfer from the pump interaction into the probe interaction in figure 5.1(b), while the cell temperature optimizes the atomic density for the NMOR response of the probe scheme in equation 3.12. Finally, the balancing angles into the polarimeter determine the ratio of NMOR signal to FWM noise suppression.

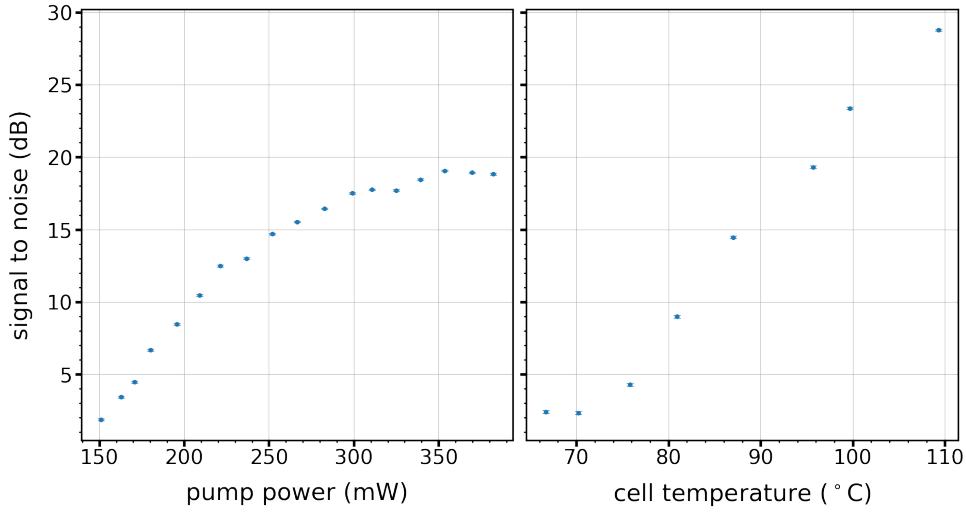


Figure 5.4: Optimizations to maximize the SNR of the magnetometer by varying pump power (left; $T_{cell} = 110$ °C, $P_{probe} = 500$ μW) and cell temperature (right; $P_{pump} = 380$ mW, $P_{probe} = 450$ μW). The SNR saturates around $P_{pump} = 350$ mW, while the temperature continues in a linear trend. To protect the Rb from reacting with the glass cell, only temperatures $T_{cell} \leq 110$ °C are used.

The optimizations for pump power and cell temperature are shown in figure 5.4. The pump power is limited by the 500 mW output of the amplifier, as well as the amount lost to the filtering PBS after the squeezing cell in figure 5.3, however, it is seen that the SNR saturates around the 350 mW pump power point. The cell temperature shows no maximum or saturation up to 110 °C, indicating that higher temperatures could further improve SNR. This, however, is limited by the temperature at which rubidium vapor reacts with the glass cell at around 120 °C, and is therefore not explored further.

The pump linear polarization optimization is the most enigmatic, revealing sharp fea-

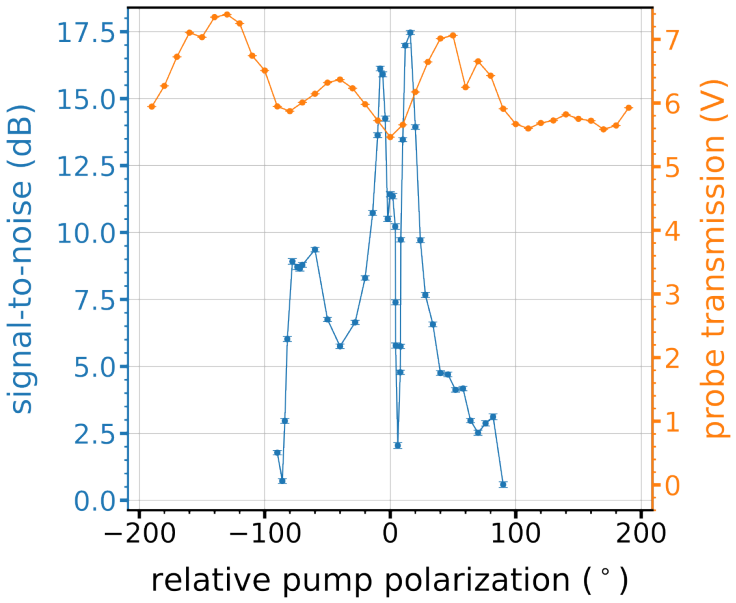


Figure 5.5: Dependence of SNR on pump polarization, showing a sharp response around 20° polarization angle relative to the probe polarization. (b) Probe transmission variance as a function of pump polarization, showing 14% fluctuation over the range of polarization angles. Pump polarization angles are physical polarization angles relative to the probe polarization.

tures in signal-to-noise displayed in figure 5.5(a) compared to the expected sinusoidal dependence [128]. The pump polarization is measured relative to the maximum transmission of the probe field through a polarizing beam splitter, where 0° indicates parallel pump and probe field polarizations. Figure 5.5(b) shows the probe transmission only varies within 10% through the rotation of the pump polarization angle, which is unlikely to cause a 15 dB boost to the SNR. Further studies should verify the source of this discrepancy, however, we show that a 15 dB improvement of SNR is possible with a pump polarization of ± 10° relative to the probe polarization.

The theoretical SNR of the system can be calculated by comparing the magnetic signal from NMOR and the intensity noise from FWM in the ratio [49]

$$SNR = \frac{\text{NMOR signal}}{\text{FWM noise}} = \frac{2g^2 \sin(2\theta_0)|\alpha|^2\theta_B}{(1+g^2-g^2\cos(4\theta_0))|\alpha|^2 + 2\sin^2(2\theta_0)g^2}, \tag{5.2}$$

for g the FWM gain, θ_0 the balancing angle, $|\alpha|^2$ the input probe intensity, and θ_B the

NMOR-induced polarization rotation angle.

The polarimeter system in figure 5.3 can be arranged to maximize noise suppression at $\theta_0 = 0$ or to maximize NMOR signal at $\theta_0 = \pi/4$.

To determine the best SNR in both probe and conjugate fields, we vary the polarimeter balancing angle by adjusting the probe and conjugate waveplates before the polarimeter PBS in figure 5.3. Figure 5.6 shows the resulting balancing angle dependence peaking near the angle of maximum noise suppression $\theta_0 \approx 0$. The SNR in equation 5.2 does not take into account optical losses or intermediate processes that can contribute to offsets in SNR peaks in figure 5.6. However, sharp SNR drops are present in both cases, showing a good qualitative agreement between the calculated and experimental traces.

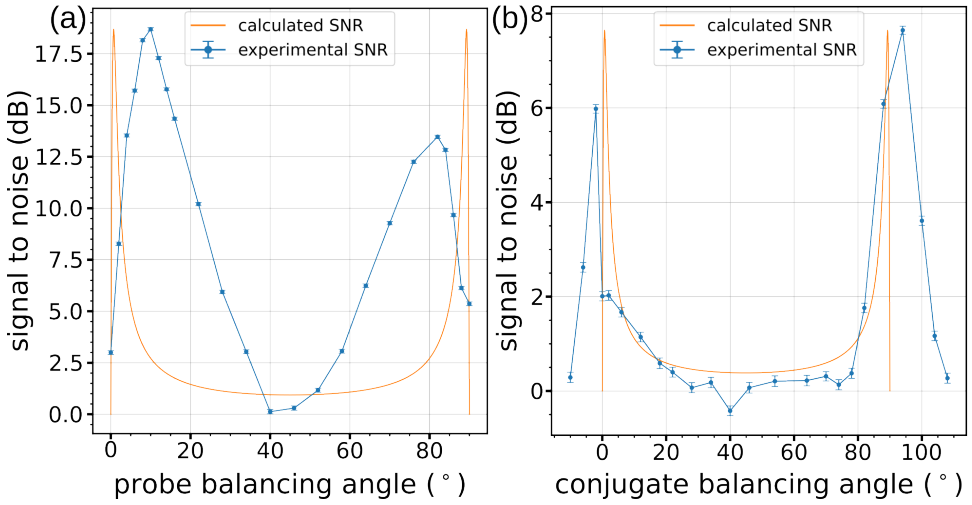


Figure 5.6: Experimental (blue) and calculated (orange) SNR dependence on (a) probe and (b) conjugate balancing angle, where 45° corresponds to the balanced polarimeter. The calculated traces are given by equation 5.2 and are plotted to show the functional trend of the balancing angle dependence.

Sending the intensity-correlated fields through the magnetometer setup will induce optical losses even with ideal optical materials and coatings. This can be remedied by compensating for the optical losses by reducing conjugate transmission through the use of a neutral density filters. Figure 5.7 shows optical loss compensation when the probe beam propagates through a VIS (350 - 700 nm) antireflection coated window. Placing a filter in

the conjugate field can then equalize the losses between the probe and conjugate, maintaining identical squeezing performance despite optical losses due to optics components or atomic interactions through the magnetometer system.

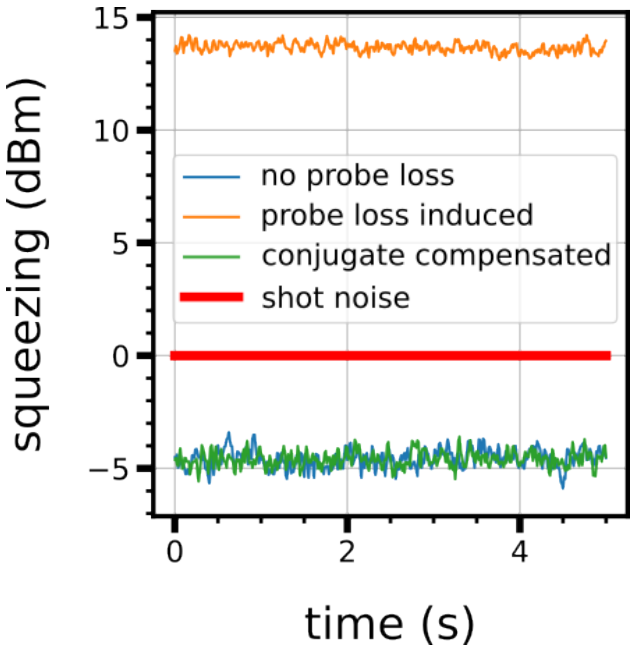


Figure 5.7: Demonstration of optical loss compensation on the squeezing when transmission loss is applied to the probe using a VIS antireflection coated window. Ideal squeezing performance is given in the absence of any optical losses (blue), but the squeezing degrades when loss is induced in the probe field (orange). By inducing equal amounts of loss in the conjugate channel (green), identical squeezing performance is recovered, resulting in the noises without probe loss (blue) and compensated conjugate (green) being equivalent.

5.3 Quantum-Enhanced Magnetometry

When each of the optimizations are used and optical losses in the probe path minimized, we measure a quantum-enhanced magnetometer signal in figure 5.8. Here we apply a sinusoidal 250 nT magnetic field at 300 kHz that is only visible in the presence of pump and conjugate fields.

This result shows that we can measure magnetic fields *not possible with classical detectors, including traditional NMOR*, as traditional optical magnetometers are limited by

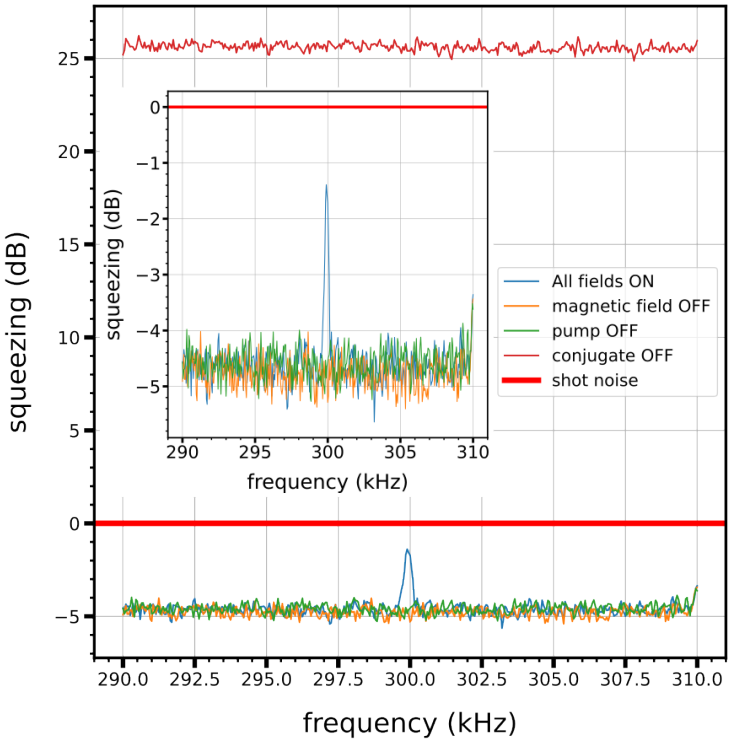


Figure 5.8: Quantum-enhanced magnetometer signal using the squeezed fields generated through FWM and inducing magnetic sensitivity using far-detuned magnetometry. The squeezed magnetometer signal (blue) lies below shot noise (thick red line), which vanishes in the absence of the pump field (green) and magnetic field (orange) within the magnetometer cell. Blocking the conjugate (thin red) removes the noise cancellation, and the magnetic field signal peak at 300 kHz vanishes due to the optical noise drowning out the magnetic field signal. Inset focuses on the range below shot noise for convenience.

optical shot noise. Without the pump field, the magnetically induced optical polarization rotation vanishes due to the far-detuning, while blocking the conjugate dramatically increases the noise by 20 dB, effectively drowning out the 250 nT signal. We note that 250 nT is chosen for this demonstration since the corresponding signal peak in figure 5.8 is 3 dB above the noise level, corresponding to the point where signal is equal to the noise. Realistically, the magnetometer will be limited by the noise floor, meaning the ultimate sensitivity would be 3 dB (or factor of 2) lower, resulting in a lower bound of 125 nT.

Although this initial demonstration pales in comparison to state of the art sub-pT NMOR magnetometers [131], we still demonstrate -4 – -4.7 dB performance improvement over shot-noise limited magnetometers. Accurate measure of the sensitivity improvement

entails comparing this quantum-enhanced magnetometer to the resonant single-Λ NMOR magnetometer.

This approach simplifies optical alignment by physically separating the squeezing and magnetic measurement processes, compared to previous work where both are done co-incidently [132]. Remote sensing applications may make use of this combined method, where squeezed light has successfully coupled into fibers [133]. This application enables remote magnetic field measurements in noisy environments, such as high-radiation nuclear accelerator beam lines.

To summarize, we have designed and built a scheme to reduce the optical noise of coherent fields used in atomic magnetometer setups, and by implementing a far-detuned optical scheme through inelastic wave-mixing, we can measure magnetic fields as far as 5 dB below the classical limit. The method is limited by how much squeezing is possible through the FWM process, which has been shown to exhibit down to -8 dB [57], if the optical losses are absolutely minimized.

5.4 Future Fundamental Research

With the demonstration of quantum-enhanced magnetometry there are ample opportunities to explore sensitivity using alternative configurations.

5.4.1 Quantum-Enhanced Magnetic Gradiometer

Forcing the conjugate field to bypass the magnetometer cell gives up potentially useful magnetic field information. By sending the conjugate through the magnetometer cell, duplicating and aligning the pump to the new conjugate field to induce magnetic sensitivity, and sending the conjugate to the opposite polarimeter input port as show in figure 5.9 yields a method to perform quantum-enhanced magnetic field gradiometry.

This reconfiguration is the most feasible with the current configuration of the setup, given that the current magnetometer cell enclosure has magnetic field gradient capabili-

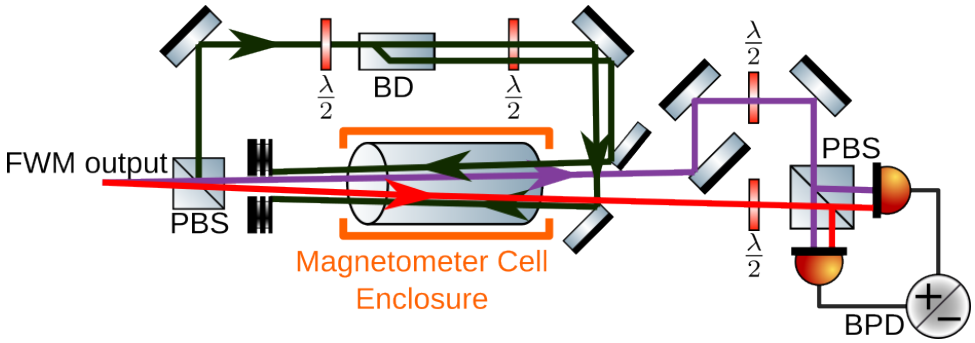


Figure 5.9: Experimental configuration using the conjugate to measure magnetic field gradients within the magnetometer cell. Inputting the conjugate in the opposite polarimeter input port allows differential measurement of the magnetic field between the probe and conjugate regions

ties. Pump power may be a limitation, since for optimal power for the single probe case is around 300 mW, requiring a 600 mW pump laser be split, which is not currently implemented in the setup. Regardless, the principle can be demonstrated as a test setup before migrating to the electron beam profiling experiment, which stands to greatly benefit from gradiometric measurements of particle beam magnetic field.

5.4.2 Quantum-Enhanced Magnetic Field Imaging & Vector Magnetometry

The reduction of optical noise using two-mode squeezed light generated through four-wave mixing can bring improvements to spatial characterization of magnetic fields. The original motivation to reduce optical noise in the electron beam profiling was due to the noise prevalent in the magnetic field images. However, implementation of the probe and conjugate fields for imaging is difficult due to the poor quantum-efficiency of cameras inducing optical losses between the lasers. Further, the formation of intensity-correlated photon pairs in the FWM process is spatially randomized, requiring some form of coincidence or correlation detection to map out and subtract the photon pairs within the laser cross section.

Additionally, recent advances in vector magnetometry make use of structured light using angularly-dependent polarizations created through a vortex waveplate [36]. Depending

on the resulting polarizations that are most and least prominent in a polarimeter image detector, the magnetic field direction can be determined using two parameters derived from the captured intensity profiles. As a similar case to magnetic field imaging, the reduction of optical noise through two-mode squeezed light can benefit the accuracy of magnetic field direction measurements, given that the measured signal is intensity dependent. Even more similar in this case, optical losses are present in the system, leading to degraded optical noise suppression.

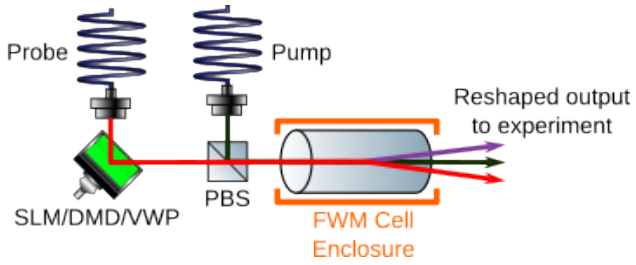


Figure 5.10: Potential experimental implementation to extract spatial information about magnetic field magnitude or direction using a spatial light modulator (SLM), digital micro-mirror device (DMD), or vortex waveplate (VWP).

However, others have shown that shaping the probe laser input to the FWM cell can also shape the output conjugate and, naturally, probe lasers identically [100]. Therefore, intensity masks or varying polarizations can be used in the probe input to reshape the probe output through the simple addition shown in figure 5.10. With the reshaped output, a single-pixel imaging setup [134] can be used to capture spatial gradients of magnetic field magnitude used in the electron beam magnetic field profiling. In principle, reduced optical noise would allow for more accurate magnetic field direction measurements, but in practice this remains quite challenging due to the specific hyperfine transition monitoring which may not work in the far-detuned regime that the quantum-enhanced magnetometer operates.

These approaches to extracting spatial magnetic field information are possible, and desirable in the case of measuring electron beam magnetic fields. With improved optical noise cancellation, smaller beam currents can be detected and profiled, allowing a broader

range of experimental charged particle beams to be used and diagnosed in experiments.

Chapter 6

Conclusion

In summary, thanks to the nonlinear interaction with atomic spins, the light polarization rotates in a dilute alkali-metal vapor in the presence of the magnetic field produced by a passing charged particle beam. Taking advantage of this effect, we demonstrated a non-invasive method for characterizing the position and total current of an electron beam that was obtained by mapping the nonlinear polarization rotation of a transverse probe laser crossing the e-beam. We experimentally evaluated the accuracy of the proposed technique to determine the total current and transverse position at 20 keV for e-beam currents between 30–110 μA, and discussed its current limitations. Since the e-beam is detected via its magnetic field, the scheme is insensitive to the beam energy [135] or charged particle type. A notable advantage of this measurement scheme is its immunity to the parasitic electric fields that inevitably accompany charged particle beams in the proximity of glass interfaces. Whereas such fields can substantially influence Rydberg atom electrometry measurements, the approach outlined in this dissertation remains insensitive to these electric fields, simplifying implementation in experimental environments. We expect that this technique can be applied to nuclear particle accelerators and refined to meet the precision required for experiments at the frontier of nuclear and high-energy physics research.

We also address the optical noise of the prototype electron beam detector using four-

wave mixing, a nonlinear effect from quantum optics, to reduce optical noise and detect magnetic fields down to -4.7 dB below traditional optical magnetometers. The far-detuned requirement for adequate four-wave mixing was preserved using another nonlinear process called inelastic wave-mixing, which allows magnetic sensitivity for a wider range of laser detunings and intensities. This elegant solution of reusing the four-wave mixing pump to induce magnetic sensitivity can be used remotely in a wide range of magnetic field detectors where strict alignments to preserve four-wave mixing are not always possible.

Looking ahead, the work discussed in this dissertation provides a solution to previously shot-noise limited magnetometers with the prospect of greatly enhancing magnetic gradiometer measurements. By accurately measuring magnetic field differences and working in a far-detuned regime, we relax the requirement for optimal isolation from environmental magnetic fields. This magnetic gradiometer configuration can be optimal for field work to measure magnetic field gradients only possible using quantum-enhanced field sensing.

This initial research paves the way for future fundamental and applied research to implement a quantum-enhanced tracker onto an accelerator beam line to non-invasively characterize charged particle beams, and assist in the impactful research on characterizing the fundamental constituents and interactions in physics.

Appendix A

Quantum Fundamentals

In the expression, $n_a = a^\dagger a$ is the photon number operator, made up of creation $a^\dagger$ and annihilation a operators which obey the commutation relation

$$\left[a, a^\dagger\right] = 1. \tag{A.1}$$

All expectation values will be evaluated using a coherent state input, defined as

$$|\alpha\rangle = e^{-\frac{|\alpha|^2}{2}} \sum_{n=0}^{\infty} \frac{\alpha^n}{\sqrt{n!}} |n\rangle, \tag{A.2}$$

where $|n\rangle$ are the number (or Fock) states. The creation and annihilation operators interact with the coherent state through:

$$a|\alpha\rangle = \alpha|\alpha\rangle \tag{A.3}$$

$$\langle\alpha|a^\dagger = \alpha^*\langle\alpha| \tag{A.4}$$

$$\tag{A.5}$$

We evaluate the photon number (or intensity) fluctuation through equation 4.16, where we ensure normal ordering (i.e. $a^\dagger a$ order of operators instead of the reverse order) through the commutation relation in equation A.1. The result, of which ends up reducing to

$$\langle n^2 \rangle = |\alpha|^4 + |\alpha|^2 \tag{A.6}$$

$$\langle n \rangle^2 = |\alpha|^4 \tag{A.7}$$

$$\langle (\Delta n)^2 \rangle = |\alpha|^2 = \langle n \rangle, \tag{A.8}$$

confirming the expectation that the photon number uncertainty should scale with the number of photons going into our detector.

Appendix B

Vacuum Procedures

This appendix highlights the procedures to use for various vacuum-related work. The STAIB electron gun manual details the processes for electron gun related work, but here we summarize the procedures for minimizing electron filament and alkali degradation in extenuating or common circumstances.

The procedures are structured like (and inspired by) aviation checklists, where each line is a step in the overall procedure. The left-hand side lists the object or parameter, while the right-hand side lists the action or value to set the parameter to.

As an example, the following entry

FILAMENT ..... 0.75 A SET

means to set the electron filament current to 0.75 A, while an entry reading

Pressure Reading ..... $\leq 10^{-3}$ Torr

means to ensure the pressure in the system is smaller than $\leq 10^{-3}$ Torr.

B.1 QET Valve Routines

B.1.1 Part Descriptions

Valves 2 and 3 in figure B.1 require manual rotation of the handles to open and shut. Clockwise rotation closes the valve, while counter-clockwise opens the valve. In general,

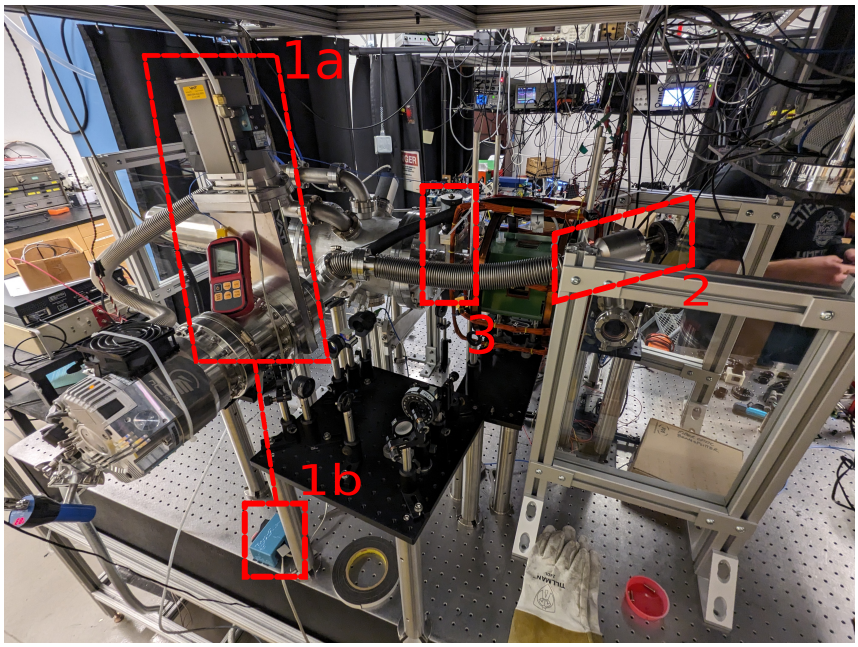


Figure B.1: 3 valves on the Faraday QET system. (1a) primary safety gate valve: dependent on lab power and the state of the control switch where the state of the valve is indicated through the white marker on the left side of the unit. (1b) control switch for the primary safety gate valve (annotated by (1a)): green opens the gate valve, red closes the valve. This switch will maintain the valve closed position until the green button is manually pushed. (2) gradual angle valve: an angle valve which slowly opens and closes by manually rotating the valve handle. (3) manual gate valve: valve similar in structure to the primary safety valve, but requires manual turning to open and close.

operate the angle valve (2) before the gate valve (3).

Valve 1 cuts the system off from the vacuum pumps, so it should remain open while pumping out.

B.1.2 Expected Power Outage Procedure

Perform the following actions as close to the outage as reasonably possible, to limit the amount of time air actively leaks into the system.

Valve 2 ..... **Fully closed**

Valve 3 ..... **Fully closed**

Valve 1 ..... **Open**

Following the power outage, perform the following actions as soon as reasonably possible.

Pressure Reading ..... $\leq 10^{-3}$ **Torr**

Valve 1 ..... **Open**

Valve 2 ..... **Gradually open, monitor system pressure remains** $\leq 10^{-3}$ **Torr**

Valve 3 ..... **Open**

Pressure Reading ..... ≈ 5 **nTorr once stabilised**

B.1.3 Unexpected Power Outage Procedure

Following the power outage, perform the following actions as soon as reasonably possible.

Pressure Reading ..... $\leq 10^{-3}$ **Torr**

Valve 1 ..... **Open**

Pressure Reading ..... ≈ 5 **nTorr once stabilised**

B.2 Minimizing Rb Oxidation When Opening Vacuum

Sometimes the areas between valves 2 and 3 in figure B.1 need to be exposed to atmosphere to fix or improve vacuum-related issues. However, exposing Rb to air will rapidly oxidize the alkali and degrade the cell optical quality. Therefore, to prevent interaction with the alkali, we constantly backflow the cell with an inert gas (such as nitrogen or argon) to prevent Rb oxidation and air from contaminating the vacuum. Once the chamber is filled with inert gas, the vacuum can be safely opened to perform work on the system. Once vacuum is sealed, the trapped inert gas should be pump out using the rough pump bypass in section 3.4.1 to protect the turbo pump. Once low vacuum is achieve, the turbo pump can be exposed to safely pump down the vacuum vessel.

Since the initial part of the process involves pressurizing the vessel to above 1 atm, extreme care needs to be taken when handling the part of the system under pressure. Never overpressure the vessel (roughly 2-3 atm), be cautious removing vacuum flanges under pressure, and protect the pumps from sudden spikes in high pressure.

Below lists the steps to perform vacuum work and minimize Rb degradation, following previous valve labelling and references.

B.2.1 Vacuum Work Gas Backflow Procedure

Valve 1 ..... **Fully closed**

Valve 2 ..... **Fully closed**

Valve 3 ..... **Fully closed**

Rb Cell Gas Inlet Valve ..... **Fully closed**

Inert Gas Bottle ..... **Open & Active (Gentle) Flow**

Inert Gas Bottle ..... **Connect to Rb Cell Gas Inlet Valve**

Inert Gas Bottle ..... **Pressure set to** ≥ 1 **atm**

Rb Cell Gas Inlet Valve ..... **Fully open**

Rb Cell ..... **Pressurized (read on Gas Bottle Valve)**

Vacuum System ..... **Perform maintenance**

Vacuum System ..... **Perform maintenance**

Vacuum System ..... **Sealed**

Rb Cell Gas Inlet Valve ..... **Fully closed**

Rough Pump Bypass Valve(s) ..... **Fully open**

System Pressure ..... $\sim$ **1 mTorr**

Valve 2 ..... ***Gradually*** **open until fully open**

Pressure Reading ..... $\leq 10^{-3}$ **Torr**

Valve 1 ..... **Open**

Pressure Reading ..... ≈ 5 **nTorr once stabilised**

B.3 Electron Gun Procedures

These procedures deal with turning the electron gun on to run the electron beam. Whenever the electron gun hasn't been used for longer than a week, or if the filament has been exposed to atmospheric pressure, the slow startup procedure in section B.3.2 should be followed. Otherwise, the fast startup procedure can be used from section B.3.3. Precise adherence to these procedures is not required, so long as any changes in electron filament current and energy are done gradually.

For the following processes, ION GAUGE 1 refers to the gauge monitoring the upstream chamber, while ION GAUGE 2 monitors the downstream chamber next to the Faraday cup.

B.3.1 Preliminary Checks

GATE VALVE 1 ..... OPEN
GATE VALVE 2 ..... OPEN
GATE VALVE 3 ..... OPEN
ION GAUGE 1 ..... ON
(OPTIONAL) ION GAUGE 2 ..... ON
PRESSURE ..... STABILIZED
ION GAUGE 1 ..... ≤ 5 μTorr
FARADAY CUP ..... CONNECTED
FARADAY MULTIMETER ..... ON & DC-I MODE
RADIATION SHIELDING ..... POSITIONED
GEIGER METER ..... ON

B.3.2 Slow Startup

MAIN POWER ..... ON

INTERLOCK ..... ON

BEAM BLANKING ..... OFF

CURRENT READING ..... I_F SET

FILAMENT ..... 0.25 A SET

STANDBY ..... 15 s

FILAMENT ..... 0.50 A SET

STANDBY ..... 15 s

FILAMENT ..... 0.75 A SET

STANDBY ..... 15 s

FILAMENT ..... 1.00 A SET

STANDBY ..... 15 s

ENERGY ..... 5.0 kV OVER 15 s

ARCING ..... STABILIZED

FILAMENT ..... 1.10 A OVER 30 s

ION GAUGE 1 ..... MONITOR

ENERGY ..... 10.0 kV OVER 30 s

FILAMENT ..... 1.20 A OVER 15 s

ION GAUGE 1 ..... MONITOR

EMISSION ..... $I_E \leq 1.0$ μA

ENERGY ..... 15.0 kV OVER 30 s

FILAMENT ..... 1.30 A OVER 15 s

ENERGY ..... 20.0 kV OVER 60 s

FILAMENT ..... 1.30 A OVER 15 s

FILAMENT ..... $\leq$ 1.80 A SET

BEAM BLANKING ..... FUNCTIONAL

DEFLECTION ..... X & Y SET

GRID ..... SET

FOCUS ..... SET

RADIATION RATES ..... CHECK

B.3.3 Fast startup

MAIN POWER ..... ON

INTERLOCK ..... ON

BEAM BLANKING ..... OFF

CURRENT READING ..... I_F SET

FILAMENT ..... 1.0 A OVER 30 s

FILAMENT ..... 1.3 A OVER 30 s

ENERGY ..... 20 kV OVER 120 s

BEAM BLANKING ..... FUNCTIONAL

DEFLECTION ..... X & Y SET

GRID ..... SET

FOCUS ..... SET

RADIATION RATES ..... CHECK

B.3.4 Standby (less than 1 hr)

FILAMENT ..... 1.20 A SET

B.3.5 Standby (less than 3 hr)

FILAMENT ..... 1.00 A SET

ENERGY ..... $\leq$ 10 kV SET

B.3.6 Shutdown

FILAMENT ..... 0.00 A SET

ENERGY ..... 0.0 kV SET

MAIN POWER ..... OFF

INTERLOCK ..... OFF

Appendix C

Squeezing Balanced Photo-Detector Schematic

This appendix discusses the design of the balanced photodetector (BPD) used to measure squeezing generated from four-wave mixing. Having a photodetector design capable of measuring individual probe and conjugate transmission in addition to the joint sum and differential transmission simultaneously acquires shot noise measured through the total probe transmission and differential noise to extract the quantum-enhanced noise suppression.

The BPD is a custom design that can be optimized for the desired detector frequency through a combination of filter and amplifier circuits using operational amplifiers. In our scheme, we tune the filters for uniform frequency response at 300 kHz where stable and optimal squeezing was measured in our experiment. To minimize losses induced by the photodetectors, we use high efficiency (QE $\sim$60%) and bandwidth ($f_c = 300$ MHz) Hamamatsu S3883 Si photodiodes (compared to the camera used in the NMOR experiment, with QE $\leq$ 20%). OP276 amplifiers are used for low noise, high bandwidth, and precision, supplied by $\pm$ 15 V for large output range used in the experiment.

Figures C.1 and C.2 show the schematics for the circuit and connectors. The first stage is a pair of standard photodetector amplifier circuits with outputs POS and NEG.

These two outputs are transferred to voltage followers to filter and amplify the individual channel transmission with identical gain of 2, each output POS_OUT and NEG_OUT measurable by BNC connector. The differential channel is a voltage subtracter, using POS and NEG (i.e. **not** the outputs of the voltage followers POS_OUT and NEG_OUT), whose outputs can be read out by BNC or SMA for spectrum analyzer readout. Finally, the sum of transmissions is a voltage adder, adding inputs POS_OUT and NEG_OUT to SUM_OUT read using a BNC cable. The corresponding gain of each circuit is annotated throughout figure C.1, where the adding and subtracting circuits have a gain of 1 and 2, respectively

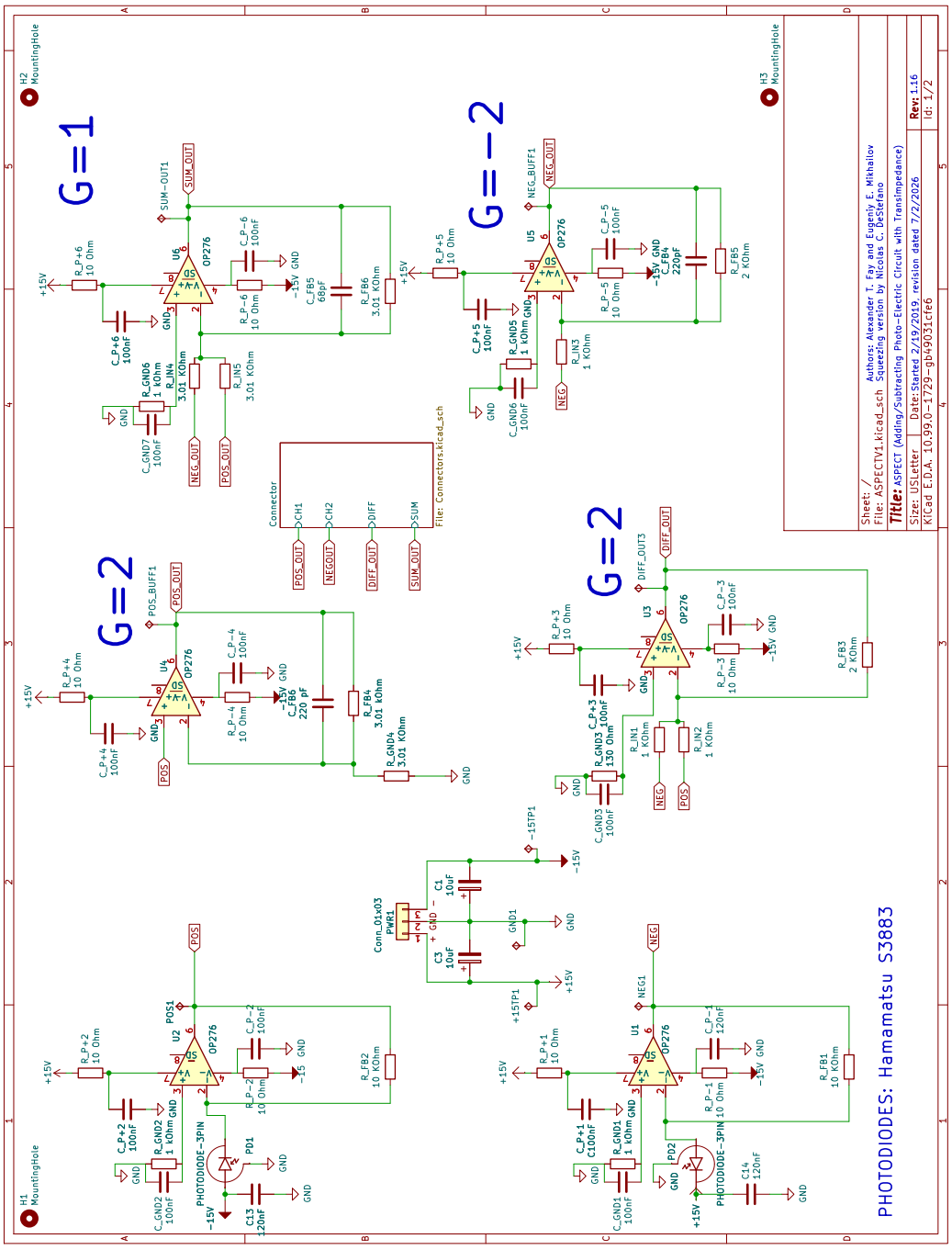


Figure C.1: Electronic schematic for the op-amp circuits and power supply.

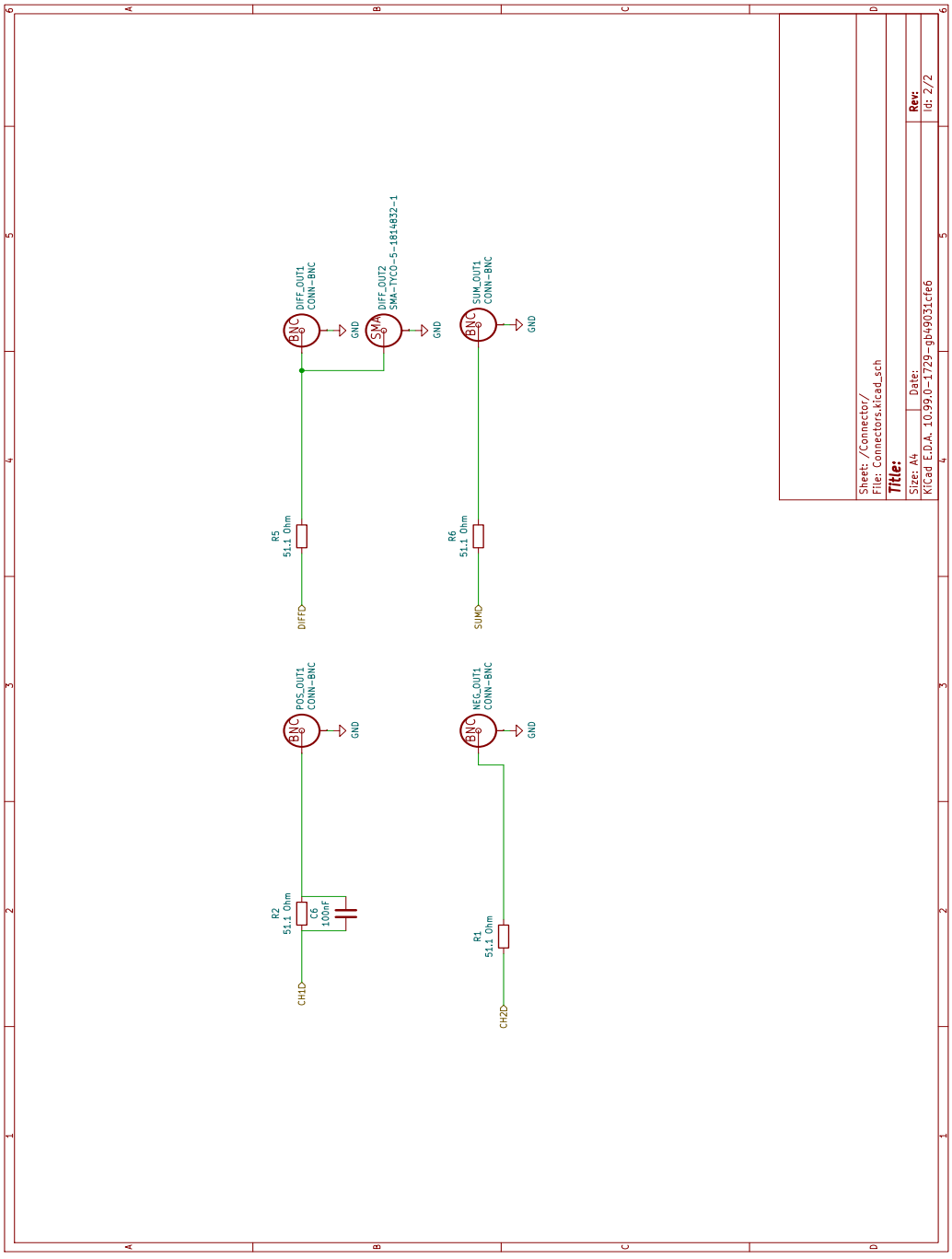


Figure C.2: Electronic schematic for the connectors for various outputs, POS_OUT (CH1), NEG_OUT (CH2), DIFF_OUT (DIFF), and SUM_OUT (SUM).

References

[1] C. Yan et al. Superharp: A Wire scanner with absolute position readout for beam energy measurement at CEBAF. *Nucl. Instrum. Meth. A*, 365:261–267, 1995.

[2] R. Bossart, J. Bosser, L. Burnod, E. d'Amico, G. Ferioli, J. Mann, F. Meot, and R. Coïsson. *Proton Beam Profile Monitor using Synchrotron Light*, pages 470–475. Birkhäuser Basel, Basel, 1980.

[3] S.T. Wang, D.L. Rubin, J. Conway, M. Palmer, D. Hartill, R. Campbell, and R. Holtzapple. Visible-light beam size monitors using synchrotron radiation at cesr. *Nuclear Instruments and Methods in Physics Research Section A: Accelerators, Spectrometers, Detectors and Associated Equipment*, 703:80–90, 2013.

[4] Wei Li, Jun Yan, Peifan Liu, and Ying K. Wu. Synchrotron radiation interferometry for beam size measurement at low current and in large dynamic range. *Phys. Rev. Accel. Beams*, 25:080702, Aug 2022.

[5] T. Hofmann, G.E. Boorman, A. Bosco, S.M. Gibson, and F. Roncarolo. A low-power laserwire profile monitor for h- beams: Design and experimental results. *Nuclear Instruments and Methods in Physics Research Section A: Accelerators, Spectrometers, Detectors and Associated Equipment*, 903:140–146, 2018.

[6] L. Corner, A. Aryshev, G.A. Blair, S.T. Boogert, P. Karataev, K. Kruchinin, L.J. Nevay, N. Terunuma, J. Urakawa, and R. Walczak. Laserwire: A high resolution non-invasive beam profiling diagnostic. *Nuclear Instruments and*

Methods in Physics Research Section A: Accelerators, Spectrometers, Detectors and Associated Equipment, 740:226–228, 2014. Proceedings of the first European Advanced Accelerator Concepts Workshop 2013.

[7] Remy Anne, Yvon Georget, Robert Hue, Christian Tribouillard, and Jean Luc Vignet. A noninterceptive heavy ion beam profile monitor based on residual gas ionization. *Nuclear Instruments and Methods in Physics Research Section A: Accelerators, Spectrometers, Detectors and Associated Equipment*, 329(1):21–28, 1993.

[8] Hampus Sandberg, William Bertsche, Dominique Bodart, Stephen Gibson, Steen Jensen, Swann Levasseur, Kenichirou Satou, Gerhard Schneider, James Storey, and Raymond Veness. Commissioning of timepix3 based beam gas ionisation profile monitors for the CERN proton synchrotron. *JACoW IBIC*, 2021:172–175, 2021.

[9] A. Variola, R. Jung, and G. Ferioli. Characterization of a nondestructive beam profile monitor using luminescent emission. *Phys. Rev. ST Accel. Beams*, 10:122801, Dec 2007.

[10] A. Salehilashkajani, H. D. Zhang, M. Ady, N. Chritin, P. Forck, J. Glutting, O. R. Jones, R. Kersevan, N. Kumar, T. Lefevre, T. Marriott-Dodington, S. Mazzoni, I. Papazoglou, A. Rossi, G. Schneider, O. Sedlacek, S. Udrea, R. Veness, and C. P. Welsch. A gas curtain beam profile monitor using beam induced fluorescence for high intensity charged particle beams. *Applied Physics Letters*, 120(17):174101, 2022.

[11] H. Maesaka, H. Ego, S. Inoue, S. Matsubara, T. Ohshima, T. Shintake, and Y. Otake. Sub-micron resolution rf cavity beam position monitor system at the sacla xfel facility. *Nuclear Instruments and Methods in Physics Research Section*

A: Accelerators, Spectrometers, Detectors and Associated Equipment, 696:66–74, 2012.

[12] K. B. Unser. The parametric current transformer, a beam current monitor developed for lep. *AIP Conference Proceedings*, 252(1):266–275, 04 1992.

[13] Lu Ma, Michael A. Viray, David A. Anderson, and Georg Raithel. Measurement of dc and ac electric fields inside an atomic vapor cell with wall-integrated electrodes. *Phys. Rev. Appl.*, 18:024001, Aug 2022.

[14] Sebastian Borówka, Uliana Pylypenko, Mateusz Mazelanik, and Michał Parniak. Sensitivity of a rydberg-atom receiver to frequency and amplitudemodulation of microwaves. *Appl. Opt.*, 61(29):8806–8812, Oct 2022.

[15] Wiktor Krokosz, Jan Nowosielski, Bartosz Kasza, Sebastian Borówka, Mateusz Mazelanik, Wojciech Wasilewski, and Michał Parniak. Electric-field metrology of a terahertz frequency comb using rydberg atoms. *Optica*, 12(11):1854–1864, Nov 2025.

[16] Rob Behary, Kevin Su, Nicolas DeStefano, Mykhailo Vorobiov, T. Averett, Alexandre Camsonne, Shukui Zhang, Charles T. Fancher, Neel Malvania, Eugeniy E. Mikhailov, Seth Aubin, and Irina Novikova. Electron beam characterization via quantum coherent electric field imaging. *Phys. Rev. Res.*, 7:L042042, Nov 2025.

[17] Mykhailo Vorobiov, Rob Behary, Will Torg, Nicolas DeStefano, Saskia Mordijck, Edward Thomas Jr., Saikat Chakraborty Thakur, Charles T. Fancher, Neel Malvania, Seth Aubin, Eugeniy E. Mikhailov, and Irina Novikova. Non-perturbative 2d spatial measurements of electric fields within a plasma sheath, 2025.

[18] Dmitry Budker and Derek F. Jackson Kimball, editors. *Optical Magnetometry*. Cambridge University Press, Cambridge, 5 2013.

[19] D. Budker, W. Gawlik, D. F. Kimball, S. M. Rochester, V. V. Yashchuk, and A. Weis. Resonant nonlinear magneto-optical effects in atoms. *Rev. Mod. Phys.*, 74:1153–1201, Nov 2002.

[20] Liam J Coy. *Assessing Quantum Magnetometry as an EmergingDetection Modality for Strategic Anti-Submarine Warfare*. PhD thesis, Massachusetts Institute of Technology, 2025.

[21] Y L Xu, Y J Zhou, K Ding, R Q Lv, M W Wu, and Z Wang. Unmanned unexploded ordnance detection system based on magnetic method. *Journal of Physics: Conference Series*, 2887(1):012021, nov 2024.

[22] Qiong Wang, Chen Zheng, Peili Wu, and Xiaoyu Wang. Geomagnetic/inertial navigation integrated matching navigation method. *Heliyon*, 8(11):e11249, 2022.

[23] Anthony P. Colombo, Tony R. Carter, Amir Borna, Yuan-Yu Jau, Cort N. Johnson, Amber L. Dagel, and Peter D. D. Schwindt. Four-channel optically pumped atomic magnetometer for magnetoencephalography. *Opt. Express*, 24(14):15403–15416, Jul 2016.

[24] Kasper Jensen, Mark Alexander Skarsfeldt, Hans Stærkind, Jens Arnbak, Mikhail V. Balabas, Søren-Peter Olesen, Bo Hjorth Bentzen, and Eugene S. Polzik. Magnetocardiography on an isolated animal heart with a room-temperature optically pumped magnetometer. *Scientific Reports*, 8(1):16218, Nov 2018.

[25] Irina B. Novikova. *Nonlinear magneto-optic effects in optically dense rubidium vapor*. PhD thesis, Texas A&M University, 2003. Copyright - Database copyright

ProQuest LLC; ProQuest does not claim copyright in the individual underlying works; Last updated - 2023-03-03.

[26] Dmitry Budker and Michael Romalis. Optical magnetometry. *Nature Physics*, 3(4):227–234, Apr 2007.

[27] Simon Michael Rochester. *Modeling nonlinear magneto-optical effects in atomic vapors*. University of California, Berkeley, 2010.

[28] M. Rosner, D. Beck, P. Fierlinger, H. Filter, C. Klau, F. Kuchler, P. Rössner, M. Sturm, D. Wurm, and Z. Sun. A highly drift-stable atomic magnetometer for fundamental physics experiments. *Applied Physics Letters*, 120(16):161102, 4 2022.

[29] V. G. Lucivero, W. Lee, N. Dural, and M. V. Romalis. Femtotesla direct magnetic gradiometer using a single multipass cell. *Physical Review Applied*, 15(1):014004, 1 2021.

[30] Eugeniy E. Mikhailov, I. Novikova, M. D. Havey, and F. A. Narducci. Magnetic field imaging with atomic rb vapor. *Opt. Lett.*, 34(22):3529–3531, Nov 2009.

[31] Chen Liu, Haifeng Dong, and Junjun Sang. Submillimeter-resolution magnetic field imaging with digital micromirror device and atomic vapor cell. *Applied Physics Letters*, 119(11):114002, 09 2021.

[32] Nicolas DeStefano, Saeed Pegahan, Aneesh Ramaswamy, Seth Aubin, T. Averett, Alexandre Camsonne, Svetlana Malinovskaya, Eugeniy E. Mikhailov, Gunn Park, Shukui Zhang, and Irina Novikova. Electron beam characterization via quantum coherent optical magnetometry. *Applied Physics Letters*, 125(26):264001, 12 2024.

[33] Orang Alem, Rahul Mhaskar, Ricardo Jiménez-Martínez, Dong Sheng, John LeBlanc, Lutz Trahms, Tilmann Sander, John Kitching, and Svenja Knappe. Magnetic field imaging with microfabricated optically-pumped magnetometers. *Opt. Express*, 25(7):7849–7858, Apr 2017.

[34] Hwang Lee, Michael Fleischhauer, and Marlan O. Scully. Sensitive detection of magnetic fields including their orientation with a magnetometer based on atomic phase coherence. *Phys. Rev. A*, 58:2587–2595, Sep 1998.

[35] Kevin Cox, Valery I. Yudin, Alexey V. Taichenachev, Irina Novikova, and Eugeniy E. Mikhailov. Measurements of the magnetic field vector using multiple electromagnetically induced transparency resonances in rb vapor. *Phys. Rev. A*, 83:015801, Jan 2011.

[36] Owen Rollins, Eugeniy E. Mikhailov, and Irina Novikova. Magnetic field direction detection using electromagnetically induced transparency with a vector vortex beam. *Opt. Lett.*, 51(4):961–964, Feb 2026.

[37] Mario Gonzalez Maldonado, Owen Rollins, Alex Toyryla, James A. McKelvy, Andrey Matsko, Isaac Fan, Yang Li, Ying-Ju Wang, John Kitching, Irina Novikova, and Eugeniy E. Mikhailov. Sensitivity of a vector atomic magnetometer based on electromagnetically induced transparency. *Opt. Express*, 32(14):25062–25073, Jul 2024.

[38] James McKelvy, Irina Novikova, Eugeniy E. Mikhailov, Mario Gonzalez, Isaac Fan, Yang Li, Ying-Ju Wang, John Kitching, and Andrey Matsko. Application of kernel principal component analysis for optical vector atomic magnetometry. *TechRxiv*, 2023(0519), 2023.

[39] Adam Wojciechowski, Eric Corsini, Jerzy Zachorowski, and Wojciech Gawlik. Nonlinear faraday rotation and detection of superposition states in cold atoms. *Phys. Rev. A*, 81:053420, May 2010.

[40] S Franke-Arnold, M Arndt, and A Zeilinger. Magneto-optical effects with cold lithium atoms. *Journal of Physics B: Atomic, Molecular and Optical Physics*, 34(12):2527, jun 2001.

[41] M. P. Ledbetter, I. M. Savukov, V. M. Acosta, D. Budker, and M. V. Romalis. Spin-exchange-relaxation-free magnetometry with cs vapor. *Phys. Rev. A*, 77:033408, Mar 2008.

[42] Igor Mykhaylovich Savukov, Grosz Asaf, Michael J. Haji-Sheikh, and Subhas C. Mukhopadhyay. *Spin Exchange Relaxation Free (SERF) Magnetometers*, pages 451–491. Springer International Publishing, Cham, 2017.

[43] Jundi Li, Wei Quan, Binquan Zhou, Zhuo Wang, Jixi Lu, Zhaohui Hu, Gang Liu, and Jiancheng Fang. Serf atomic magnetometer–recent advances and applications: A review. *IEEE Sensors Journal*, 18(20):8198–8207, 2018.

[44] S. J. Seltzer and M. V. Romalis. Unshielded three-axis vector operation of a spin-exchange-relaxation-free atomic magnetometer. *Applied Physics Letters*, 85(20):4804–4806, 11 2004.

[45] Jiahui Li and Irina Novikova. Improving sensitivity of an amplitude-modulated magneto-optical atomic magnetometer using squeezed light. *J. Opt. Soc. Am. B*, 39(11):2998–3003, Nov 2022.

[46] Eugeniy E. Mikhailov and Irina Novikova. Low-frequency vacuum squeezing via polarization self-rotation in rb vapor. *Opt. Lett.*, 33(11):1213–1215, Jun 2008.

[47] A. B. Matsko, I. Novikova, G. R. Welch, D. Budker, D. F. Kimball, and S. M. Rochester. Vacuum squeezing in atomic media via self-rotation. *Phys. Rev. A*, 66:043815, Oct 2002.

[48] Travis Horrom, Robinjeet Singh, Jonathan P. Dowling, and Eugeniy E. Mikhailov. Quantum-enhanced magnetometer with low-frequency squeezing. *Physical Review A - Atomic, Molecular, and Optical Physics*, 86(2):023803, 8 2012.

[49] Shuhe Wu, Guzhi Bao, Jinxian Guo, Jun Chen, Wei Du, Minwei Shi, Peiyu Yang, Liqing Chen, and Weiping Zhang. Quantum magnetic gradiometer with entangled twin light beams. *Science Advances*, 9(15):eadg1760, 2023.

[50] N. Otterstrom, R. C. Pooser, and B. J. Lawrie. Nonlinear optical magnetometry with accessible in situ optical squeezing. *Opt. Lett.*, 39(22):6533–6536, Nov 2014.

[51] M. Auzinsh, D. Budker, D. F. Kimball, S. M. Rochester, J. E. Stalnaker, A. O. Sushkov, and V. V. Yashchuk. Can a quantum nondemolition measurement improve the sensitivity of an atomic magnetometer? *Phys. Rev. Lett.*, 93:173002, Oct 2004.

[52] Anne Fabricant, Irina Novikova, and Georg Bison. How to build a magnetometer with thermal atomic vapor: a tutorial. *New Journal of Physics*, 25(2):025001, feb 2023.

[53] I. K. Kominis, T. W. Kornack, J. C. Allred, and M. V. Romalis. A subfemtotesla multichannel atomic magnetometer. *Nature*, 422(6932):596–599, Apr 2003.

[54] M. T. Turnbull, P. G. Petrov, C. S. Embrey, A. M. Marino, and V. Boyer. Role of the phase-matching condition in nondegenerate four-wave mixing in hot vapors for the generation of squeezed states of light. *Phys. Rev. A*, 88:033845, Sep 2013.

[55] Q. Glorieux, R. Dubessy, S. Guibal, L. Guidoni, J.-P. Likforman,

T. Coudreau, and E. Arimondo. Double-$Λ$ microscopic model for entangled light generation by four-wave mixing. *Phys. Rev. A*, 82:033819, Sep 2010.

[56] Quentin Glorieux, Luca Guidoni, Samuel Guibal, Jean-Pierre Likforman, and Thomas Coudreau. Strong quantum correlations in four wave mixing in 85Rb vapor. In *Quantum Optics*, Victor N. Zadkov and Thomas Durt, editors, volume 7727, page 772703. International Society for Optics and Photonics, SPIE, 2010.

[57] C. F. McCormick, V. Boyer, E. Arimondo, and P. D. Lett. Strong relative intensity squeezing by four-wave mixing in rubidium vapor. *Opt. Lett.*, 32(2):178–180, Jan 2007.

[58] Gisung Sim, Heewoo Kim, and Han Seb Moon. Intensity-difference squeezing from four-wave mixing in hot 85rb and 87rb atoms in single diode laser pumping system. *Scientific Reports*, 15(1):7727, Mar 2025.

[59] Daniel A. Steck. Rubidium 85 d line data. Technical report, Los Alamos National Laboratory, 2008.

[60] C. J. Foot. *Atomic physics*. Oxford master series in atomic, optical and laser physics. Oxford University Press, Oxford, 2023 - 2005.

[61] Marcis. Auzinsh, Dmitry. Budker, and Simon. Rochester. Optically polarized atoms : understanding light-atom interactions, 2010.

[62] Alan. Corney. *Atomic and laser spectroscopy*. Oxford science publications. Clarendon Press, Oxford ;, 1st paperback ed. edition, 1979 - 1977.

[63] Hans A. Bethe and Edwin E. Salpeter. *Quantum mechanics of one-and two-electron atoms*. Plenum Pub. Corp., New York, 1977.

[64] Daniel Manzano. A short introduction to the lindblad master equation. *AIP Advances*, 10(2):025106, 02 2020.

[65] W. Demtroder. *Laser spectroscopy*. Springer, Berlin, 4th ed. edition, 2008.

[66] Ran Finkelstein, Samir Bali, Ofer Firstenberg, and Irina Novikova. A practical guide to electromagnetically induced transparency in atomic vapor. *New Journal of Physics*, 2023.

[67] E. Figueroa, F. Vewinger, J. Appel, and A. I. Lvovsky. Decoherence of electromagnetically induced transparency in atomic vapor. *Opt. Lett.*, 31(17):2625–2627, Sep 2006.

[68] P. R. Berman. Optical faraday rotation. *American Journal of Physics*, 78(3):270–276, 03 2010.

[69] David Vojna, Ondřej Slezák, Antonio Lucianetti, and Tomáš Mocek. Verdet constant of magneto-active materials developed for high-power faraday devices. *Applied Sciences*, 9(15), 2019.

[70] d. budker, w. gawlik, d. f. kimball, s. m. rochester, v. v. yashchuk, and a. weis. resonant nonlinear magneto-optical effects in atoms. *Rev. Mod. Phys.*, 74:1153, 2002.

[71] A. B. Matsko, I. Novikova, M. S. Zubairy, and G. R. Welch. Nonlinear magneto-optical rotation of elliptically polarized light. *Phys. Rev. A*, 67:043805, Apr 2003.

[72] Daniel A. Steck. Rubidium 87 d line data. Technical report, Los Alamos National Laboratory, 2001.

[73] S. E. Harris. Electromagnetically induced transparency. *Physics Today*, 50(7):36, 1997.

[74] Michael Fleischhauer, Atac Imamoglu, and Jonathan P. Marangos. Electromagnetically induced transparency: Optics in coherent media. *Rev. Mod. Phys.*, 77:633–673, Jul 2005.

[75] M. V. Balabas, T. Karaulanov, M. P. Ledbetter, and D. Budker. Polarized alkali-metal vapor with minute-long transverse spin-relaxation time. *Phys. Rev. Lett.*, 105:070801, Aug 2010.

[76] L.S. Grattan and B. T. Meggitt. Optical fiber sensor technology : Applications and systems, 1999.

[77] Ayahiko Ichimiya and Philip I. Cohen. *Reflection high-energy electron diffraction.* Cambridge University Press, Cambridge, U.K. ;, 2004.

[78] L.-M. Peng, S. L. Dudarev, and M. J. Whelan. *High energy electron diffraction and microscopy.* Monographs on the physics and chemistry of materials ; 61. Oxford University Press, Oxford ;, 2004.

[79] G.-C. Wang and T.-M. Lu. Strain measurement of ultrathin epitaxial films using electron diffraction techniques. *Journal of Applied Physics*, 125(8):082401, 12 2018.

[80] Rob Behary, Kevin Su, Nicolas DeStefano, Jennifer Tsai, Todd Averett, Alexandre Camsonne, Shukui Zhang, Charles T. Fancher, Neel Malvania, Seth Aubin, Eugeniy E. Mikhailov, and Irina Novikova. Electron beam profiling via rydberg electromagnetically induced transparency in rubidium vapor with crossed laser beams, 2026.

[81] J. Allison, K. Amako, J. Apostolakis, et al. Geant4 developments and applications. *IEEE Transactions on Nuclear Science*, 53(1):270–278, 2006.

[82] J. Allison, K. Amako, J. Apostolakis, et al. Recent developments in geant4. *Nuclear Instruments and Methods in Physics Research Section A: Accelerators, Spectrometers, Detectors and Associated Equipment*, 835:186–225, 2016.

[83] S. Agostinelli, J. Allison, K. Amako, et al. Geant4—a simulation toolkit. *Nuclear Instruments and Methods in Physics Research Section A: Accelerators, Spectrometers, Detectors and Associated Equipment*, 506(3):250–303, 2003.

[84] A. L. Frank, E. T. Arakawa, and R. D. Birkhoff. Optical emission from irradiated foils. ii. *Phys. Rev.*, 126:1947–1952, Jun 1962.

[85] B. Bolzon, A. Aryshev, T. Aumeyr, S. Boogert, P. Karataev, K. O. Kruchinin, T. Lefevre, S. Mazzoni, L. Nevay, M. Shevelev, N. Terunuma, J. Urakawa, and C. P. Welsch. Very high resolution optical transition radiation imaging system: Comparison between simulation and experiment. *Phys. Rev. ST Accel. Beams*, 18:082803, Aug 2015.

[86] M. Castellano and V. A. Verzilov. Spatial resolution in optical transition radiation beam diagnostics. *Phys. Rev. ST Accel. Beams*, 1:062801, Oct 1998.

[87] Antoine Weis, Georg Bison, and Zoran D. Grujić. Magnetic resonance based atomic magnetometers. In *High Sensitivity Magnetometers. Smart Sensors, Measurement and Instrumentation*, A. Grosz, M. Haji-Sheikh, and S. Mukhopadhyay, editors, volume 19, pages 361–424. Springer, Cham, 2017.

[88] Kai Mei C. Fu, Geoffrey Z. Iwata, Arne Wickenbrock, and Dmitry Budker. Sensitive magnetometry in challenging environments. *AVS Quantum Science*, 2(4):044702, 12 2020.

[89] P. Grangier, R. E. Slusher, B. Yurke, and A. LaPorta. Squeezed-light–enhanced polarization interferometer. *prl*, 59:2153–2156, Nov 1987.

[90] P. M. Anisimov, R. A. Akhmedzhanov, I. V. Zelensky, and E. A. Kuznetsova. Influence of transverse magnetic fields and depletion of working levels on the nonlinear resonance faraday effect. *Journal of Experimental and Theoretical Physics*, 97(5):868–874, Nov 2003.

[91] K. F. Reim, P. Michelberger, K. C. Lee, J. Nunn, N. K. Langford, and I. A. Walmsley. Single-photon-level quantum memory at room temperature. *Phys. Rev. Lett.*, 107:053603, Jul 2011.

[92] J. Shapiro and S. Wagner. Phase and amplitude uncertainties in heterodyne detection. *IEEE journal of quantum electronics*, 20(7):803–813, 1984.

[93] B. J. Lawrie, P. D. Lett, A. M. Marino, and R. C. Pooser. Quantum sensing with squeezed light. *ACS Photonics*, 6(6):1307–1318, 2019.

[94] Paul-Antoine Moreau, Ermes Toninelli, Thomas Gregory, and Miles J. Padgett. Imaging with quantum states of light. *Nature Reviews.Physics*, 1(6):367–380, 06 2019. Copyright - Copyright Nature Publishing Group Jun 2019; Last updated - 2025-07-02.

[95] Chuan Xu, Lidan Zhang, Songtao Huang, Taxue Ma, Fang Liu, Hidehiro Yonezawa, Yong Zhang, and Min Xiao. Sensing and tracking enhanced by quantum squeezing. *Photon. Res.*, 7(6):A14–A26, Jun 2019.

[96] Yun-Yi Pai, Claire E. Marvinney, Chengyun Hua, Raphael C. Pooser, and Benjamin J. Lawrie. Magneto-optical sensing beyond the shot noise limit. *Advanced Quantum Technologies*, 5(1):2100107, 2022.

[97] K. Goda, O. Miyakawa, E. E. Mikhailov, S. Saraf, R. Adhikari, K. McKenzie, R. Ward, S. Vass, A. J. Weinstein, and N. Mavalvala. A quantum-enhanced prototype gravitational-wave detector. *Nature Physics*, 4(6):472–476, Jun 2008.

[98] J. Abadie, others, and The LIGO Scientific Collaboration. A gravitational wave observatory operating beyond the quantum shot-noise limit. *Nature Physics*, 7(12):962–965, Dec 2011.

[99] Hugo Defienne, Warwick P. Bowen, Maria Chekhova, Gabriela B. Lemos, Dan Oron, Sven Ramelow, Nicolas Treps, and Daniele Faccio. Advances in quantum imaging. *Nature Photonics*, 18(10):1024–1036, 10 2024.

[100] Vincent Boyer, Alberto M. Marino, Raphael C. Pooser, and Paul D. Lett. Entangled images from four-wave mixing. *Science*, 321(5888):544–547, 2008.

[101] Danilo Zia, Nazanin Dehghan, Alessio D'Errico, Fabio Sciarrino, and Ebrahim Karimi. Interferometric imaging of amplitude and phase of spatial biphoton states. *Nature Photonics*, 17(11):1009–1016, Nov 2023.

[102] Dongyu Liu, Mingsheng Tian, Shuheng Liu, Xiaolong Dong, Jiajie Guo, Qiongyi He, Haitan Xu, and Zheng Li. Ghost imaging with non-gaussian quantum light. *Phys. Rev. Appl.*, 16:064037, Dec 2021.

[103] Savannah L. Cuozzo, Pratik J. Barge, Nikunjkumar Prajapati, Narayan Bhusal, Hwang Lee, Lior Cohen, Irina Novikova, and Eugeniy E. Mikhailov. Low-light shadow imaging using quadrature-noise detection with a camera. *Advanced Quantum Technologies*, 5(7):2100147, 2022.

[104] Savannah L. Cuozzo, Pratik J. Barge, Nikunjkumar Prajapati, Narayan Bhusal, Hwang Lee, Lior Cohen, Irina Novikova, and Eugeniy E. Mikhailov. Low-light shadow imaging using quadrature-noise detection with a camera. *Advanced Quantum Technologies*, 5(7):2100147, 2022.

[105] Charris Gabaldon, Pratik Barge, Savannah L. Cuozzo, Irina Novikova, Hwang Lee, Lior Cohen, and Eugeniy E. Mikhailov. Quantum fluctuations spatial mode profiler. *AVS Quantum Science*, 5(2):025005, 06 2023.

[106] Martijn Jasperse. *Relative intensity squeezing by four-wave mixing in rubidium*. PhD thesis, University of Melbourne, School of Physics, 2010.

[107] Ziqi Niu. *Development of Quantum Information and Sensing Tools Based on Four-Wave Mixing in Hot Rubidium Vapor*. PhD thesis, College of William & Mary, 2025. Copyright - Database copyright ProQuest LLC; ProQuest does not claim copyright in the individual underlying works; Last updated - 2025-07-02.

[108] Nikunjkumar Prajapati. *Development of Quantum Information Tools Based on Multi-Photon Raman Processes in Rb Vapor*. PhD thesis, College of William & Mary, 2020. Copyright - Database copyright ProQuest LLC; ProQuest does not claim copyright in the individual underlying works; Last updated - 2025-07-02.

[109] Quentin Glorieux, Luca Guidoni, Samuel Guibal, Jean-Pierre Likforman, and Thomas Coudreau. Quantum correlations by four-wave mixing in an atomic vapor in a nonamplifying regime: Quantum beam splitter for photons. *Phys. Rev. A*, 84:053826, Nov 2011.

[110] C. F. McCormick, A. M. Marino, V. Boyer, and P. D. Lett. Strong low-frequency quantum correlations from a four-wave-mixing amplifier. *Phys. Rev. A*, 78:043816, Oct 2008.

[111] Jaeuk Baek, Sanghyun Park, Min-Hwan Lee, Heung-Ryoul Noh, and Geol Moon. Polarization-selective four-wave mixing in a degenerate multi-level system. *Scientific Reports*, 14(1):5705, Mar 2024.

[112] Ziqi Niu, Jianming Wen, Chuanwei Zhang, Shengwang Du, and Irina Novikova. Bi-chromatic intensity squeezing using four-wave mixing in 85rb vapor. *Optica Quantum*, 3(1):72–77, Feb 2025.

[113] L.-M. Duan, M. D. Lukin, J. I. Cirac, and P. Zoller. Long-distance quantum communication with atomic ensembles and linear optics. *Nature*, 414(6862):413–418, Nov 2001.

[114] L J Wang, C K Hong, and S R Friberg. Generation of correlated photons via four-wave mixing in optical fibres. *Journal of Optics B: Quantum and Semiclassical Optics*, 3(5):346, oct 2001.

[115] Nikunjkumar Prajapati, Ziqi Niu, and Irina Novikova. Quantum-enhanced

two-photon spectroscopy using two-mode squeezed light. *Opt. Lett.*, 46(8):1800–1803, Apr 2021.

[116] Zhenquan Yang, Prasoon Saurabh, Frank Schlawin, Shaul Mukamel, and Konstantin E. Dorfman. Multidimensional four-wave-mixing spectroscopy with squeezed light. *Applied Physics Letters*, 116(24):244001, 06 2020.

[117] Noah Schlossberger, Nikunjkumar Prajapati, Samuel Berweger, Andrew P. Rotunno, Alexandra Artusio-Glimpse, Matthew T. Simons, Abrar A. Sheikh, Eric B. Norrgard, Stephen P. Eckel, and Christopher L. Holloway. Rydberg states of alkali atoms in atomic vapour as si-traceable field probes and communications receivers. *Nature Reviews.Physics*, 6(10):606–620, 10 2024. Copyright - Copyright Nature Publishing Group Oct 2024; Last updated - 2025-07-02.

[118] Sebastian Borówka, Uliana Pylypenko, Mateusz Mazelanik, and Michał Parniak. Continuous wideband microwave-to-optical converter based on room-temperature rydberg atoms. *Nature Photonics*, 18(1):32–38, Jan 2024.

[119] K F Hulme. Nonlinear optical crystals and their applications. *Reports on Progress in Physics*, 36(5):497, may 1973.

[120] S. E. Harris and R. B. Miles. Proposed third-harmonic generation in phase-matched metal vapors. *Applied Physics Letters*, 19(10):385–387, 11 1971.

[121] Marlan O. Scully and M. Suhail Zubairy. *Quantum optics*, chapter 16.4 Four-wave mixing. Cambridge University Press, Cambridge ;, 1997.

[122] M. Jasperse, L. D. Turner, and R. E. Scholten. Relative intensity squeezing by four-wave mixing with loss: an analytic model and experimental diagnostic. *Opt. Express*, 19(4):3765–3774, Feb 2011.

[123] Leiming Cao, Jinjian Du, Jingliang Feng, Zhongzhong Qin, Alberto M. Marino, Mikhail I. Kolobov, and Jietai Jing. Experimental observation of quantum correlations in four-wave mixing with a conical pump. *Opt. Lett.*, 42(7):1201–1204, Apr 2017.

[124] R. C. Pooser, A. M. Marino, V. Boyer, K. M. Jones, and P. D. Lett. Quantum correlated light beams from non-degenerate four-wave mixing in an atomic vapor: the d1 and d2 lines of 85rb and 87rb. *Opt. Express*, 17(19):16722–16730, Sep 2009.

[125] Matthew Turnbull. *Multi-spatial-mode quadrature squeezing from four-wave mixing in a hot atomic vapour*. PhD thesis, University of Birmingham, 2014.

[126] D. Budker, D. F. Kimball, S. M. Rochester, V. V. Yashchuk, and M. Zolotorev. Sensitive magnetometry based on nonlinear magneto-optical rotation. *Physical Review A - Atomic, Molecular, and Optical Physics*, 62(4):7, 9 2000.

[127] Feng Zhou, Chengjie J. Zhu, Edward W. Hagley, and Lu Deng. Symmetry-breaking inelastic wave-mixing atomic magnetometry. *Science Advances*, 3(12):e1700422, 2017.

[128] Bei Liu, Jin Peng, Hai-Ning Wang, Chang-Feng Fang, Jun-Lei Wang, Xian Zhao, and Lu Deng. Dual-beam room-temperature atomic magnetometer with high sensitivity and large dynamic range. *Applied Physics Express*, 16(1):012008, jan 2023.

[129] L. Deng. Theory of colliding-probe atomic magnetometry: breaking the symmetry-enforced magneto-optical rotation blockade. *Opt. Express*, 30(24):44218–44228, Nov 2022.

[130] Ravn Jenkins. Measuring magnetic field gradients using electromagnetically induced transparency in rb vapor, 2019-05-01.

[131] Vito Giovanni Lucivero, Pawel Anielski, Wojciech Gawlik, and Morgan W. Mitchell. Shot-noise-limited magnetometer with sub-picotesla sensitivity at room temperature. *Review of Scientific Instruments*, 85(11):113108, 11 2014.

[132] N. Otterstrom, R. C. Pooser, and B. J. Lawrie. Nonlinear optical magnetometry with accessible in situ optical squeezing. *Opt. Lett.*, 39(22):6533–6536, Nov 2014.

[133] Priya Drashni, Hari P. Lamsal, Belle A. White, Noah A. Crum, George Siopsis, and Tian Li. High-flux sub-poissonian twin-beam generation from warm atomic vapor, 2026.

[134] Graham M. Gibson, Steven D. Johnson, and Miles J. Padgett. Single-pixel imaging 12 years on: a review. *Opt. Express*, 28(19):28190–28208, Sep 2020.

[135] Aneesh Ramaswamy, Svetlana A. Malinovskaya, Ünlü, Hilmi, and Norman J. M. Horing. *Control with EIT: High Energy Charged Particle Detection*, pages 363–392. Springer International Publishing, Cham, 2022.

ProQuest Number: 32740347

INFORMATION TO ALL USERS
The quality and completeness of this reproduction is dependent on the quality
and completeness of the copy made available to ProQuest.



Distributed by
ProQuest LLC a part of Clarivate (2026).
Copyright of the Dissertation is held by the Author unless otherwise noted.

This work is protected against unauthorized copying under Title 17,
United States Code and other applicable copyright laws.

This work may be used in accordance with the terms of the Creative Commons license
or other rights statement, as indicated in the copyright statement or in the metadata
associated with this work. Unless otherwise specified in the copyright statement
or the metadata, all rights are reserved by the copyright holder.

ProQuest LLC
789 East Eisenhower Parkway
Ann Arbor, MI 48108 USA